Modelling Turbulent Premixed CH_4/H_2/air Flames with Effects of Stretch, Heat Loss and Non-unity Lewis Number for Flame Stabilization and Dynamics

Halit Kutkan

Modelling Turbulent Premixed $CH_4/H_2/Air$ Flames

With Effects Of Stretch, Heat Loss And Non-unity

Lewis Number For Flame Stabilization And Dynamics

BY

Halit Kutkan

Dissertation discussed in partial fulfillment of

the requirements for the Degree of

DOCTOR OF PHILOSOPHY

Civil, Chemical and Environmental Engineering

curriculum in Fluid Dynamics and Environmental Engineering,

Department of Civil, Chemical and Environmental Engineering, University of Genoa, Italy

December, 2022

Advisors:
Dr. Giovanni Campa - Ansaldo Energia S.p.A.
Prof. Alessandro Bottaro - Università degli Studi di Genova

External Reviewers:
Prof. Wolfgang Polifke - Technische Universität München
Assoc. Prof. Antonio Andreini - Università degli Studi di Firenze

Examination Committee:
Prof. Carlo Camporeale - Politecnico di Torino
Prof. Marco Colombini - Università degli Studi di Genova
Assoc. Prof. Davide Laera - Politecnico di Bari
Prof. Marco Mancini - Politecnico di Milano

Ph.D. program in Civil, Chemical and Environmental Engineering
Curriculum in Fluid Dynamics and Environmental Engineering
Cycle 35th

Acknowledgements

ABSTRACT

This research study investigates the effects of hydrogen enrichment on bluff-body stabilized turbulent premixed methane flames in the lean combustion regime. To this end, a premixed combustion modelling closure is proposed for RANS (Reynolds Averaged Navier-Stokes), SAS (Scale Adaptive Simulation) and LES (Large Eddy Simulation) simulations of atmospheric turbulent premixed CH_4/H_2/air flames. The model solves the progress variable equation, and the reaction rate source term is modelled with an algebraic closure which is a function of a turbulent flame speed. The turbulent flame speed has been derived by building on correlations in the literature, and specifically calibrated against atmospheric spherically expanding turbulent premixed CH_4/H_2/air flame speed measurements including stretch effects. Stretch and heat loss effects, responsible for the correct flame stabilization, are taken into account by means of tabulated laminar consumption speeds. Tabulation is done by solving one-dimensional conservation equations with a detailed chemistry approach in a fresh-to-burnt counter flow flame configuration for different strain and heat loss levels in *CANTERA*. The hydrogen enrichment effect is accounted for by means of an effective Lewis number incorporated into the turbulent flame speed. The model has been implemented in RANS, SAS, and LES context CFD (Computational Fluid Dynamics) simulations, and validated against atmospheric bluff body stabilized turbulent flame experiments ranging from pure methane to pure hydrogen. The performance of the model in flame dynamics predictions has been tested by extracting FTFs (Flame Transfer Functions) and UIRs (Unit Impulse Responses) from SAS and LES simulations and comparing them against those from experiments. Results indicate that the model predicts the correct flame stabilizations for RANS, SAS, and LES contexts and is capable of predicting flame dynamics.

INDEX

Nomenclature

Acronyms

AFSW Algebraic flame surface wrinkling

BML   Bray-Moss-Libby

CFD   Computational fluid dynamics

ExtH$_2$ Extended model for CH$_4$/H$_2$/air mixtures

FSC   Flame speed closure

FTF   Flame transfer function

HTC   Heat transfer coefficient

ITNFS Intermittent turbulence net flame stretch

KPP   Kolmogorov-Petrovskii-Piskunov

LES   Large eddy simulation

LV   Lindstedt-Vaos

RANS Reynolds averaged Navier Stokes

RSM   Reynolds stress turbulence model

SAS   Scale adaptive simulation

SGS   Sub-grid-scale

SI   System identification

TFC   Turbulent flame closure

UIR   Unit impulse response

Scripts

α Thermal diffusivity

β Heat loss parameter

ΔH_c^o Lower heating value of combustion

δ Laminar flame thickness

δ_t Turbulent flame brush thickness

δ_{ij}	Kronecker delta
δ_{L0}	Unstretched adiabatic laminar flame thickness
Δ_{LES}	LES filter length
$\dot{\omega}$	Reaction rate
$\dot{q}$	Total heat release rate per volume
ϵ	Turbulence dissipation rate
η_K	Kolmogorov length scale
Γ_K	ITNFS efficiency function
κ	Flame stretch
μ	Dynamic viscosity
ν	Kinematic viscosity
$\overline{\omega}$	Reaction rate source term
ϕ	Equivalence ratio
ρ	Density
Σ	Flame surface density
Ξ	Flame surface wrinkling ratio
c	Normalized combustion progress variable
Da	Damkohler number
k	Turbulent kinetic energy
Ka	Karlovitz number
l_0	The largest turbulent length scale
L_i	Inner cut-off scale
L_o	Outer cut-off scale
l_t	Turbulent length scale
L_y	Flame surface wrinkling length scale
l_{int}	Turbulent integral length scale
Le^*	Effective Lewis number

Nu Nusselt number

P Pressure

Pr Prandtl number

Ra Rayleigh number

Re Reynolds number

S_c Laminar flame consumption speed

S_t Turbulent flame speed

S_{L0} Unstretched adiabatic laminar flame speed

Sc Schmidt number

T Temperature

u Velocity

$u^{'}$ Turbulent fluctuation velocity

u_{η_K} Kolmogorov velocity scale

Superscripts

$^{-}$ Reynolds averaged/filtered quantity

$^{\sim}$ Favre averaged/filtered quantity

Subscripts

ad Adiabatic property

b, p Burnt, products

$L0$ Unstretched adiabatic

SGS Sub-grid-scale property

st Stoichiometric condition

t Turbulent property

u Unburnt, reactants

INTRODUCTION

1.1. MOTIVATION

In view of the global efforts for the decarbonization of the power generation sector, in recent years, there has been an increased interest in the development of gas turbine engines able to introduce hydrogen blending into the normal natural gas fuel supply. Hydrogen is seen as a promising option to store excess energy produced from renewable sources. Gas turbine engines fed by hydrogen/natural gas could in the future complement the intermittent renewable power supply by working as back-up power during periods of scarce wind and daylight [1, 2]. However, current lean premixed combustor technologies are not yet able to handle reliably the full range of 0–100% hydrogen contents blended with natural gas.

One challenge in the development of such systems (see Figure 1.1) is to predict the flame stabilization and dynamics inside the combustion chamber when hydrogen, which has a higher reactivity than natural gas, is added to the fuel. In lean-premixed combustors, flames are stabilized by recirculating hot gases with the help of bluff-bodies and/or swirlers. Depending on the interplay between hydrogen addition, heat losses and flame stretch in the hot gas recirculation zones, different flame stabilization shapes can be present in a combustor (see [3] for bluff body stabilized and [4, 5] for swirl stabilized flames).

Conventional combustion modelling approaches have mainly been developed for fuels like CH_4 or natural gas having unity Lewis number (Le) and may lead to inaccurate results when used for H_2 or H_2 blended ($Le < 1$) fuels. Additionally, reliable modelling approaches require to consider stretch and heat loss effects to predict the correct flame stabilization shape [6–9] which is crucial for the prediction of the flame dynamics response [5, 10, 11]. To this end, this study aims at predicting correct flame stabilization shapes and accordingly the flame dynamics for CH_4/H_2/air flames by combining the stretch and heat loss effects with an effective Lewis number approach in the modelling closure.

1.1.1. Combustion and flame

Combustion takes place when fuel, oxidizer, and a sufficient amount of energy (activation energy) are provided. Conversion of reactants into combustion products can be described by an overall unique one-step reaction of the form [13]:

$$n_f F + n_o O \rightarrow n_p P \tag{1.1}$$

where n refers to mole number and subscripts f, o and p refer to fuel F, oxidizer O and product P, respectively. The mixture is at stoichiometric condition when reactants (fuel and oxidizer) are consumed completely. The equivalence ratio, which is an important measure in combustion for deciding whether the mixture is at lean (excess in oxidizer) or rich (excess in fuel) condition,
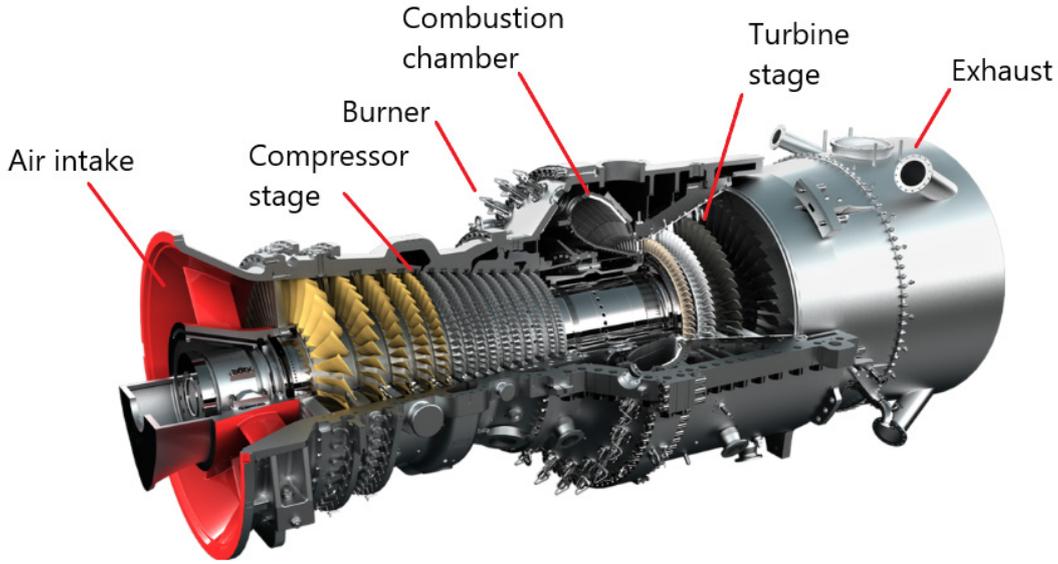
Figure 1.1: Ansaldo Energia AE94.3A gas turbine [12].

is defined as follows:

$$\phi = \frac{Y_f}{Y_{f,st}} = \frac{X_f}{X_{f,st}} \tag{1.2}$$

where $Y_f = m_f/(m_f + m_o)$ denotes the fuel mass fraction (known also as the mixture fraction), $X_f = n_f/(n_f + n_o)$ denotes the fuel mole fraction and the subscript st stands for the stoichiometric condition. The equivalence ratio remains the same independently from the evaluation done based on mass or mole, and its value indicates whether the mixture is lean ($\phi < 1$), stoichiometric ($\phi = 1$), or rich ($\phi > 1$).

In terms of the mixing state of fuel and oxidizer, flames can be classified as non-premixed (diffusion) or premixed flames (see Figure 1.2). In diffusion flames, fuel and oxidizer are stored separately, they mix and burn at the same time and the flame occurs at the isosurface of the stoichiometric condition, while in premixed flames fuel and oxidizer are stored as a premixed mixture and they burn afterward [13].

Figure 1.3 shows the structure of a laminar premixed flame. Fresh (fuel and oxidizer premixed mixture) and burnt (combustion products) gases are separated by the flame. Mixture equivalence ratio ϕ remains constant and the mixture can burn at any ϕ value provided that ϕ does not exceed the lean ($\phi \approx 0.3 - 0.7$ depending on fuel) or rich ($\phi \approx 2 - 4$ depending on fuel) extinction limits [13]. Laminar premixed flames can be characterized by the laminar flame speed (or laminar consumption speed) S_c and the laminar flame thickness δ. These are the referential parameters for freely propagating (unstretched) laminar premixed flames (see Figure 1.3) under adiabatic conditions and depend only on the chemical kinetics and transport properties (thermal diffusion) of the mixture. Across the flame thickness, a strong temperature gradient occurs which heats up the unburnt mixture through thermal diffusion and causes ignition resulting in flame propagation towards the unburnt mixture at a laminar flame speed. The

premixed flame   diffusion flame

post flame
oxidation
and radiation   post flame
                                  radiation

                 surface of
                 stoichiometric
                 mixture
                 $\phi = 1$

premixed
flame front

$S_c = u_n$

                 air   air

fuel + air   fuel
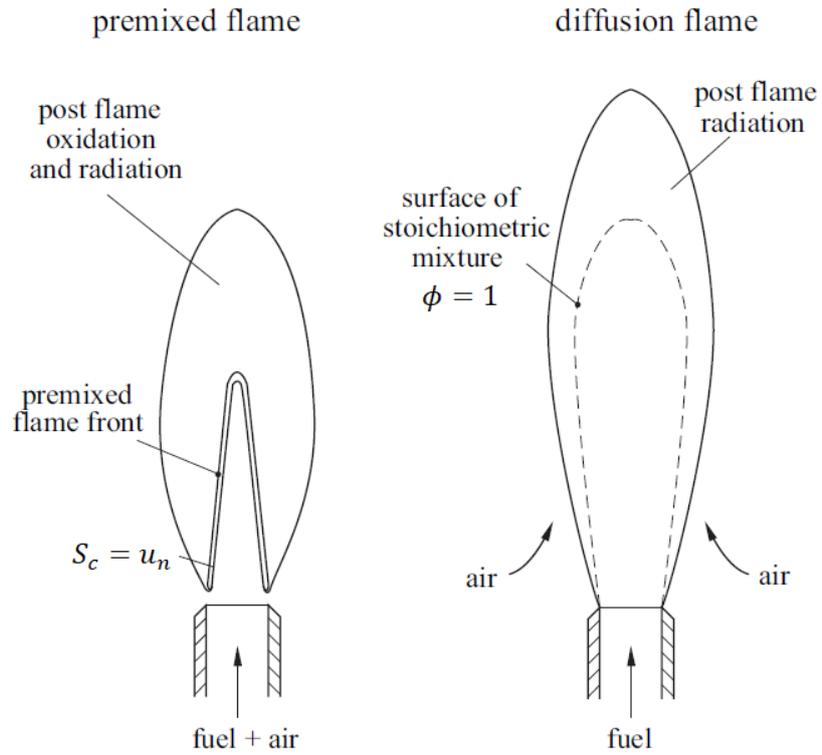
Figure 1.2: Laminar premixed and diffusion flames. Figure is adapted from [14].

S_{L0} flame

fresh gases
(fuel and oxidizer)   burnt gases

δ_{L0}

                                  temperature

fuel

oxidizer   reaction rate

preheat   reaction
zone   zone
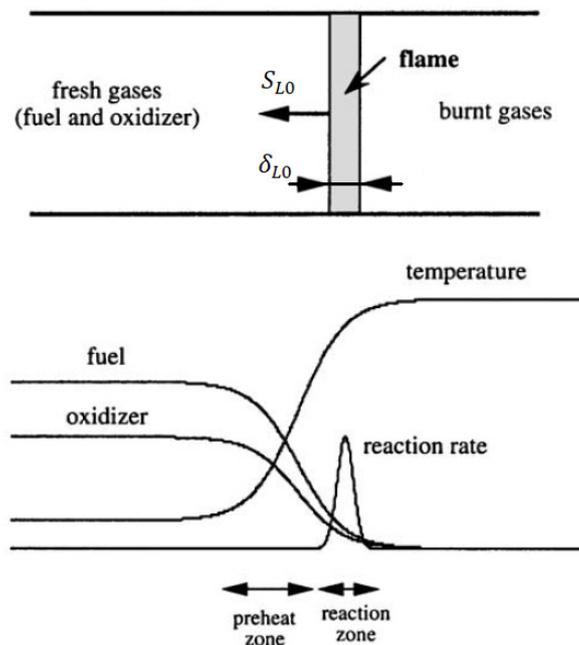
Figure 1.3: Adiabatic freely propagating laminar premixed flame structure. Figure is adapted from [15].

premixed flame stabilizes in steady state condition at a location where the local laminar flame speed S_c is equal to the local flow velocity normal to flame front u_n (see Figure 1.2). The referential quantities, the laminar flame thickness δ_{L0} and the laminar flame speed S_{L0} are defined as follows [13, 15]:

$$\delta(\kappa = 0, \beta = 1) = \delta_{L0} = \frac{T_{ad} - T_u}{max(dT/dx)} \tag{1.3}$$

$$S_c(\kappa = 0, \beta = 1) = S_{L0} = \frac{1}{\rho_u Y_f} \int_{-\infty}^{\infty} \dot{\omega} \, dx \tag{1.4}$$

where $\kappa = 0$ and $\beta = 1$ indicate the unstretched and adiabatic condition (freely propagating flame) with the subscript $L0$ referring to this condition, and $\dot{\omega}$ is the reaction rate.
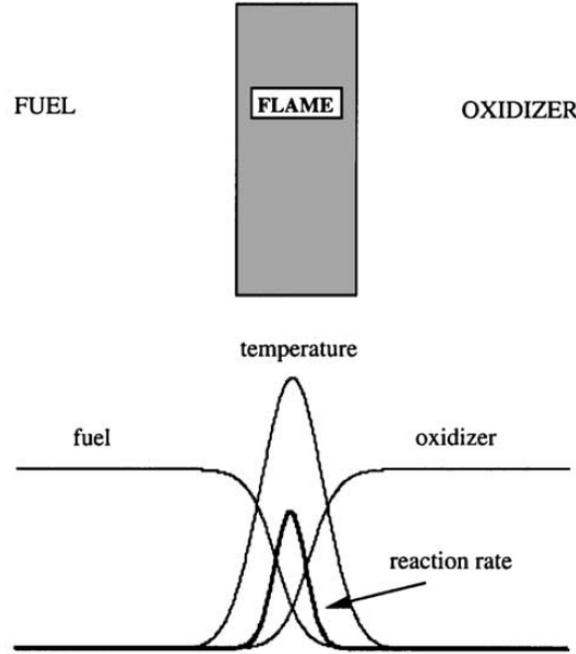
Figure 1.4: Laminar diffusion flame structure. Figure is taken from [15].

Figure 1.4 shows the diffusion flame structure. The flame separates the fuel and oxidizer and occurs at the $\phi = 1$ isosurface (stoichiometric condition). The reaction rate is controlled by the molecular diffusion of the reactants toward the reaction zone. Flame cannot propagate towards the fuel/oxidizer side due to a lack of sufficient oxidizer/fuel, resulting in less efficiency. Since the reaction rate is controlled by the mixing state, it does not exhibit referential flame speed as in premixed flames. The diffusion flame is an unsteady flame and stabilizes in a steady condition if and only if the stretch applies, otherwise, the flame spreads with time by the effect of thermal and molecular diffusion and gets thickened [13]. Due to this, the unstretched diffusion flame does not have a referential flame thickness.

Conventional industrial burners are usually designed for premixed flames due to their higher efficiency. However, supplying a mixture in perfectly premixed condition to industrial-scale

combustion chambers is not easy, and the fuel and oxidizer are supplied separately to a mixing chamber before entering into the combustion chamber, resulting in a technically or partially premixed mixture. Flame characteristics occurring in partially premixed mixtures can be regarded as the combination of premixed and non-premixed flame characteristics. The flame can propagate towards the unburnt mixture as in premixed flame, the equivalence ratio varies in the mixture as in diffusion flames, but the mixture does not necessarily burn close to the stoichiometric ratio ($\phi = 1$), instead, it can burn at any equivalence ratio as in premixed flames. In this study, our focus is limited to premixed flames.

Turbulence affects combustion and alters the reaction rate. Turbulent eddies interact with the flame front and induce flame stretch. Stretch alters the reaction rate, and, depending on the fuel type, may increase or decrease the local reaction rate. At extreme values, the stretch can even cause quenching of the flame. Besides this, turbulent eddies wrinkle the flame surface which results in the increment of flame surface area and accordingly the enhancement in the global reaction rate.

1.1.2. Stretch, heat loss and flame stabilization

Flame stretch κ is defined as the fractional rate of change of the flame surface area $A(t)$ (see Figure 1.5). The flame front, propagating in non-uniform flow, is exposed to strain and curvature effects which lead to change in the flame surface area. This change is measured by the stretch [13].

$$\kappa = \frac{1}{A}\frac{dA}{dt} \tag{1.5}$$
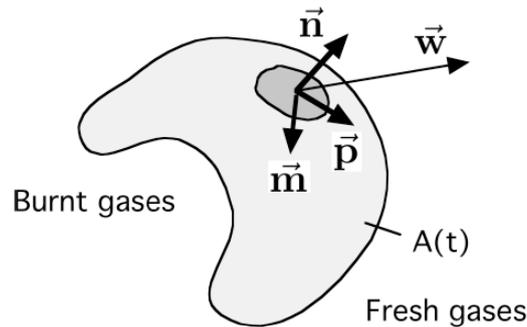
Figure 1.5: Definition of flame stretch. Figure is adapted from [13].

A general expression for the stretch applying to a thin flame sheet is given by Candel and Poinsot [13, 16] as follows:

$$\kappa = (\delta_{ij} - n_i n_j)\frac{\partial w_i}{\partial x_j} \tag{1.6}$$

where δ_{ij} is the Kronecker delta, n_i is the component of the flame surface normal vector, and w_i is the component of the flame front velocity vector which is defined as follows:

$$\vec{w} = \vec{u} + S_d\vec{n} \tag{1.7}$$

where $\vec{u}$ is the flow velocity vector and S_d is the displacement speed accounting for the effects of flow on the flame structure. Substitution of Eq. 1.7 into Eq. 1.6 is given as follows [13]:

$$\kappa = (\delta_{ij} - n_i n_j)\frac{\partial u_i}{\partial x_j} + S_d\frac{\partial n_i}{\partial x_i} \tag{1.8}$$

In Eq. 1.8, the first term on the right hand side (RHS) represents the contribution from the flow strain, and the second term (the term with S_d) represents the contribution from the flame curvature. In the scope of this thesis study, the contribution of curvature on the mean flame stretch is assumed to be small, which is a valid assumption in highly turbulent flows [17, 18], and strain is only considered to define the mean flame stretch (i.e. the stretch and strain yield the same value), thus, the Eq. 1.8 reduces to the following:

$$\kappa = (\delta_{ij} - n_i n_j)\frac{\partial u_i}{\partial x_j} \tag{1.9}$$

Stretch alters the local reaction rate and can cause quenching at extreme values. The value at which the flame quenching occurs is defined as the extinction limit of stretch and decreases with the presence of heat losses. The combined effect of stretch and heat loss is responsible for the flame quenching and defines the flame stabilization shape in the combustors [6–9]. Studies (see for example [3–5] among many others) have shown that depending on the interplay between heat losses, flame stretch and hydrogen content in the fuel, flames in lean premixed combustors may stabilize in different shear layer regions (see Figure 1.6) producing M-type, V-type or detached-type mean-flame shapes (see Figure 1.7).
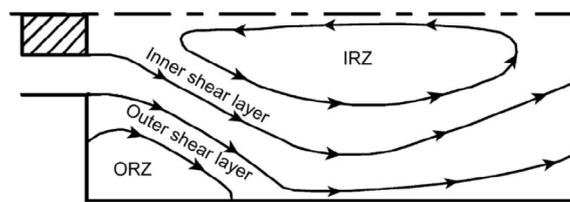
Figure 1.6: Inner (IRZ) and outer recirculation zones (ORZ) in gas turbine combustors. Figure is taken from [7].

In Figure 1.7 a) flame stabilizes at the inner and outer shear layers producing M-flame shape, which is generally seen under adiabatic conditions, in b) flame stabilizes at the inner shear layer but cannot resist stretch and heat loss at the outer shear layer, produces V-flame shape, and in c) stretch exceeds the extinction limit at the centerbody additional to the outer shear layer, causing a detached flame which stabilizes at the vortex breakdown bubble [19]. The extinction limit of stretch depends on the mixture composition (hydrogen content in the fuel), and increases as the mixture Lewis number decreases with the hydrogen addition [20].
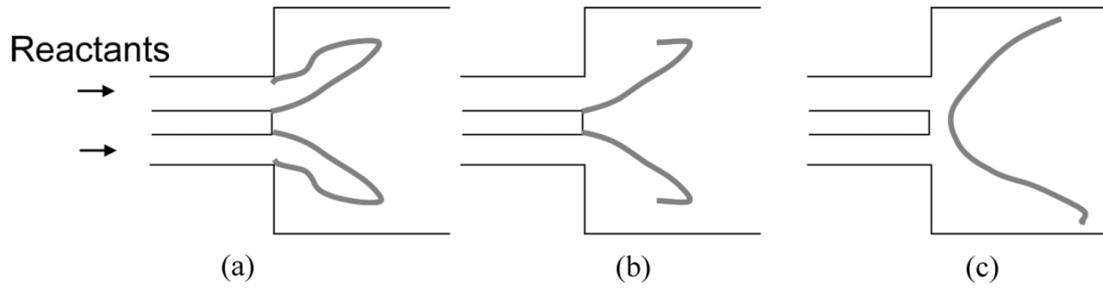
Figure 1.7: Three possible flame stabilizations in gas turbine combustors: a) M-flame, b) V-flame and c) detached flame. Figure is taken from [19].

1.1.3. Hydrogen enrichment effects

Lewis number Le is defined as the ratio of mixture thermal diffusivity to molecular diffusivity of a specie:

$$Le_k = \frac{\alpha_{mix}}{D_k} \qquad (1.10)$$

where subscript k refers to specie index, α_{mix} is the thermal diffusivity of the premixed fuel oxidizer mixture, and the fuel molecular diffusivity D_k is generally calculated from the binary mass diffusion coefficient between the fuel specie k and the excess inert gas N_2. Lewis number is around unity $Le \approx 1$ for methane flames and around $Le \approx 0.3$ for hydrogen flames.
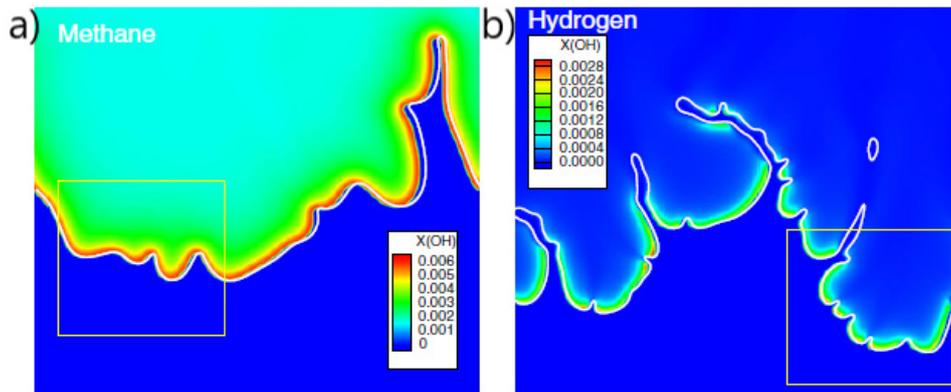
Figure 1.8: OH mole fraction (marker of the reaction zone) contours for a) CH_4/air ($Le \approx 1$) and b) H_2/air ($Le < 1$). White lines represent the flame location. Bottom: unburnt reactants, top: burnt products. Figure taken from [21].

Figure 1.8 shows the flame front reaction rate distribution for methane ($Le \approx 1$) and hydrogen ($Le \approx 0.3$) flames from a two-dimensional direct numerical simulation (DNS) study [21] under turbulent conditions. Considering positive curvature as convex towards unburnt reactants and negative curvature is the opposite, both flames have positive and negative curvatures. However, the methane flame has a smoother flame front with equi-sized and equi-distributed radius

of curvatures in positive and negative direction, the hydrogen flame has steeper negative curvatures and smoother positive curvatures. In the hydrogen flame front ($Le < 1$), the reaction rate increases at positive and decreases at negative curvatures, while it remains constant for the methane flame ($Le \approx 1$). These reaction rate variations in the hydrogen flame are known as the Lewis number effect (or preferential diffusion effect) in the literature and are sourced from the difference between the mixture thermal diffusivity α_{mix} and hydrogen mass diffusivity D_{H_2}.

Figure 1.9 schematizes the hydrogen flame front for explaining the phenomenon. Due to the higher molecular diffusivity of hydrogen compared to mixture thermal diffusivity ($D_{H_2} > \alpha_{mix}$), as the unburnt H_2/air mixture approaches the negatively curved flame front (concave towards the fresh mixture), the hydrogen molecules diffuse towards positive curvatures (convex towards the fresh mixture) at either side, by the effect of the thermal diffusion layer. This causes local enrichment at the positively curved regions and results in a locally leaner mixture at the negatively curved region downstream. Enhanced diffusion towards positive curvatures consumes most, even all of the hydrogen in the flow pathline before reaching the negatively curved flame front, causing reduced reaction rate or extinction of the flame at the negative curvature and the enhanced reaction rate at the positive curvature. With the extinction, positively curved flame fronts combine and form a bigger positive curvature. This phenomenon continuously repeats over the wrinkled flame surface and causes thermodiffusively unstable flame front. Overall, these instabilities cause enhancement in the flame surface area and consequently in the global reaction rate in hydrogen flames [21].
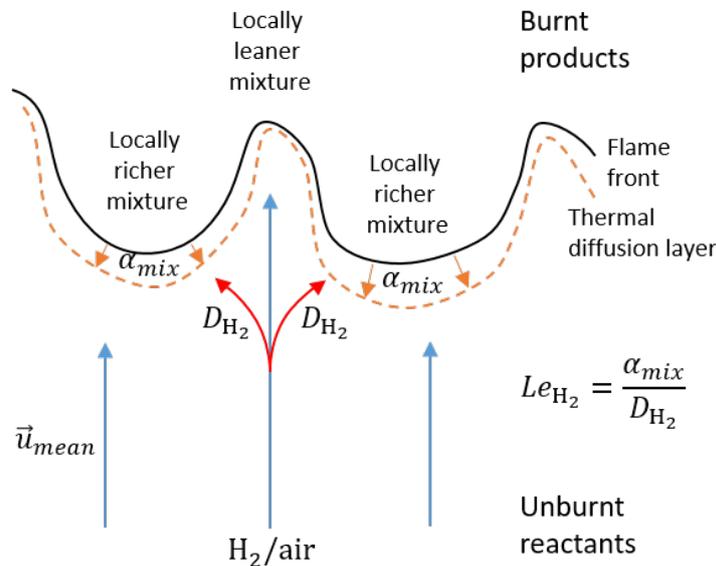
Figure 1.9: Preferential diffusion of hydrogen ($Le < 1$).

On the other hand, the high reactivity of hydrogen is not a consequence of only the thermodiffusive instabilities, but also the consequence of its burning chemistry. Figure 1.10 shows the laminar flame speed S_{L0} of different fuels against equivalence ratio at the unburnt mixture temperature and operating pressure of a conventional gas turbine inlet conditions. As observed, the reactivity of hydrogen significantly differs from the other fuels, including its own blend with methane in 50-50%$_{vol}$ blending ratio. From 50%$_{vol}$ to pure hydrogen, the flame speed increases

to its tenfold, and this enhancement is solely the consequence of hydrogen burning chemistry.
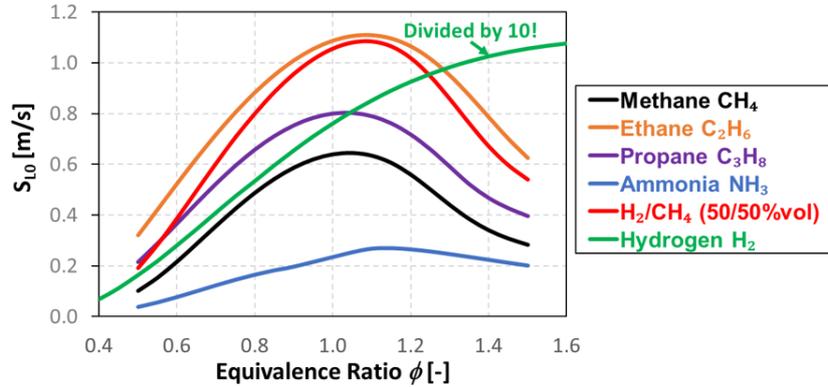
Figure 1.10: Laminar flame speeds of different fuels at various equivalence ratios. Calculated in *CANTERA* with GRI-Mech 3.0 [22] detailed chemistry mechanism in '*FreeFlame*' configuration at unburnt mixture conditions of $T_u = 723\ K$ and $P = 20\ bar$.

1.1.4. Flame transfer function

The flame transfer function (FTF) represents the dynamic response of the flame to acoustic perturbations. It is defined as the ratio of heat release rate fluctuations to velocity fluctuations, in the frequency domain. Its gain (magnitude) indicates the intensity of heat release rate fluctuations and its phase (angle) provides information about the time delay.

$$FTF(\omega) = \frac{Q(\omega)/\overline{Q}}{\hat{u}_{ref}(\omega)/\overline{\hat{u}}_{ref}} \tag{1.11}$$

In Eq. 1.11, Q and $\hat{u}_{ref}$ refer to the instantaneous values of the volume integrated heat release rate and the mass-weighted averaged axial velocity at the reference plane chosen upstream of the flame, respectively. ω refers to the angular frequency ($\omega = 2\pi f$), and $^{—}$ refers to the mean value.

The flame transfer function has crucial importance in thermoacoustic studies. It is the key element of the thermoacoustic network models [23, 24] and represents the flame as a nonlinear function. Thus, it is a determinant parameter to test the dynamic performance of combustion models.

1.1.5. State of the art and objective

As emphasized above, stretch, heat loss and Lewis number effects are responsible for the correct flame stabilization shape. Regarding this, several efforts have been made in the literature to take into account these effects. These studies are briefly reviewed below, and the objective of the current study is stated in the end.

Mercier et al. [25] investigated the impact of heat loss in the FTACLES (Filtered Tabulated Chemistry for LES) combustion modelling approach for 60% and $90\%_{vol}$ H_2 in fuel for CH_4/H_2/air premixed swirl flames. They included the heat loss effects in the chemistry tabulation but did not account for the stretch effects. The inclusion of heat loss effects produced flame stabilization in agreement with experiments. However, it was pointed out that the model could be improved by explicitly modelling the effect of flame stretching. Chatelier et al. [26] used the same approach and burner configuration for $60\%_{vol}$ H_2 content in fuel for CH_4/H_2/air premixed flame to extract FTFs. Despite reasonably well-predicted mean flame shape and FTF, excluding explicit modelling of flame stretch caused over-predicted heat release rates at the outer shear layer.

Agostinelli et al. [27, 28] used DTFLES (Dynamically Thickened Flame LES) approach with analytically reduced chemistry to simulate partially premixed CH_4/H_2/air flames up to $50\%_{vol}$ H_2 content in the *PRECCINSTA* gas turbine model combustor. The intrinsic inclusion of heat loss in the DTFLES approach allowed them to predict correctly the thermo-acoustic instabilities seen experimentally at the highest hydrogen content investigated. Garcia et al. [29] used a similar modelling approach for extracting FTFs from CH_4/H_2/air premixed flames up to $67\%_{vol}$ H_2 content in the *Norwegian University of Science and Technology (NTNU)* single sector laboratory scale burner. They calibrated a three-step global mechanism for lean methane-hydrogen mixtures following [30] and used it in the DTFLES model with enabled radiation and conjugated heat transfer. Including heat loss allowed them to predict the correct flame stabilization shapes and FTFs measured from experiments.

Tay-Wo-Chong et al. proposed extensions to Zimont's turbulent flame speed closure (TFC) model [31] and Schmid's [32] reaction rate closure in RANS [6, 7] and later in LES [8], to account for the stretch and heat loss effects in CH_4/air turbulent premixed flames. These effects were accounted for by tabulating laminar consumption speed values calculated in fresh-to-burnt counterflow premixed flames at different levels of stretch and heat losses. These models were tested against experimental data of a swirl stabilized perfectly premixed atmospheric combustor [24] achieving satisfactory predictions of mean flame shapes and flame dynamics. The extended TFC model was also later used by Nassini et al. [33] in LES simulations aimed at predicting flame stabilization up to lean blow-out (LBO) in both a laboratory scale and an industrial gas turbine combustors.

Klarmann et al. [34, 35] in the RANS context and Tang et al. [9] in the LES context applied a similar laminar consumption speed tabulation approach to include the effects of stretch and heat loss in flamelet generated manifold (FGM) modelling. They compared the predicted flame topologies to those from experiments and those from the cases without including stretch and heat loss effects. Comparisons showed that including stretch and heat loss effects improves the accuracy of the predictions providing better agreements with experiments.

Dinkelacker et al. [36] proposed an algebraic expression to calculate an effective Lewis number for the CH_4/H_2/air flames and incorporated it into a TFC-based modelling approach [37] in RANS context. This approach allowed them to predict the flame length shortening effect as the hydrogen content in the fuel was increasing up to $40\%_{vol}$ in a Bunsen type burner [38] at elevated pressure. This approach was later used in other RANS and LES studies [39–41].

Combustion models mentioned above, can be classified as either RANS or LES-based models and translating from one to the other either brings some difficulties or is not possible. TFC-

based models, which were developed for RANS, require an update in the model coefficient for its application in LES [39, 42, 43], and tuning the coefficient may require a set of LES calculations [39]. On the other hand, FTACLES and DTFLES models are developed for LES and require resolved scales for modelling the combustion. Amongst the others, FGM approach, owing to its presumed PDF (Probability Density Function) based closure, is applicable in both RANS and LES context CFDs without a problem in the sense of turbulent chemistry interaction. However, in the FGM model, the manifold generation is done on a discretized space for the progress variable, and the effort required for the generation of the manifolds increases considerably when the stretch and heat loss are added as additional dimensions, making the approach impractical[1] for including stretch and heat loss effects.

In this regard, this study aims at proposing a practical modelling approach for RANS, SAS and LES context CFD simulations of CH_4/H_2/air premixed flames up to pure hydrogen, for reproducing the correct flame stabilizations and dynamics, without requiring further tuning in the model coefficient. To this end, it combines the stretch and heat loss modelling approach from [6, 8] with an effective Lewis number expression from [36] in an algebraic modelling closure. The resulting model is validated for its predictions of the flame stabilization shapes and FTFs measured in the *NTNU* atmospheric single sector bluff body stabilized test rig [3] for the CH_4/H_2/air premixed flames from pure methane to pure hydrogen.

1.2. STRUCTURE OF THE WORK

The thesis is structured as follows. In Chapter 2, the fundamental concepts of turbulent premixed combustion and the modelling approaches relevant to this work, are described. In Chapter 3, the proposed turbulent premixed combustion modelling approach is explained. In Chapter 4, the experimental setup, where the data used for the validation of CFD studies is produced, is briefly described. The details of the numerical setups used in CFD simulations are presented. The cold flow results for RANS, SAS and LES are presented, and the tabulated look-up tables are plotted. In Chapter 5, the results for the mean flame shape stabilizations are presented. In Chapter 6, the CFD-SI methodology for FTF extraction is explained, and the dynamic performance of the proposed modelling closure is investigated by means of FTF and UIR comparisons with those from experiments. Finally, the thesis is concluded in Chapter 7, with outcomes and outlooks.

---

[1]Klarmann et al. proposed a workaround for facilitating the stretched and non-adiabatic manifold generation for CH_4/air premixed flames [34, 35] .

TURBULENT PREMIXED COMBUSTION

This chapter overviews the fundamental concepts and modelling approaches for turbulent premixed combustion. First, turbulence characteristics and the turbulent energy spectrum (energy cascade) concept are described. Then the turbulent premixed regime diagram, the turbulent flame speed, the fractal theory and the flame surface density are explained. Following this, fundamental governing equations for reacting flow in averaged/filtered form are presented. Finally, in the last two sections, RANS, SAS and LES turbulence modelling approaches and the RANS-based turbulent premixed combustion modelling approaches benefited in this study are presented.

2.1. TURBULENCE

Turbulence is characterized by an unsteady, energetic, irregular, random, and chaotic behaviour of the flow. Characteristics of turbulent flows are listed as follows [44]:

- Irregular: The flow exhibits nonlinear random velocity and vorticity fluctuations at different scales.

- Diffusive: All turbulent flows are diffusive (e.g. spreading velocity and vorticity fluctuations through the surrounding fluid) which causes rapid mixing by enhancing momentum, heat and mass transfer. If a flow is chaotic but not diffusive, it is not turbulent.

- Energetic: Turbulence always occurs at high Reynolds numbers with high kinetic energy, where the inertial forces of the flow prevail over the viscous forces.

$$Re = \frac{uL_{char}}{\nu} \qquad (2.1)$$

- Three-dimensional: Turbulent flows are always three-dimensional, exhibiting vorticity fluctuations additional to velocity fluctuations.

- Dissipative: Turbulence is always dissipative. Viscous shear stresses cause deformation work that raises the internal energy of fluid at the expense of turbulent kinetic energy. A continuous energy supply is needed to compensate for these viscous losses. If no energy is supplied, turbulence decays rapidly. Random motions without viscous losses (non-dissipative character) are not turbulent though they can be dispersive [44].

- Continuum phenomenon: It is a continuum phenomenon, even the smallest scales of turbulence are far larger than the molecular scale.

- Flow feature: It is the feature of a flow, rather than a feature of a fluid.

2.1.1. Scales of turbulence and energy cascade

Turbulence involves different scales of irregular vortexes (eddies) whose size differs from the very large scales comparable to the characteristic scale of the flow L_{char} (i.e. the width of the flow) to the smallest scales (Kolmogorov scale η_K), which are not recognizable to the naked eye [44]. Large-scale eddies are unstable and transfer their energy by breaking up into smaller ones, these small eddies follow a similar break-up process and transfer their energy to smaller ones, and this continues until the energy of the smallest-scale eddies is not sufficient to transfer any further, and the energy at this scale is dissipated by the viscosity [45].

Figure 2.1 shows the sampled velocity signal at a reference point in a turbulent field. The decomposition of turbulent velocity u into mean $\overline{u}$ and fluctuating part u' is known as the Reynolds decomposition $u = \overline{u} + u'$, and is used widely in turbulence studies. The turbulent kinetic energy k is defined with the help of Reynolds decomposition as follows [45].

$$k = \frac{1}{2}\overline{u_i' u_i'} \tag{2.2}$$
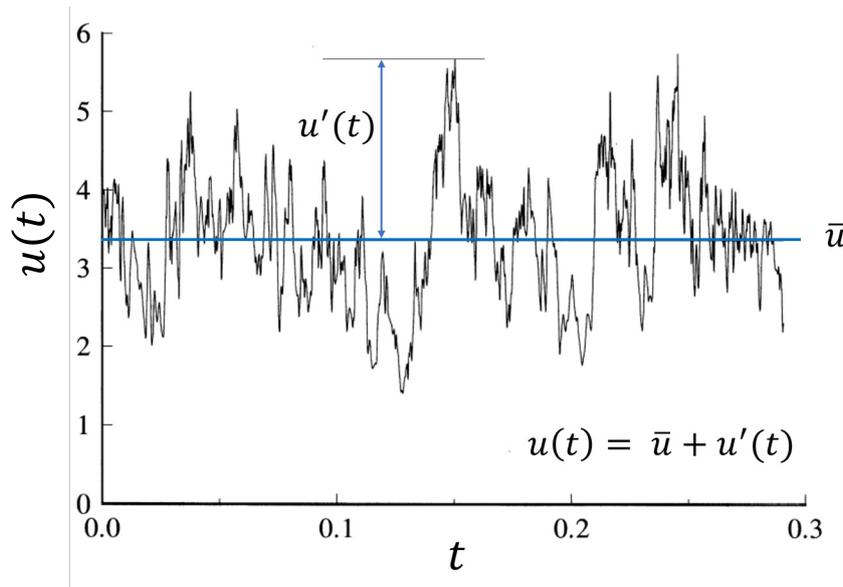
Figure 2.1: Sampled velocity signal at a reference location in a turbulent field. Figure is modified from [45]

Turbulent energy spectrum or in other words the energy cascade is a useful concept that describes the turbulent kinetic distribution at different scales of eddies starting from its production at large scales to the dissipation at small scales in a fully turbulent flow. An illustration of the energy cascade is given in Figure 2.2, the turbulent kinetic energy defined in Eq. 2.2 corresponds to the integration of energy $E(m)$ over all the wavenumbers m as given below [45].

$$k = \frac{1}{2}\overline{u_i' u_i'} = \int_0^\infty E(m)\, dm \tag{2.3}$$
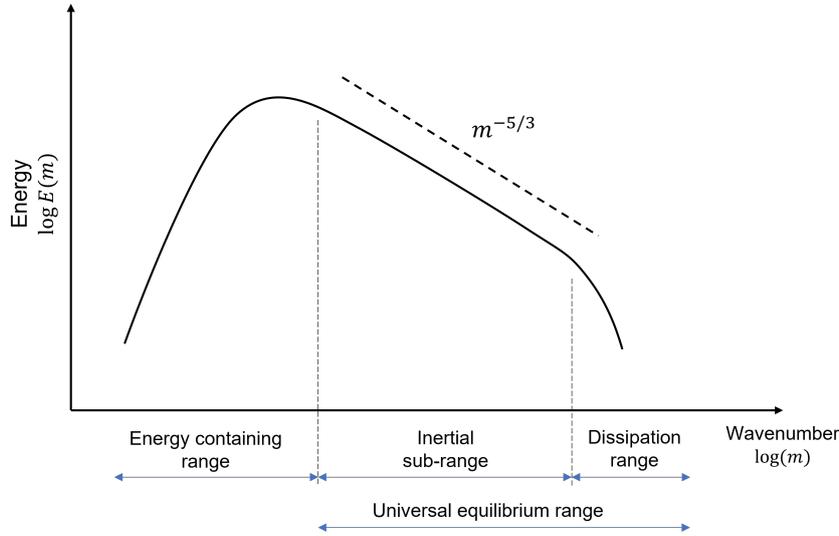
Figure 2.2: Turbulence energy spectrum (energy cascade).

As observed from Figure 2.2, the energy spectrum is divided into three ranges. The energy-containing range, where the turbulent kinetic energy is produced, includes the largest-size eddies whose scales are comparable to the characteristic scale of the flow. In this range, the eddy motions are determined by the mean flow field and the large-scale eddies exhibit anisotropic behavior that their character differs from one flow to the other [45].

The inertial subrange and the dissipation range together, form the universal subrange of turbulence. As the name suggests, in these ranges anisotropy gets lost and eddies exhibit a universal behavior that their statistics are similar in every high Reynolds flow.

The inertial subrange is the largest range of turbulence. It includes much smaller eddies than those in the energy-containing range, and much larger eddies than those in the dissipation range. However, these eddies still have sufficient energy to prevail over viscous forces, and viscous effects are negligible. In this range, the characteristics of eddies are determined by the inertial effects only [45]:

$$\epsilon = \frac{u^{'}(l_{int})^3}{l_{int}} \tag{2.4}$$

where $u^{'}(l_{int})$ and l_{int} are the velocity and length scale of the eddy, respectively, in the inertial subrange, and ϵ is the turbulent dissipation rate. As revealed by Kolmogorov, the energy dissipation rate follows Kolmogorov's $-5/3$ law (see Figure 2.2) with the energy spectrum given as follows [45]:

$$E(m) = C\epsilon^{2/3}m^{-5/3} \tag{2.5}$$

where C is a constant.

The dissipation range, where the viscous effects are dominant, contains the smallest size eddies with the lowest level of energy. In this range, the turbulent kinetic energy strongly decays due to viscous effects. The scales (Kolmogorov scales) for length, velocity and time in this range are given as follows [45]:

$$\eta_K = \left(\frac{\nu^3}{\epsilon}\right)^{0.25} \tag{2.6}$$

$$u_{\eta_K} = (\epsilon\nu)^{0.25} \tag{2.7}$$

$$\tau_{\eta_K} = \left(\frac{\nu}{\epsilon}\right)^{0.5} \tag{2.8}$$

2.2. TURBULENT PREMIXED FLAMES

Turbulence alters the flame structure through the interactions between the eddies and the flame front. The classification of these interactions based on referential parameters of turbulence (i.e. turbulent length scale and fluctuation velocity) and premixed flame (i.e. unstretched adiabatic laminar flame speed and thickness) leads to turbulent premixed combustion regime diagrams (see Figure 2.3). Depending on the interactions between turbulent length scale, turbulent fluctuation velocity, laminar flame speed, and laminar flame thickness, different flame structures with different characteristics develop. The flames with similar structure and character are gathered under a representative regime which helps to develop regime-specific combustion models [13].

In regime diagrams, the turbulence length scale is defined from the turbulent integral length scale l_{int} and the laminar flame thickness is defined from the diffusion flame thickness $\delta_{L0,d}$ as follows:

$$l_{int} = \frac{u'^3}{\epsilon} \tag{2.9}$$

$$\delta_{L0,d} = \frac{\alpha_u}{S_{L0}} \tag{2.10}$$

In order to classify the regimes, another flame thickness denoting the reaction zone thickness is defined as $\delta_r \approx \delta_{L0,d}/10$, and the non-dimensional numbers are defined as follows [13]:

- Damköhler number:
$$Da = \frac{\tau_{int}}{\tau_c} = \frac{l_{int}/u'}{\delta_{L0,d}/S_{L0}} \tag{2.11}$$

- Karlovitz number:
$$Ka = \frac{\tau_c}{\tau_{\eta_K}} = \frac{\delta_{L0,d}/S_{L0}}{\eta_K/u_{\eta_K}} \tag{2.12}$$

- Karlovitz number based on reaction zone thickness:
$$Ka_r = \frac{\delta_r/S_{L0}}{\eta_K/u_{\eta_K}} \approx \frac{Ka}{100} \tag{2.13}$$

- Turbulent Reynolds number:

$$Re_t = Da^2 Ka^2 = \frac{u'}{S_{L0}} \frac{l_{int}}{\delta_{L0,d}} \tag{2.14}$$

where τ_c and τ_{int} are the chemical and turbulent integral time scales, respectively.

The regimes are explained as follows [13, 14]:
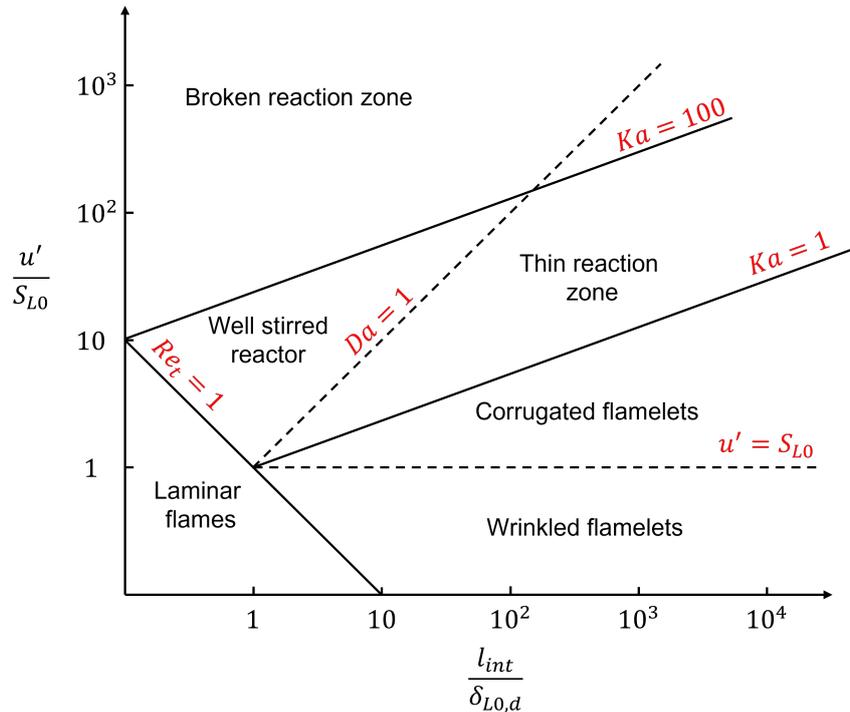
Figure 2.3: Turbulent premixed combustion regimes diagram (log-log scale). Figure is adapted from [14]

- Laminar flame regime ($Re_t < 1$): in this regime flow field is completely laminar.

- Wrinkled flame regime ($Re_t > 1,\ Da > 1,\ Ka < 1$): this regime refers to the very low turbulence level ($u' < S_{L0}$), where the eddies do not have enough energy to compete with the advancement of the flame front. Instead, they can slightly wrinkle the flame front. Thus, the laminar flame propagation dominates over the turbulence effects [14].

- Corrugated flame regime ($Re_t > 1,\ Da > 1,\ Ka < 1$): in this regime turbulent velocity is higher than the laminar flame speed $u' > S_{L0}$, and the laminar flame thickness is smaller than the Kolmogorov scale $\delta_{L0,d} < \eta_K$. The Kolmogorov-size eddies cannot diffuse into the flame but wrinkle the flame front. The flow is quasi-laminar [14].

- Thin reaction zone ($Re_t > 1,\ Da > 1,\ 1 < Ka < 100$): in this regime, the chemical time scale is bigger than the Kolmogorov time scale but lower than the turbulent integral time scale ($\tau_{\eta_K} < \tau_c < \tau_{int}$). The laminar flame thickness is larger than the Kolmogorov scales ($\delta_{L0,d} > \eta_K$) so the Kolmogorov eddies can penetrate into the diffusion zone $\delta_{L0,d}$ but not
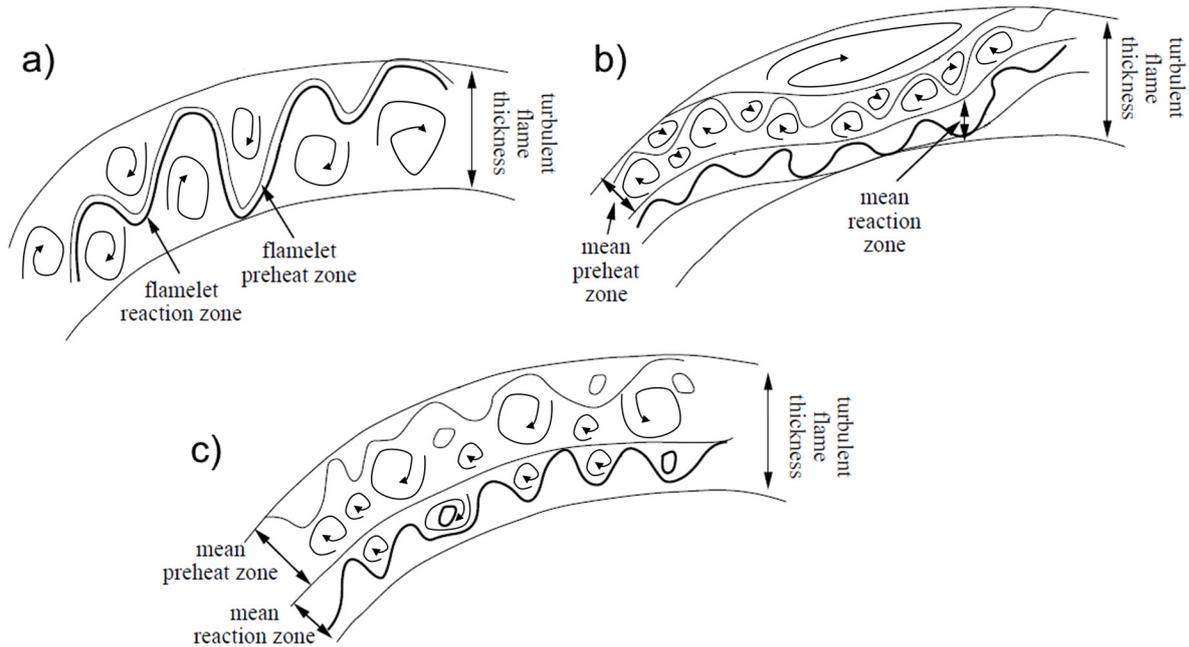
Figure 2.4: Illustrations of a) the wrinkled-corrugated flamelet, b) the thickened wrinkled flame (thin reaction zone and well stirred reactor), and c) the thickened flame (broken reaction zone) structure. Figure is modified from [13].

into the reaction zone δ_r, which causes a thickened wrinkled flame. The flame front does not exhibit laminar characteristics anymore. Large-scale eddies wrinkle the flame, and the flame front eddy interactions induce stretch and may lead to flame quenching [13].

- Well-stirred reactor ($Re_t > 1,\ Da < 1,\ 1 < Ka < 100$): the difference between this regime and the thin reaction zone is that the turbulent integral time scale is lower than the chemical time scale ($\tau_{int} < \tau_c$), so the mixing is fast and the overall reaction rate is limited by chemistry [13].

- Broken reaction zone ($Re_t > 1,\ Da < 1,\ Ka > 100$): this regime is also known as the thickened flame regime where the eddies can penetrate into both diffusion $\delta_{L0,d}$ and reaction zone δ_r, so the flame structure cannot be identified as a thin flame surface anymore [13, 14].

Illustrations of the regimes are given in Figure 2.4. In the regime diagram (Figure 2.3), the combination of the thin reaction zone and well-stirred reactor corresponds to thickened wrinkled flame regime [13, 14] where the most of industrial and academic combustion applications fall [46].
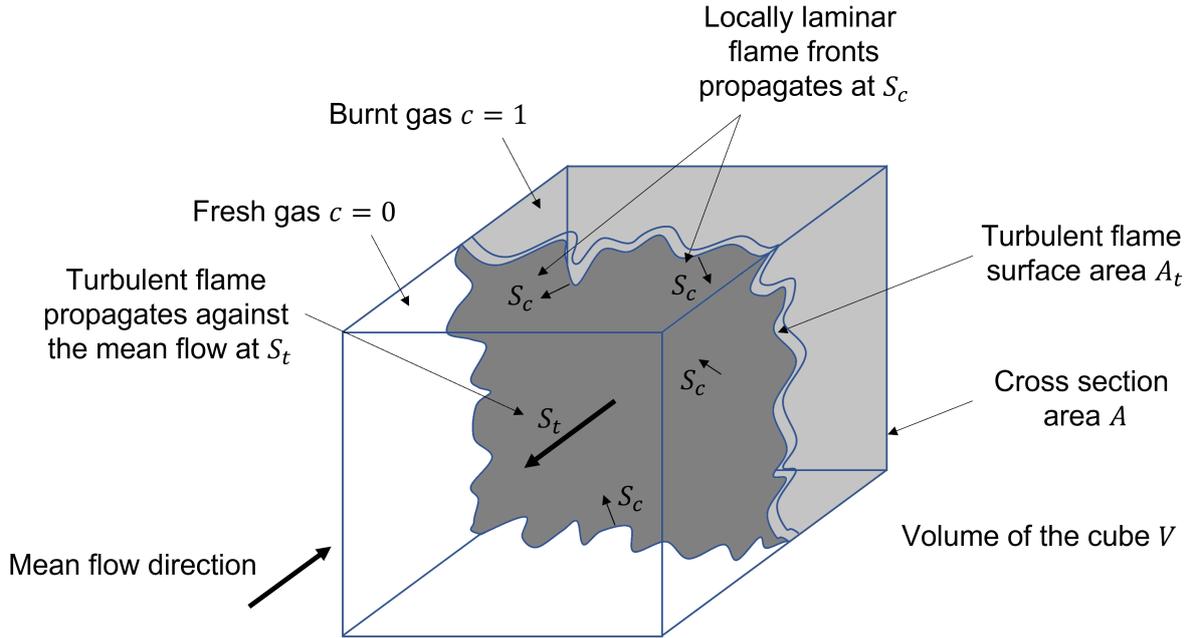
Figure 2.5: Turbulent premixed flame propagation in a unit cube. Figure is modified from [13]

2.2.1. Turbulent flame speed

Turbulent flame speed is an important concept in turbulent premixed combustion. As the laminar consumption speed S_c is responsible for the burning rate in laminar premixed flames, the turbulent flame speed S_t is responsible for the same in turbulent premixed flames. Figure 2.5 illustrates the turbulent premixed flame propagation in a unit cube. The turbulent flame surface is wrinkled and thickened due to flame front eddy interactions, and the total surface area is enhanced. The enhancement in the flame surface area increases the reaction rate ($S_t > S_c$).

According to Damköhler, two different turbulent premixed combustion regimes exist [14]. These are the large-scale and small-scale turbulence levels, corresponding to the corrugated flamelets and the thin reaction zone in the regime diagram (see Figure 2.3), respectively. For these two regimes, he proposed two proportionalities as follows:

$$S_t \propto u', \quad \text{for large-scale turbulence} \tag{2.15}$$

$$S_t \propto S_{L0} \left(\frac{u'}{S_{L0}} \frac{l_{int}}{\delta_{L0,d}} \right)^{1/2}, \quad \text{for small-scale turbulence} \tag{2.16}$$

As seen from Eqs. 2.15 and 2.16, the turbulent flame speed S_t increases with the turbulence fluctuation velocity u', and the proportionality $S_t \propto u'$ differs depending on the combustion regime. Attempts made in the literature to combine Damköhler's correlations into one led to a general expression with an adjustable exponent as follows [13, 14]:

$$S_t = S_{L0} + C S_{L0} \left(\frac{u'}{S_{L0}} \right)^n \tag{2.17}$$

where C is the coefficient, and $n \approx 0.7$ is the exponent ranging between $0.5 < n < 1$, both to be adjusted depending on the regime of interest.

Deriving a relation for the turbulent flame speed is still an active area of combustion research, as is part of the current study too. The proposed expression for the S_t in this study is explained in Chapter 3.

2.2.2. Fractal theory and flame surface density

Gouldin [47] explains the application of the fractal theory to turbulent premixed combustion as follows. The flame is described as a wrinkled isothermal surface in a homogeneous isotropic turbulent field, and this wrinkled roughened surface is considered inside a cubic volume of L_o^3 (similar to Figure 2.5). If this volume is split into smaller cubic cells with a side length of L_i, then the number of small cubic cells N touched by this surface will be proportional to:

$$N \propto \left(\frac{L_o}{L_i}\right)^D \tag{2.18}$$

where D is the fractal dimension converges to 2 for a flat surface, and to 3 for a highly wrinkled surface (in which $D = 3$ means that the flame surface touches all the small cubes). Assuming that the flame surface occupies on average L_i^2 amount of area in each cell, a relation can be expressed for the total surface area A_f by multiplying the number of cells N to L_i^2.

$$A_f = N L_i^2 = L_i^{2-D} L_o^D \tag{2.19}$$

If the total flame surface area A_f in the big cube is divided by the volume of the cube, the resulting expression will refer to the flame surface density Σ having a unit of [m^2/m^3].

$$\Sigma = L_i^{2-D} L_o^{D-3} \tag{2.20}$$

One can multiply the Eq. 2.20 by L_o/L_o, yielding to:

$$\Sigma = \left(\frac{L_o}{L_i}\right)^{D-2} \frac{1}{L_o} \tag{2.21}$$

where the L_i and the L_o are defined as the inner and outer cut-off scales, and $D = 7/3$ is the fractal dimension whose value should be in the range of $2 < D < 3$ [47, 48]. In Eq. 2.21, the first term with exponential $D - 2$ refers to flame surface wrinkling ratio Ξ which is defined as the ratio of the turbulent flame surface area to the laminar flame surface area. Note that, if $D = 2$ is assumed, the flame surface wrinkling ratio converges to one ($\Xi = 1$), meaning that the flame is laminar, and no surface area enhancement is observed. To use the Eq. 2.21 in the premixed combustion modelling studies, Gouldin et al. [48] accounts for the probability of the presence of the cubic volume inside a turbulent flame brush thickness and re-writes the expression as follows:

$$\Sigma = \left(\frac{L_o}{L_i}\right)^{D-2} \frac{\overline{c}(1 - \overline{c})}{\delta_t} \tag{2.22}$$

The Eq. 2.22 is obtained by multiplying the Eq. 2.21 with $\bar{c}(1 - \bar{c})L_o/\delta_t$, where $\bar{c}$ is the Reynolds averaged progress variable, $\bar{c}(1-\bar{c})L_o$ stands for the probability of finding the flamelet along a segment of the flamelet normal which is of length L_o, and the division by the turbulent flame brush thickness δ_t is done for the normalization of the probability density function [48].

Apart from the derivation above, Bray et al. [49] proposed an empirical relation for the flame surface density Σ, based upon a square wave signal measured from the one-point statistics of a turbulent flame as follows:

$$\Sigma = \frac{g}{\sigma_y} \frac{\bar{c}(1 - \bar{c})}{L_y} \tag{2.23}$$

where $g \approx 1$ and $\sigma_y \approx 0.5$ are the empirical coefficients. L_y is defined as the integral length scale of the flame surface wrinkling, which controls the flame surface density Σ, and is expressed as follows [49]:

$$L_y = C_L l_{int} \left(\frac{S_{L0}}{u'} \right)^n \tag{2.24}$$

where $C_L \approx 1$ and $n \approx 1$ are the empirical coefficient and exponent, respectively, l_{int} is the turbulent integral length scale, u' is the turbulent fluctuation velocity and S_{L0} is the laminar flame speed.

2.3. AVERAGED/FILTERED GOVERNING EQUATIONS

In RANS simulations of variable density flows, Favre averaging (mass-weighted Reynolds averaging) is preferred over the Reynolds decomposition:

$$\tilde{f} = \frac{\overline{\rho f}}{\overline{\rho}} \tag{2.25}$$

In constant density LES simulations, the quantities are filtered in the physical space by taking the weighted average over a given volume which is defined as follows [13]:

$$\overline{f}(x) = \int f(x') F(x - x') dx' \tag{2.26}$$

where F is the LES filter:

$$F(x) = F(x_1, x_2, x_3) = \begin{cases} 1/\Delta_{LES}^3 & \text{if} \quad |x_i| \leq \Delta_{LES}/2, \ i = 1, 2, 3 \\ 0 & \text{otherwise} \end{cases} \tag{2.27}$$

In Eq. 2.27, $\Delta_{LES} = V^{1/3}$ is the LES filter length, where V is the volume of the mesh cell. For variable density flows, Favre (mass-weighted) filtering operation is defined as follows [13]:

$$\overline{\rho}\tilde{f}(x) = \int \rho f(x') F(x - x') dx' \tag{2.28}$$

After substitution of Favre averaged/filtered quantities into flow governing equations, a similar set of equations for RANS and LES can be obtained as follows [15]:

Continuity equation:

$$\frac{\partial \overline{\rho}}{\partial t} + \frac{\partial}{\partial x_i}\left(\overline{\rho}\tilde{u}_i\right) = 0 \tag{2.29}$$

Momentum equation:

$$\frac{\partial}{\partial t}\left(\overline{\rho}\tilde{u}_i\right) + \frac{\partial}{\partial x_i}\left(\overline{\rho}\tilde{u}_i\tilde{u}_j\right) + \frac{\partial \overline{p}}{\partial x_j} = \frac{\partial}{\partial x_i}\left(\overline{\tau}_{ij} + URS\right) \tag{2.30}$$

Total enthalpy equation, $h_t = h_s + h_c + K.E. = \int_{T_u}^{T_b} C_p\, dT + \sum_{k=1}^{N} \Delta h_{f,k}^o Y_k + \frac{1}{2}u_i u_i$:

$$\frac{\partial}{\partial t}\left(\overline{\rho}\tilde{h}_t\right) + \frac{\partial}{\partial x_i}\left(\overline{\rho}\tilde{u}_i\tilde{h}_t\right) = \frac{\partial \overline{p}}{\partial t} + \frac{\partial}{\partial x_j}\left(\overline{u_i\tau_{ij}}\right) + \frac{\partial}{\partial x_i}\left[\overline{\lambda}\frac{\partial \tilde{T}}{\partial x_i} - UEF\right] \tag{2.31}$$

Species transport equations for N species ($k = 1, ..., N$):

$$\frac{\partial}{\partial t}\left(\overline{\rho}\tilde{Y}_k\right) + \frac{\partial}{\partial x_i}\left(\overline{\rho}\tilde{u}_i\tilde{Y}_k\right) = \frac{\partial}{\partial x_i}\left[\overline{\rho}\overline{D}_k\frac{\partial \tilde{Y}_k}{\partial x_i} - USF\right] + \overline{\dot{\omega}}_k \tag{2.32}$$

$\overline{\tau_{ij}}$ term in the momentum (Eq. 2.30) and in the total enthalpy (Eq. 2.31) equations is the averaged/filtered viscous stress tensor which is evaluated as below.

$$\overline{\tau}_{ij} = -\frac{2}{3}\overline{\mu}\frac{\partial \tilde{u}_k}{\partial x_k}\delta_{ij} + \overline{\mu}\left(\frac{\partial \tilde{u}_i}{\partial x_j} + \frac{\partial \tilde{u}_j}{\partial x_i}\right) \tag{2.33}$$

URS (in Eq. 2.30) is the unclosed/unresolved Reynolds stress term and needs to be modelled with a proper turbulence or sub-grid-scale model. Energy equation (Eq. 2.31) is given in total enthalpy form which is the sum of sensible enthalpy h_s, chemical enthalpy h_c and kinetic energy $K.E.$. In this equation, the term with $\overline{u_{ij}\tau_{ij}}$ refers to the heating due to viscous dissipation and is generally neglected in subsonic flows as is done in this study too. UEF (in Eq. 2.31) and USF (in Eq. 2.32) refer to the unclosed/unresolved enthalpy and species fluxes, respectively, and are modelled following the gradient assumption [15]:

$$UEF = -\frac{\overline{C}_p\mu_t}{Pr_t}\frac{\partial \tilde{T}}{\partial x_i} \tag{2.34}$$

$$USF = -\frac{\mu_t}{Sc_{t,k}}\frac{\partial \tilde{Y}_k}{\partial x_i} \tag{2.35}$$

where $Sc_{t,k}$ is the turbulent Schmidt number of the k'th specie and Pr_t is the turbulent Prandtl number. μ_t is the turbulent/sub-grid-scale viscosity whose calculation depends on the turbulence /sub-grid-scale model chosen for the URS and $\overline{\dot{\omega}}_k$ (in Eq. 2.32) is the mass reaction rate of the k'th specie.

In the case of a thin premixed flame front, assuming a simple one-step irreversible chemical scheme, the flame can be described by a progress variable c, where $c = 0$ refers to unburnt and $c = 1$ refers to burnt gases. For such conditions, the progress variable is defined based on reduced mass fractions [15].

$$c = \frac{Y_f - Y_{f,u}}{Y_{f,b} - Y_{f,u}} \tag{2.36}$$

where Y_f, $Y_{f,u}$ and $Y_{f,b}$ are the local, unburnt gas and burnt gas fuel mass fractions, respectively. Under the assumptions of adiabatic combustion at constant pressure with unity Lewis number ($Le = 1$ for all the species), the species transport equations (Eq. 2.32) can be reduced to a single transport equation for the progress variable c, whose Favre averaged/filtered form ($\tilde{c}$) is given as below [13]:

$$\frac{\partial}{\partial t}\left(\overline{\rho}\tilde{c}\right) + \frac{\partial}{\partial x_i}\left(\overline{\rho}\tilde{u}_i\tilde{c}\right) = \frac{\partial}{\partial x_i}\left(\overline{\rho}D_t\frac{\partial \tilde{c}}{\partial x_i}\right) + \overline{\dot{\omega}} \tag{2.37}$$

where D_t is the turbulence diffusivity which is defined as follows:

$$D_t = \frac{\nu_t}{Sc_t} \tag{2.38}$$

In Eq. 2.38, $\nu_t = \mu_t/\overline{\rho}$ is the turbulent kinematic viscosity and Sc_t is the turbulent Schmidt number. In this study, $Sc_t = Pr_t = 0.7$ is assumed. The term $\overline{\dot{\omega}}$ in Eq. 2.37 is the reaction rate source term (reaction rate closure) responsible for the turbulence-chemistry interaction and needs to be modelled. Some of the methods to model this term are explained in Section 2.5., and the proposed model is described in Chapter 3.

2.4. MODELLING TURBULENCE

This section explains modelling of the unclosed/unresolved Reynolds stress tensor (URS term in Eq. 2.30) in RANS, SAS and LES contexts. The URS term, born due to averaging/filtering operation, is not closed/resolved in RANS/LES and needs modelling. Figure 2.6 a) and b) illustrate the averaged/filtered parts of the velocity compared to direct numerical simulation (DNS). The URS term is defined for RANS and LES as follows:

$$URS_{RANS} = -\overline{\rho}\widetilde{u_i''u_j''}, \quad URS_{LES} = -\overline{\rho}\left(\widetilde{u_iu_j} - \tilde{u}_i\tilde{u}_j\right) \tag{2.39}$$
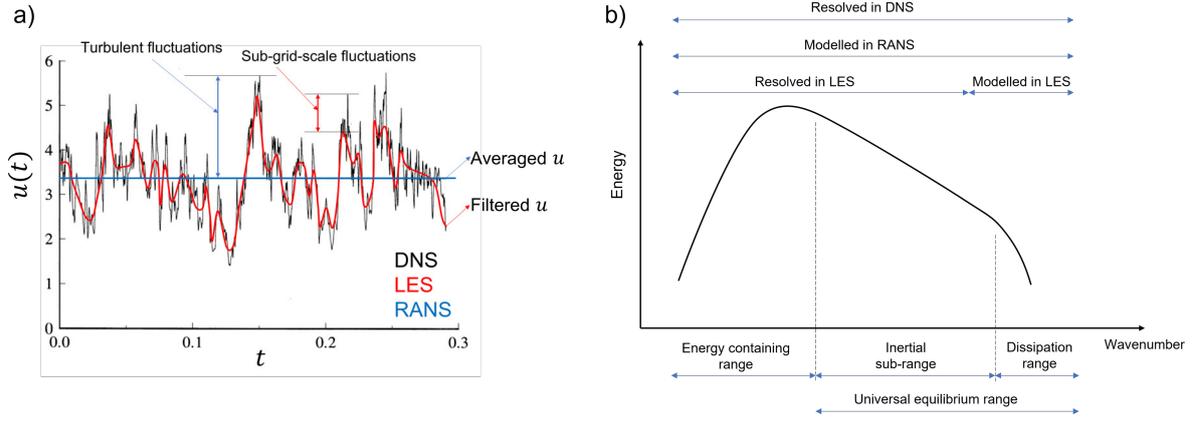
Figure 2.6: a) DNS, LES and RANS difference on a sampled velocity signal, b) DNS, LES and RANS scale resolution and modelling differences. Figure a) is modified from [45].

2.4.1. Reynolds averaged Navier Stokes (RANS)

In RANS approach, unclosed Reynolds stress tensor URS_{RANS} can be modelled either based on eddy viscosity models with Boussinesq approximation or solving transport equations for the Reynolds stresses.

Eddy viscosity turbulence models

Boussinesq hypothesis assumes that the turbulence is isotropic, and relates the Reynolds stresses to the mean velocity gradients through the turbulent viscosity μ_t. The two equations model families $k - \epsilon$ and $k - \omega$ models use this approach to model the unclosed Reynolds stress tensor URS_{RANS} [50].

$$-\overline{\rho} \widetilde{u_i'' u_j''} = \mu_t \left(\frac{\partial \tilde{u}_i}{\partial x_j} + \frac{\partial \tilde{u}_j}{\partial x_i} \right) - \frac{2}{3} \left(\overline{\rho} \tilde{k} + \mu_t \frac{\partial \tilde{u}_k}{\partial x_k} \right) \delta_{ij} \tag{2.40}$$

The turbulent viscosity μ_t is computed for the $k - \epsilon$ turbulence model as follows:

$$\mu_t = \overline{\rho} C_\mu \frac{\tilde{k}^2}{\tilde{\epsilon}} \tag{2.41}$$

and for the $k - \omega$ turbulence model as follows:

$$\mu_t = \frac{\overline{\rho} \tilde{k}}{\tilde{\omega}} \tag{2.42}$$

In Eq. 2.41, $C_\mu = 0.09$ is the model coefficient of the $k - \epsilon$ model. According to the version selected (i.e. realizable $k - \epsilon$ model, $k - \omega$ SST model, etc.), turbulent kinetic energy and turbulent dissipation rate or specific dissipation rate are solved from their transport equations.

Reynolds stress turbulence model (RSM)

Reynolds stress model (RSM) solves a transport equation for each component of the Reynolds stress tensor $URS_{RANS} = -\overline{\rho}\widetilde{u_i'' u_j''}$, and additionally solves a transport equation for the turbulence dissipation rate ϵ or the specific dissipation rate ω, depending on the version selected. Since the $-\overline{\rho}\widetilde{u_i'' u_j''}$ is a symmetric tensor, in total seven transport equations (six equations for the Reynolds stresses and one equation for the dissipation rate) are solved for a three-dimensional simulation. In this study, RANS calculations are carried out with an ϵ based linear pressure-strain RSM model whose transport equations for Reynolds stresses are given as follows [50]:

$$\frac{\partial}{\partial t}\left(\overline{\rho}\widetilde{u_i'' u_j''}\right) + \frac{\partial}{\partial x_k}\left(\overline{\rho}\tilde{u}_k \widetilde{u_i'' u_j''}\right) = \frac{\partial}{\partial x_k}\left[\left(\overline{\mu} + \frac{\mu_t}{\sigma_k}\right)\frac{\partial}{\partial x_k}\left(\widetilde{u_i'' u_j''}\right)\right] + P_{ij} + \phi_{ij} - \epsilon_{ij} \quad (2.43)$$

where P_{ij}, ϕ_{ij} and ϵ_{ij} are defined as follows:

$$P_{ij} = -\overline{\rho}\left[\widetilde{u_i'' u_k''}\frac{\partial \tilde{u}_j}{\partial x_k} + \widetilde{u_j'' u_k''}\frac{\partial \tilde{u}_i}{\partial x_k}\right] \quad (2.44)$$

$$\phi_{ij} = -C_1\overline{\rho}\frac{\tilde{\epsilon}}{\tilde{k}}\left[\widetilde{u_i'' u_j''} - \frac{2}{3}\delta_{ij}\tilde{k}\right] - C_2\left[P_{ij} - \frac{1}{3}\delta_{ij}P_{kk}\right] \quad (2.45)$$

$$\epsilon_{ij} = \frac{2}{3}\delta_{ij}\overline{\rho}\tilde{\epsilon} \quad (2.46)$$

and the coefficients are given as below.

$$\sigma_k = 0.82, \quad C_1 = 1.8, \quad C_2 = 0.6 \quad (2.47)$$

The transport equation for the turbulent dissipation rate is given as follows:

$$\frac{\partial}{\partial t}\left(\overline{\rho}\tilde{\epsilon}\right) + \frac{\partial}{\partial x_i}\left(\overline{\rho}\tilde{\epsilon}\tilde{u}_i\right) = \frac{\partial}{\partial x_j}\left[\left(\overline{\mu} + \frac{\mu_t}{\sigma_\epsilon}\right)\frac{\partial \tilde{\epsilon}}{\partial x_j}\right] + C_{1\epsilon}\frac{1}{2}P_{ii}\frac{\tilde{\epsilon}}{\tilde{k}} - C_{2\epsilon}\overline{\rho}\frac{\tilde{\epsilon}^2}{\tilde{k}} \quad (2.48)$$

where the coefficients are given as below.

$$\sigma_\epsilon = 1.0, \quad C_{1\epsilon} = 1.44, \quad C_{2\epsilon} = 1.92 \quad (2.49)$$

The turbulent viscosity μ_t is calculated from Eq. 2.41, and the turbulent kinetic energy is computed from the trace of the Reynolds stress tensor.

$$\tilde{k} = \frac{1}{2}\widetilde{u_i'' u_i''} \quad (2.50)$$

2.4.2. Scale adaptive simulation (SAS)

Scale adaptive simulation (SAS) introduced by Menter and Egorov [51, 52], is an improved unsteady RANS formulation, which allows resolution in the turbulent spectrum in unstable flow

conditions. In unsteady RANS (URANS) calculations, only the large-scale structures of turbulence can be resolved. The SAS overcomes this limitation by introducing a von Karman length scale dependent source term to the specific dissipation rate ω equation, which allows dynamic adjustment for the resolved scales and results in a LES-like behaviour in the unsteady regions of the flow field (see Figure 2.7). At the same time standard RANS behaviour is preserved in the stable regions [50].
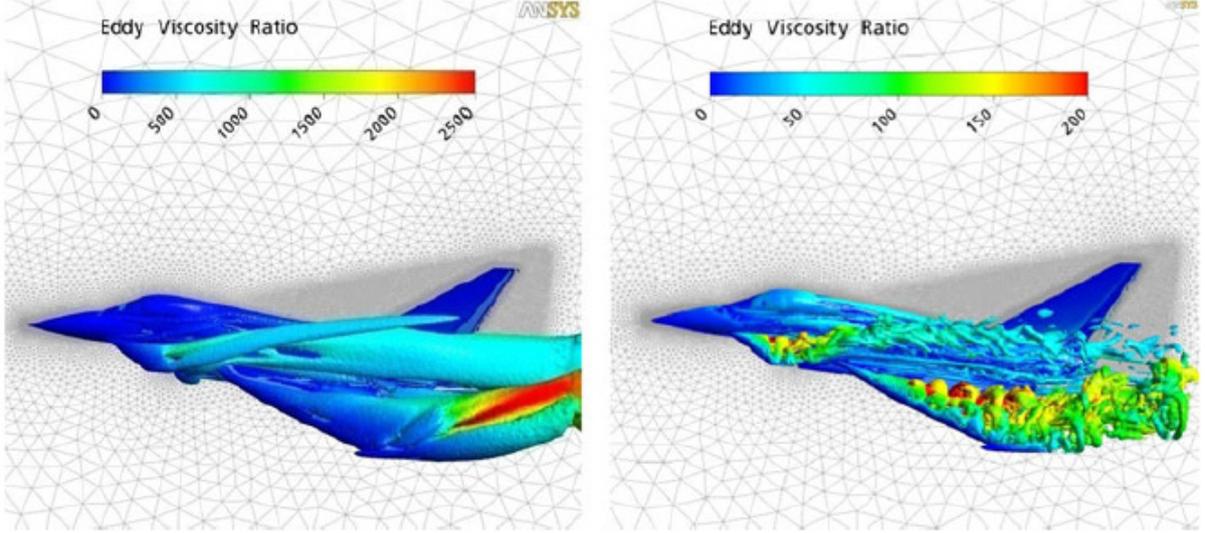
Figure 2.7: SST-URANS vs SST-SAS comparison in the unsteady region of the flow. Figure is taken from [52].

The SAS approach, initially developed for $k - \omega\ SST$ turbulence model [51, 52], can be used with any version of ω based models including ω based RSM turbulence model, which is selected in this study. In ω based RSM-SAS model, the Reynolds stress transport equations are in the same form of Eq. 2.43, with a difference in modelling of the ϕ_{ij} and ϵ_{ij} terms.

The ϕ_{ij} term in Eq. 2.43 is modelled in SAS as follows [50]:

$$
\begin{aligned}
\phi_{ij} = & -C_1 \overline{\rho} \beta^*_{RSM} \tilde{\omega} \left[\widetilde{u_i'' u_j''} - \frac{2}{3} \delta_{ij} \tilde{k} \right] - \hat{\alpha}_0 \left[P_{ij} - \frac{1}{3} P_{kk} \delta_{ij} \right] \\
& - \hat{\beta}_0 \left[D_{ij} - \frac{1}{3} P_{kk} \delta_{ij} \right] - \tilde{k} \hat{\gamma}_0 \left[S_{ij} - \frac{1}{3} S_{kk} \delta_{ij} \right]
\end{aligned}
\tag{2.51}
$$

where D_{ij}, S_{ij} and the coefficients are defined as:

$$
D_{ij} = -\overline{\rho} \left[\widetilde{u_i'' u_k''} \frac{\partial \tilde{u}_k}{\partial x_j} + \widetilde{u_j'' u_k''} \frac{\partial \tilde{u}_k}{\partial x_i} \right]
\tag{2.52}
$$

$$
S_{ij} = \frac{1}{2} \left[\frac{\partial \tilde{u}_j}{\partial x_i} + \frac{\partial \tilde{u}_i}{\partial x_j} \right]
\tag{2.53}
$$

$$C_1 = 1.8, \quad C_2 = 0.52, \quad \hat{\alpha}_0 = \frac{8 + C_2}{11}, \quad \hat{\beta}_0 = \frac{8C_2 - 2}{11}, \quad \hat{\gamma}_0 = \frac{60C_2 - 4}{55} \tag{2.54}$$

and the β_{RSM}^* is defined as below.

$$\beta_{RSM}^* = \beta^* f_\beta^*,$$

$$\beta^* = 0.09, \quad f_\beta^* = \begin{cases} 1, & \text{if } \chi_k \leq 0 \\ \frac{1 + 640\chi_k^2}{1 + 400\chi_k^2}, & \text{otherwise} \end{cases}, \quad \chi_k \equiv \frac{1}{\tilde{\omega}^3} \frac{\partial \tilde{k}}{\partial x_j} \frac{\partial \tilde{\omega}}{\partial x_j} \tag{2.55}$$

The ϵ_{ij} term in Eq. 2.43 is modelled in SAS as follows.

$$\epsilon_{ij} = \frac{2}{3} \delta_{ij} \overline{\rho} \beta_{RSM}^* \tilde{k} \tilde{\omega} \tag{2.56}$$

The turbulent specific dissipation rate ω transport equation for SAS is given as below:

$$\frac{\partial}{\partial t} (\overline{\rho} \tilde{\omega}) + \frac{\partial}{\partial x_i} (\overline{\rho} \tilde{\omega} \tilde{u}_i) = \frac{\partial}{\partial x_j} \left[\left(\overline{\mu} + \frac{\mu_t}{\sigma_\omega} \right) \frac{\partial \tilde{\omega}}{\partial x_j} \right] + \frac{\tilde{\omega}}{\tilde{k}} \mu_t S^2 - \overline{\rho} \beta f_\beta \tilde{\omega}^2 + Q_{SAS} \tag{2.57}$$

where $\sigma_\omega = 2.0$ and $\beta = 0.072$ are the model coefficients, and S is the modulus of the mean strain rate tensor S_{ij} which is calculated as follows:

$$S \equiv \sqrt{2 S_{ij} S_{ij}} \tag{2.58}$$

and the f_β term is calculated as below.

$$f_\beta = \frac{1 + 70\chi_\omega}{1 + 80\chi_\omega}, \quad \chi_\omega = \left| \frac{\Omega_{ij} \Omega_{ij} S_{ki}}{(\beta^* \tilde{\omega})^3} \right|, \quad \Omega_{ij} = \frac{1}{2} \left(\frac{\partial \tilde{u}_i}{\partial x_j} - \frac{\partial \tilde{u}_j}{\partial x_i} \right) \tag{2.59}$$

Q_{SAS} term in Eq. 2.57 is the additional source term of the scale adaptive simulation, which is given as follows:

$$Q_{SAS} = max \left[\overline{\rho} \eta_2 \kappa S^2 \left(\frac{l_t}{L_{vK}} \right)^2 - C \frac{2 \overline{\rho} \tilde{k}}{\sigma_\phi} max \left(\frac{1}{\tilde{\omega}^2} \frac{\partial \tilde{\omega}}{\partial x_j} \frac{\partial \tilde{\omega}}{\partial x_j}, \frac{1}{\tilde{k}^2} \frac{\partial \tilde{k}}{\partial x_j} \frac{\partial \tilde{k}}{\partial x_j} \right), 0 \right] \tag{2.60}$$

where η_2, C, σ_ϕ are the coefficients given as below:

$$\eta_2 = 3.51, \quad C = 2, \quad \sigma_\phi = \frac{2}{3} \tag{2.61}$$

and l_t and L_{vK} are the turbulent length scale and the von Karman length scale, respectively.

$$l_t = \frac{\sqrt{\tilde{k}}}{C_\mu^{0.25} \tilde{\omega}} \tag{2.62}$$

$$L_{vK} = \kappa \left| \frac{S}{U''} \right| \tag{2.63}$$

In the Eq. 2.62 and 2.63, $C_\mu = 0.09$ is the model coefficient as in the $k - \epsilon$ turbulence model, and $\kappa = 0.41$ is the von Karman constant. S is the modulus of mean strain rate tensor calculated following Eq. 2.58 and the U'' term is defined as follows.

$$U'' = \sqrt{\frac{\partial^2 \tilde{u}_i}{\partial x_k^2} \frac{\partial^2 \tilde{u}_i}{\partial x_j^2}} \tag{2.64}$$

Finally, the turbulent viscosity μ_t is calculated from the Eq. 2.42, and the turbulent kinetic energy k is calculated from the Eq. 2.50.

2.4.3. Large eddy simulation (LES)

In LES, unresolved Reynolds stress tensor URS_{LES}, which is born due to filtering operation, is unknown and needs to be modelled. Sub-grid-scale (SGS) models use Boussinesq approximation to model this tensor similar to RANS eddy viscosity-based turbulence models. In this study, the dynamic kinetic energy SGS model, which solves a transport equation for the SGS kinetic energy k_{SGS}, is used to model the turbulent viscosity μ_t and the unresolved Reynolds stress tensor.

In this approach, the turbulent viscosity μ_t, the unresolved Reynolds stress tensor URS_{LES} and the transport equation for the SGS kinetic energy are given as follows [50]:

$$\mu_t = C_k \overline{\rho} \tilde{k}_{SGS}^{0.5} \Delta_{LES} \tag{2.65}$$

$$URS_{LES} = -\overline{\rho} \left(\widetilde{u_i u_j} - \tilde{u}_i \tilde{u}_j \right) = \mu_t \left(\frac{\partial \tilde{u}_i}{\partial x_j} + \frac{\partial \tilde{u}_j}{\partial x_i} \right) + \frac{2}{3} \overline{\rho} \tilde{k}_{SGS} \delta_{ij} \tag{2.66}$$

$$\overline{\rho} \frac{\partial \tilde{k}_{SGS}}{\partial t} + \overline{\rho} \frac{\partial}{\partial x_j} \left(\tilde{u}_j \tilde{k}_{SGS} \right) = URS_{LES} \frac{\partial \tilde{u}_i}{\partial x_j} - C_\epsilon \overline{\rho} \frac{\tilde{k}_{SGS}^{1.5}}{\Delta_{LES}} + \frac{\partial}{\partial x_j} \left(\mu_t \frac{\partial \tilde{k}_{SGS}}{\partial x_j} \right) \tag{2.67}$$

In Eq. 2.65 - 2.67, $\Delta_{LES} = V^{1/3}$ refers to the LES filter length with V is the volume of the mesh cells. Noting that, Eq. 2.65 - 2.67 are dependent on each other and the model coefficients C_k and C_ϵ are calculated dynamically as explained in [53].

2.5. MODELLING TURBULENT COMBUSTION

This section summarizes some of the modelling approaches for closing the reaction rate source term $\overline{\dot{\omega}}$ in Eq. 2.37. Amongst many other modelling approaches in the literature, only those which are used in this study, are summarized here, and the proposed modelling approach is explained in Chapter 3.

2.5.1. Turbulent flame speed based models

Turbulent flame speed models close the Favre averaged progress variable $\tilde{c}$ equation as follows [31]:

$$\overline{\dot{\omega}} = \rho_u S_t |\nabla \tilde{c}| \tag{2.68}$$

where ρ_u is the unburnt mixture density, S_t is the turbulent flame speed, and the term $|\nabla \tilde{c}|$ is calculated as follows:

$$|\nabla \tilde{c}| \equiv \left[\sum_{k=1}^{3} \left(\frac{\partial \tilde{c}}{\partial x_k} \right)^2 \right]^{0.5} \tag{2.69}$$

Turbulent flame closure (TFC) model

The Eq. 2.70 for S_t was proposed by Zimont et al. [31, 54, 55] together with Eq. 2.68 to close the progress variable $\tilde{c}$ equation, resulting in turbulent flame closure (TFC) model. The model was initially developed for RANS, then it was extended to LES [42, 56]. Here the original RANS version is explained.

$$S_t = A u'^{0.75} S_{L0}^{0.5} \alpha_u^{-0.25} l_t^{0.25} \tag{2.70}$$

In Eq. 2.70, A, u', S_{L0}, α_u and l_t refer to the model coefficient $A = 0.52$, turbulent velocity, unstretched adiabatic laminar flame speed, thermal diffusivity of the unburnt mixture and the turbulent length scale, respectively. The turbulent velocity and the turbulent length scale are given as follows:

$$u' = \sqrt{\frac{2}{3}\tilde{k}} \tag{2.71}$$

$$l_t = C_D \frac{u'^3}{\tilde{\epsilon}} \tag{2.72}$$

where $C_D = 0.37$ is given as a coefficient for the turbulent length scale.

Flame speed closure (FSC) model

Lipatnikov et al. [46] replaced the turbulence diffusivity D_t (in Eq. 2.37) and the turbulent flame speed S_t (Eq. 2.68) terms by their flame development time t_{fd} dependent forms $D_{t,t}$ and $S_{t,t}$, respectively, as follows:

$$D_{t,t} = D_t \left[1 - \exp\left(-\frac{t_{fd}}{\tau'} \right) \right], \quad S_{t,t} = S_t \left[1 + \frac{\tau'}{t_{fd}} \left[\exp\left(-\frac{t_{fd}}{\tau'} - 1 \right) \right] \right]^{0.5} \tag{2.73}$$

where the reaction rate source term becomes:

$$\overline{\dot{\omega}} = \rho_u S_t \left[1 + \frac{\tau'}{t_{fd}} \left[\exp\left(-\frac{t_{fd}}{\tau'} - 1\right)\right]\right]^{0.5} |\Delta\tilde{c}| \tag{2.74}$$

With these replacements, he aimed at reproducing the turbulent flame brush thickness development better, and entitled this approach as the flame speed closure (FSC) model. In this approach, the flame development time t_{fd} and the fully developed flame time scale τ' are defined as follows:

$$t_{fd} = \frac{x_c - x_{fh}}{u_{dump}}, \quad \tau' = \frac{D_t}{u'^2} \tag{2.75}$$

where x_c is the axial coordinate of the cell of interest, x_{fh} is the axial coordinate of the flame holder (flame attachment point to the solid boundary), and u_{dump} is the mean axial velocity at the dump plane.

Extended turbulent flame closure (ExtTFC) model

Tay-Wo-Chong et al. [6] extended the TFC closure by replacing the unstretched adiabatic laminar flame speed S_{L0} with the stretched and non-adiabatic laminar consumption speed $S_c(\kappa, \beta)$. In the extended TFC (ExtTFC) model, Eq. 2.68 remains the same but the turbulent flame speed is updated as below:

$$S_t = 0.52 u'^{0.75} S_c(\kappa, \beta)^{0.5} \alpha_u^{-0.25} l_t^{0.25} \tag{2.76}$$

where the $S_c(\kappa, \beta)$ is tabulated from a fresh-to-burnt counter flow flame flamelet configuration in one-dimensional chemistry solvers (i.e. *CANTERA*) at different levels of stretch κ and heat loss β with detailed chemistry mechanism. Further details of the $S_c(\kappa, \beta)$ tabulation will be explained in Chapter 3.

Algebraic flame surface wrinkling (AFSW) model

Dinkelacker and Muppala [36, 40] proposed an effective Lewis number (Le^*) dependent turbulent flame speed S_t expression for the TFC closure (Eq. 2.68) for simulations of fuel mixtures with H_2 content and entitled the model as the algebraic flame surface wrinkling (AFSW) model.

$$S_t = S_{L0} + \frac{0.46}{\exp\left(Le^* - 1\right)} u'^{0.55} S_{L0}^{0.7} \nu_u^{-0.25} l_t^{0.25} \left(\frac{P}{1 \text{ atm}}\right)^{0.2} \tag{2.77}$$

In Eq. 2.77, ν_u is the kinematic viscosity of the unburnt mixture, P is the operating pressure, and the turbulent length scale l_t is calculated as follows:

$$l_t = C_\mu^{0.75} \frac{\tilde{k}^{1.5}}{\epsilon} \tag{2.78}$$

where $C_\mu = 0.09$ is the coefficient of $k - \epsilon$ turbulence model. The hydrogen enrichment effect (increased reactivity due to preferential diffusion of H_2) on the turbulent flame speed is taken into account by updating the model coefficient by means of an effective Lewis number Le^* which is defined as below [36]:

$$Le^* = \frac{\alpha_{mix}}{X_{\mathrm{CH_4}}D_{\mathrm{CH_4}} + X_{\mathrm{H_2}}D_{\mathrm{H_2}}} \tag{2.79}$$

where α_{mix} is the mixture thermal diffusivity, X is the molar fraction of the specie in the fuel mixture and D is the binary molecular diffusion coefficient of the specie with respect to inert $\mathrm{N_2}$ specie.

2.5.2. Kolmogorov-Petrovskii-Piskunov (KPP) theorem

Kolmogorov-Petrovskii-Piskunov (KPP) theorem is a theoretical tool that can provide a relation between the turbulent flame speed S_t and the reaction rate source term $\bar{\bar{\omega}}$ under some assumptions, such as frozen turbulence [13]. Assuming a relation between $\bar{\bar{\omega}}$ and S_t as follows:

$$\bar{\bar{\omega}} = \rho_u F(S_t)\tilde{c}(1 - \tilde{c}) \tag{2.80}$$

where $F(S_t)$ is the unknown function depending on S_t, a balance equation for statistically one-dimensional steady propagating turbulent flame is given as follows [13]:

$$\rho_u S_t \frac{\partial \tilde{c}}{\partial x} = \rho_u \frac{\nu_t}{Sc_t}\frac{\partial^2 \tilde{c}}{\partial x^2} + \rho_u F(S_t)\tilde{c}(1 - \tilde{c}) \tag{2.81}$$

Neglecting the second order terms, the equation becomes [13]:

$$S_t \frac{\partial \tilde{c}}{\partial x} = \frac{\nu_t}{Sc_t}\frac{\partial^2 \tilde{c}}{\partial x^2} + F(S_t)\tilde{c} \tag{2.82}$$

which has a solution when the discriminant $\Delta \geq 0$ [13].

$$\Delta = S_t^2 - 4\frac{\nu_t}{Sc_t}F(S_t) \geq 0, \quad \frac{S_t^2 Sc_t}{4\nu_t} \geq F(S_t) \tag{2.83}$$

Then a proportionality between the reaction rate source term $\bar{\bar{\omega}}$ and the turbulent flame speed S_t can be derived as follows:

$$\bar{\bar{\omega}} \propto \rho_u \frac{S_t^2 Sc_t}{4\nu_t}\tilde{c}(1 - \tilde{c}) \tag{2.84}$$

where $\nu_t = \frac{\mu_t}{\bar{\rho}}$ is the turbulent kinematic viscosity can be calculated from Eq. 2.41, and $Sc_t = 0.7$ is the turbulent Schmidt number. Using Eq. 2.41, 2.71 and 2.78, an expression for the reaction rate source term $\bar{\bar{\omega}}$, which is in the same form of Schmid et al.'s model [32], can be proposed as follows:

$$\bar{\bar{\omega}} = C_{KPP}\rho_u \frac{S_t^2}{u'^2}\frac{\tilde{\epsilon}}{\tilde{k}}\tilde{c}(1 - \tilde{c}) \tag{2.85}$$

where C_{KPP} is the model coefficient needs to be calibrated.

PROPOSED REACTION RATE CLOSURE

This chapter describes the proposed combustion modelling closure for turbulent premixed CH_4/H_2/air flames. The chapter starts with describing the stretch and heat loss modelling, followed by a turbulent flame speed derivation and its calibration, and is concluded by describing the proposed algebraic reaction rate closure.

3.1. STRETCH AND HEAT LOSS MODELLING

Stretch and heat loss modelling is composed of two steps. In the first step, laminar consumption speed S_c look-up tables are generated and in the second step, stretch κ and heat loss parameter β are modelled in the computational domain. These steps are explained below.

3.1.1. Chemistry tabulation

As the first step, the chemistry tabulation is done by calculating the laminar consumption speed S_c at different levels of stretch κ and heat loss β [6–8] in a fresh-to-burnt counter-flow flame configuration (see Figure 3.1 a)) in *CANTERA*. These tabulated S_c values are then used as look-up tables by the CFD solver.
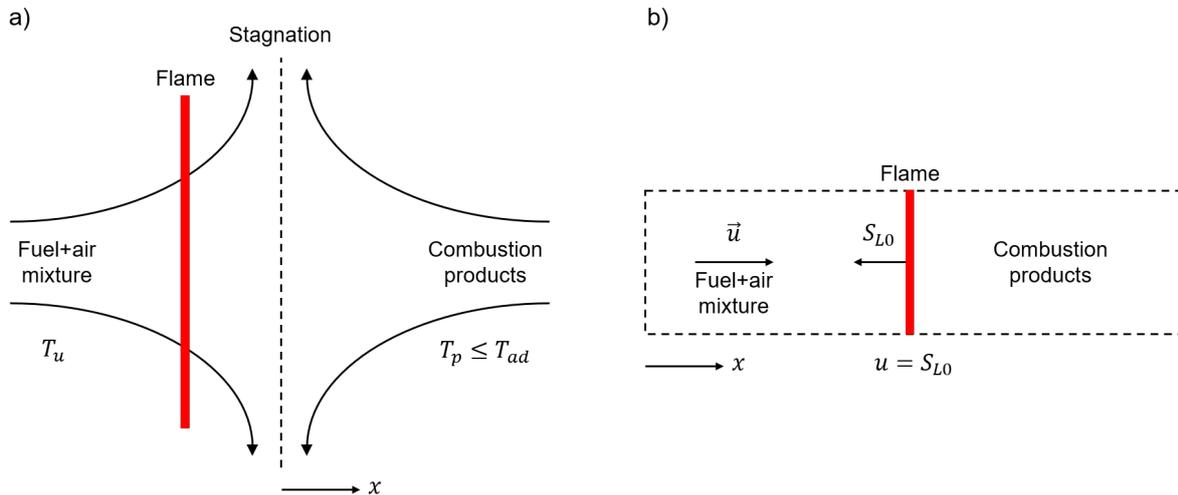
Figure 3.1: a) Fresh-to-burnt counter-flow flame and b) free flame configurations in *CANTERA*.

In order to simulate different levels of heat loss from the flame, the temperature of the unburnt mixture T_u is kept constant, while the temperature of the products T_p is gradually decreased starting from the adiabatic flame temperature T_{ad}. The β heat loss parameter (where $\beta = 1$ refers to the adiabatic case) is defined as below.

$$\beta = \frac{T_p - T_u}{T_{ad} - T_u} \tag{3.1}$$

Flame stretch is calculated from the maximum velocity gradient at the unburnt side of the opposed jets in the counter-flow flame configuration.

$$\kappa = \max \left| -\frac{\partial u}{\partial x} \right| \tag{3.2}$$

The flow velocities of the reactant and the product jets are increased gradually until either the flame extinction occurs or a maximum prescribed level of strain is reached. The momentum of reactants and products is kept always equal to maintain the stagnation plane position approximately constant. The non-adiabatic stretched consumption speed S_c is calculated as follows:

$$S_c = \frac{1}{\rho_u \Delta H_c^o Y_f} \int_{-\infty}^{\infty} \dot{q} \, dx \tag{3.3}$$

where ΔH_c^o is the lower heating value of the combustion, Y_f is the mass fraction of the fuel in the reactants mixture (mixture fraction), and $\dot{q}$ is the total heat release rate per unit volume.

For zero stretch, the laminar flame consumption speed S_c is assumed to be equal to the unstretched adiabatic laminar flame speed S_{L0} and is calculated from the free flame configuration in *CANTERA* (see Figure 3.1 b)) following Eq. 3.3, which is equivalent to $S_{L0} = S_c(\kappa = 0, \beta = 1)$.

3.1.2. Stretch and heat loss modelling in CFD

Flame stretch is modelled in the CFD simulations as the sum of contributions from the mean/resolved flow and turbulent/sub-grid-scale fluctuations [20, 57, 58].

$$\kappa = \underbrace{(\delta_{ij} - n_i \tilde{n}_j) \frac{\partial \tilde{u}_i}{\partial x_j}}_{\kappa_{mean/resolved}} + \underbrace{\Gamma_K \left(\frac{A}{S_{L0}}, \frac{B}{\delta_{L0}} \right) C \left[\frac{1}{Le} \left(1.76 + \tanh \left(Le - 2 \right) \right) \right]}_{\kappa_{turbulent/SGS}} \tag{3.4}$$

In Eq. 3.4, δ_{ij} is the Kronecker delta, $n_i \tilde{n}_j$ is the orientation factors, Γ_K is the ITNFS (Intermittent turbulence net flame stretch) efficiency function [13, 59], S_{L0} and δ_{L0} are the unstretched adiabatic laminar flame speed and flame thickness, which are calculated following Eq. 3.3 and 1.3, respectively. The term in square brackets on the RHS was proposed in [60] to better fit the average turbulent flame stretch values computed from direct numerical simulations of CH_4/H_2/air and C_3H_8/H_2/air flames, where Le is calculated as $Le = X_{CH_4} \alpha_u / D_{CH_4} + X_{H_2} \alpha_u / D_{H_2}$. This term converges to zero when $Le = 1$, thus recovers the original ITNFS definition [13, 59] for CH_4/air flames.

$$\log_{10} \left(\Gamma_K \right) = -\frac{\exp(\text{-}s\text{-}0.4)}{s + 0.4} + \left(1 - \exp(-s - 0.4) \right) \left[\sigma_1 \left(\frac{A}{S_{L0}} \right) s - 0.11 \right] \tag{3.5}$$

$$s = \log_{10} \left(\frac{B}{\delta_{L0}} \right) \tag{3.6}$$

Table 3.1: RANS, SAS and LES evaluations of A, B and C terms.

	A	B	C
RANS/SAS	u'	$\frac{u'^3}{\tilde{\epsilon}}$	$\frac{\tilde{\epsilon}}{\tilde{k}}$
LES	u'_{SGS}	Δ_{LES}	$\frac{\sqrt{k_{SGS}}}{\Delta_{LES}}$

$$\sigma_1\left(\frac{A}{S_{L0}}\right) = \frac{2}{3}\left[1 - \frac{1}{2}\text{exp}\left[-\left(\frac{A}{S_{L0}}\right)^{1/3}\right]\right] \tag{3.7}$$

A, B and C terms are calculated as given in Table 3.1. For ω based turbulence models, turbulent dissipation rate is calculated from $\tilde{\epsilon} = C_\mu\tilde{\omega}\tilde{k}$ where $C_\mu = 0.09$.

Modelling of the orientation factors $\widetilde{n_i n_j}$ differs based on the selected turbulence model. For example, for the two equations eddy viscosity models, the mean/resolved stretch reduces to $\kappa_{mean} = \frac{2}{3}\frac{\partial \tilde{u}_i}{\partial x_j}$ due to isotropic turbulence assumption [6]. For the RSM-based RANS and SAS turbulence models, which are selected in this study, the orientation factors are modelled following [61] as follows:

$$\widetilde{n_i n_i} = \frac{\sum_{k\neq i}\widetilde{u_k''^2}}{4\tilde{k}}, \quad \widetilde{n_i n_{j\neq i}} = \frac{\widetilde{u_i'' u_j''}}{2\tilde{k}} \tag{3.8}$$

For scale-resolved simulations (SAS and LES), the orientation factors can be modelled from two different approaches, which are referred to as 's1' [8] and 's2' [62] in Table 3.2:

Table 3.2: Modelling the orientation factors for scale-resolved simulations (SAS/LES).

s1	s2
$\vec{n} = -\frac{\nabla\tilde{c}}{\lvert\nabla\tilde{c}\rvert}$	$\widetilde{n_i n_j} = \widetilde{m_i m_j} + \frac{1}{3}\gamma\delta_{ij}$ $\gamma = 1 - \vec{m}\cdot\vec{m}$ $\vec{m} = -\frac{\nabla\tilde{c}}{\lvert\nabla\tilde{c}\rvert}$

where n_i is defined as the component of the vector normal to the flame surface in the 's1' model, and m_i is defined in the same way in the 's2' model. As explained in Chapter 2, the SAS is an improved version of unsteady RANS formulation, allowing to model the orientation factors in the same way as RANS. On the other hand, its LES-like scale-resolving behavior allows modelling the orientation factors as in LES. In this thesis study, both RANS and LES formulations are tested to model the orientation factors in SAS simulations.

Heat loss parameter β definition does not depend on the turbulence model and is defined as follows:

$$\beta = 1 - \frac{h_u - \tilde{h}_t}{\tilde{c}Y_f\Delta H_c^o} \tag{3.9}$$

where h_u, $\tilde{h}_t$, $\tilde{c}$, Y_f and ΔH_c^o refer to the total unburnt adiabatic enthalpy, the local value of the total enthalpy (obtained from Eq. 2.31), the progress variable, fuel mass fraction in the premixed mixture (mixture fraction) and the lower heating value of combustion, respectively.

3.2. TURBULENT FLAME SPEED DERIVATION

In the context of this study, the following turbulent flame speed S_t expression for $CH_4/H_2/air$ flames is proposed [20] by combining Eqs. 2.76 and 2.77 and by calibrating it against the experimental measurements [63–66].

$$S_t = S_c + \frac{0.4}{\sqrt{Le^*}} u'^{0.8} S_c^{0.45} \alpha_u^{-0.25} l_t^{0.25} \tag{3.10}$$

The similarities and differences with respect to Eqs. 2.76 and 2.77 are listed as follows.

First, in Eq. 3.10, the effective Lewis number Le^* is included to model the effect of hydrogen molecular diffusion on S_t, mimicking the approach that led to the development of Eq. 2.77. However, here S_t is considered that it varies proportionally to $Le^{*-0.5}$ and not to $\exp(1 - Le^*)$. This different exponent was proposed in the recent study described in [65] where it was found that $Le^{*-0.5}$ was able to best fit turbulent flame speed experimental data of pure hydrogen, propane, and iso-octane flames. Furthermore, Le^* in Eq. 3.10 is calculated as in Eq. 2.77 but the transport properties, α_{mix}, D_{CH_4} and D_{H_2} are computed at the temperature corresponding to the location of maximum heat release rate in a one-dimensional unstretched laminar flame (see Figure 3.1 b)). This different evaluation method of Le^* was mentioned in [36], because the diffusivity of hydrogen in the reaction zone of the flame is considered more meaningful for the description of the interaction between flame molecular diffusion processes and turbulent eddies.

Second, the use of S_c instead of S_{L0} is retained from Eq. 2.76 to model stretch and heat loss effects. This is particularly important to reflect the quenching effects at the outer shear layer [6–8]. The exponents of u' and S_c are adjusted compared to Eq. 2.76 primarily to achieve a better fit with the turbulent flame speed experimental data shown in Figures 3.2 and 3.3. For the same reason, the model coefficient is changed to 0.4 compared to the original value of 0.52 also, to compensate for the fact that in Eq. 3.10 for the definition of turbulent length scale l_t, Eq. 2.78 is used instead of Eq. 2.72. Note that the original exponents in Zimont's expression (Eq. 2.70) were derived by means of theoretical arguments based on the dimensional analysis of the propagation of one-dimensional turbulent flame [54]. Here, the small adjustment is reasonable because in S_c there is already a built-in dependence on u' through the stretch factor κ which was not present in [54].

Third, compared to Eq. 2.76, in Eq. 3.10, the S_c term was added to S_t in order to recover the laminar flame propagation speed when $u' = 0$. In fact, for high hydrogen content, S_c can remarkably increase with stretch and become a significant contribution to turbulent flame propagation.

3.2.1. Calibration and validation of the proposed expression

The calibration and the validation of the Eq. 3.10 were done against the fan-stirred bomb experiments in the open literature [63–66]. In these experiments, the flame is propagating in isotropic turbulence with zero mean velocity, which results in $\kappa_{mean} = 0$ and $\kappa = \kappa_{turbulent}$ in Eq. 3.4. It is assumed that in these experiments heat losses are negligible ($\beta = 1$) and the S_c tabulation

for the S_t calibration/validation was done at various κ values under adiabatic conditions with GRI-Mech 3.0 [22] detailed chemistry mechanism. The values of the turbulent velocity u' and the turbulent integral length scale $l_{int} = u'^3/\epsilon$ in experiments are obtained as specified in the original references. In occasions where the integral length scale l_{int} is not given, the largest length scale of turbulence $l_0 = k^{1.5}/\epsilon$ is assumed to be equal to the mean radius R_{sch} of spherically expanding turbulent flame. Then the different definitions of turbulent length scale l_t in Eqs. 2.72 and 2.78 are computed from the linear relation between l_0, l_{int} and l_t. The experimental turbulent flame speed data in [63–66] were all measured by reconstructing the average flame radius $R_{sch} \approx R_{c=0.1}$ from Schlieren photography as it evolves in time. Since different references use different experimental turbulent flame speed definitions, in this study the turbulent flame speed data are always extracted from the following definition by manipulating the data of the original references:

$$S_{t,c=0.5} = \left(\frac{1}{1.11} \frac{\rho_b}{\rho_u} \right) \left(\frac{R_{c=0.1}}{R_{c=0.5}} \right)^2 \frac{dR_{sch}}{dt} \tag{3.11}$$

where dR_{sch}/dt is the time derivative of the mean flame radius, as ρ_b and ρ_u are the burnt and unburnt gas density, respectively. The factor $1/1.11$ is an empirical constant proposed in [63] which is needed to convert the displacement speed dR_{sch}/dt measured from Schlieren photography to turbulent mass burning rate. Additionally, the coefficient $R_{c=0.1}/R_{c=0.5} = 1.4$ was suggested in [64] as a converting factor to obtain the turbulent flame speed at $\tilde{c} = 0.5$. For each experiment, the average dR_{sch}/dt value in the interval 25 mm $< R_{sch} <$ 45 mm and the repeated measurements at the same conditions were arithmetically averaged.
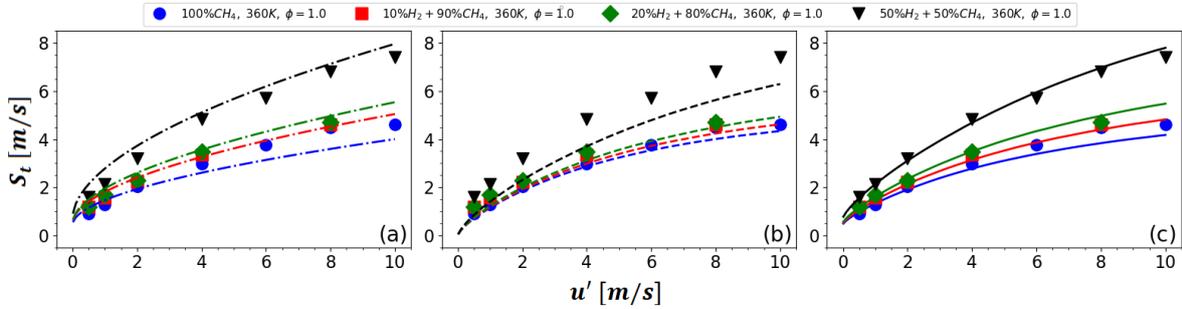
Figure 3.2: Turbulent flame speed S_t versus turbulent velocity u' under atmospheric pressure with varying H_2 contents in CH_4/H_2/air premixed flames (0%, 10%, 20% and 50% volumetric): symbols refer to experimental data from Fairweather et al. [63]. a) S_t from Eq. 2.77, b) S_t from Eq. 2.76, c) the proposed S_t expression, Eq. 3.10. Figure taken from [20].

Figures 3.2 and 3.3 show the comparison of the various turbulent flame speed expressions with experimental data. For the Eq. 2.77 (AFSW model [36]), the agreement between the model and the data is good, except for the 80% H_2+20% CH_4 fuel mixture in Figure 3.3. On the contrary, the Eq. 2.76 (ExtTFC model [6]) matches well with the 100% CH_4 turbulent flame speed data as expected (see [7]), but underpredicts them when H_2 is added to the fuel. The proposed expression (Eq. 3.10) instead matches well with all the experimental data investigated in
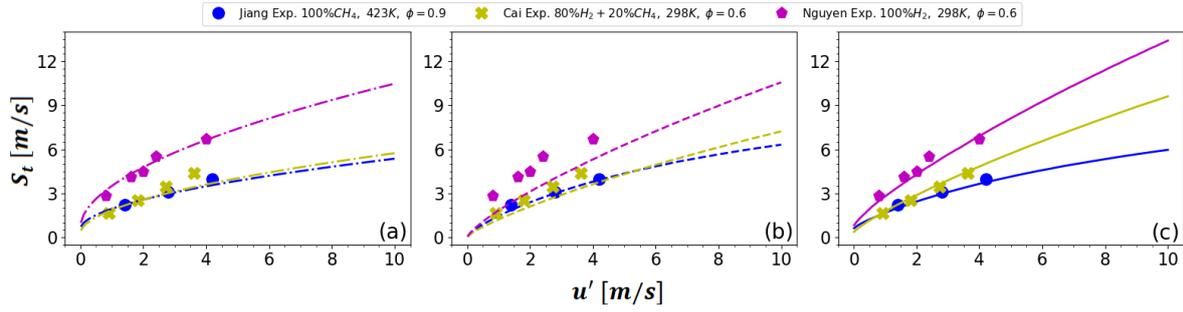
Figure 3.3: Turbulent flame speed S_t versus turbulent velocity u' under atmospheric pressure with varying H_2 contents in CH_4/H_2/air premixed flames (0%, 80% and 100% volumetric): symbols refer to experimental data from Jiang et al. [64], Cai et al. [66] and Nguyen et al. [65]. a) S_t from Eq. 2.77, b) S_t from Eq. 2.76, c) the proposed S_t expression, Eq. 3.10. Figure taken from [20].

this study. Especially, the $Le^{*-0.5}$ factor in the model is fundamental to match the experimental turbulent flame speed data under adiabatic isotropic turbulence conditions.

3.3. MODELLING REACTION RATE SOURCE TERM

Flame surface density models close the reaction rate source term $\overline{\dot{\omega}}$ (source term of the progress variable equation Eq. 2.37) as follows [15, 67]:

$$\overline{\dot{\omega}} = \rho_u \langle S_c \rangle_s \Sigma \tag{3.12}$$

where $\langle S_c \rangle_s$ is defined as the averaged laminar flame speed over the flame surface.

Lindstedt and Vaos assumed $\langle S_c \rangle_s \approx S_{L0}$ and proposed an algebraic relation for the reaction rate source term [68, 69] using fractal theories [47, 48] explained in Section 2.2.2., as follows:

$$\overline{\dot{\omega}} = C_R \rho_u \frac{S_{L0}}{u_{\eta_K}} \frac{\tilde{\epsilon}}{\tilde{k}} \tilde{c} (1 - \tilde{c}) \tag{3.13}$$

where C_R is the model coefficient to be adjusted.

In this study, the following RANS closure is proposed by replacing $C_R S_{L0}$ in the Eq. 3.13 by the proposed turbulent flame speed S_t expression (Eq. 3.10), and the resulting model is entitled as the ExtH$_2$LV model.

$$\overline{\dot{\omega}} = \rho_u \frac{S_t}{u_{\eta_K}} \frac{\tilde{\epsilon}}{\tilde{k}} \tilde{c} (1 - \tilde{c}) \tag{3.14}$$

where $u_{\eta_K} = (\overline{\nu} \tilde{\epsilon})^{0.25}$ is the Kolmogorov velocity scale. The SAS implementation of the proposed closure (Eq. 3.14) is the same as RANS implementation, for its LES implementation, Eqs. 3.10 and 3.14 are transformed using the relations given in Table 3.3.

$$S_{t,SGS} = S_c + \frac{0.4}{\sqrt{Le^*}} u'^{0.8}_{SGS} S_c^{0.45} \alpha_u^{-0.25} \Delta_{LES}^{0.25} \tag{3.15}$$

Table 3.3: Equivalent terms for different turbulence modelling approaches. (For LES, dynamic kinetic energy SGS model is assumed)

Terms	RANS/SAS	LES
Turbulent length scale, l_t	$l_t = C_\mu^{0.75} \frac{\tilde{k}^{1.5}}{\tilde{\epsilon}}$	$\Delta_{LES} = V^{1/3}$
Turbulent velocity, u'	$u' = \sqrt{\frac{2}{3}\tilde{k}}$	$u'_{SGS} = \sqrt{\frac{2}{3}\tilde{k}_{SGS}}$
Turbulence kinetic energy, $\tilde{k}$	$\tilde{k}$	$\tilde{k}_{SGS}$
Turbulence dissipation rate, $\tilde{\epsilon}$	$\tilde{\epsilon}$ for ϵ based model, $\tilde{\epsilon} = C_\mu \tilde{\omega} \tilde{k}$ for ω based model	$\tilde{\epsilon}_{SGS} \approx \frac{\tilde{k}_{SGS}^{1.5}}{\Delta_{LES}}$
Kolmogorov velocity scale, u_{η_K}	$u_{\eta_K} = (\overline{\nu}\tilde{\epsilon})^{0.25}$	$u_{\eta_{K,SGS}} = (\overline{\nu}\tilde{\epsilon}_{SGS})^{0.25}$

$$\overline{\dot{\omega}} = \rho_u \frac{S_{t,SGS}}{u_{\eta_{K,SGS}}} \frac{\sqrt{\tilde{k}_{SGS}}}{\Delta_{LES}} \tilde{c}(1 - \tilde{c}) \tag{3.16}$$

3.3.1. On the derivation of the proposed model

The Eq. 3.14 was found empirically in the seek of the best match with the experimental mean flame shapes. This section describes a possible derivation of this expression. Recalling the flame surface density relation (Eq. 2.22) is the starting point. However, here the probability density function is assumed to be dependent on the Favre averaged progress variable $\tilde{c}$ (as in LV model, Eq. 3.13 [68, 69]) rather than on the Reynolds averaged $\overline{c}$.

$$\Sigma = \left(\frac{L_o}{L_i}\right)^{D-2} \frac{\tilde{c}(1 - \tilde{c})}{\delta_t} \tag{3.17}$$

In Eq. 3.17, the inner L_i and outer cut-off L_o scales can be modelled from the Kolmogorov η_K and the largest turbulent length scales l_0, respectively, and the fractal dimension $D = 7/3$ is assumed as in [48].

$$L_i = \eta_K = \frac{\overline{\nu}^{0.75}}{\tilde{\epsilon}^{0.25}}, \quad L_o = l_0 = \frac{\tilde{k}^{1.5}}{\tilde{\epsilon}} \tag{3.18}$$

Having modelled the inner L_i and outer cut-off L_o scales, if the turbulent flame brush thickness δ_t is modelled from the outer cut-off scale L_o, as $\delta_t = L_o = l_0$, the LV model (Eq. 3.13) can be obtained by substituting the Eqs. 3.17, 3.18 and $\delta_t = L_o = l_0$ into the Eq. 3.12, with an assumption of $\langle S_c \rangle_s \approx S_{L0}$.

On the other hand, if the turbulent flame brush thickness δ_t is modelled similar to the flame surface wrinkling length scale L_y (see Eq. 2.24) defined in the BML model [49, 70]:

$$L_y \propto l_{int} \frac{S_{L0}}{u'}, \quad \delta_t = l_0 \frac{\langle S_c \rangle_s}{S_t} \tag{3.19}$$

the proposed modelling closure (ExtH$_2$LV model, Eq. 3.14) can be derived by substituting the Eqs. 3.17, 3.18 and 3.19 into the Eq. 3.12. In Eq. 3.19, the S_t is the proposed turbulent flame

speed (Eq. 3.10). Comparing δ_t versus L_y (Eq. 3.19), as the major change, u' is replaced by S_t in order to address the stretch, heat loss, and Lewis number effects by means of the proposed S_t (Eq. 3.10) expression. This change is reasonable since the relation $S_t \propto u'^{0.7-0.8}$ is known from literature studies [20, 55] (also see Section 2.2.1.).

Note that, in the context of this thesis study, the expression (Eq. 3.19) used for modelling the turbulent flame brush thickness δ_t, was not investigated exclusively against the experimental measurements as was done for the turbulent flame speed S_t in Section 3.2.. In this regard, the Eq. 3.19 is not proposed for modelling the turbulent flame brush thickness itself, as this requires an exclusive validation and calibration study similar to what was done for the proposed S_t in Section 3.2.. The proposed closure (ExtH$_2$LV model) in Section 3.3., which is validated in RANS, SAS, and LES context CFDs against experiments in Chapters 5 and 6, should be used for modelling the reaction rate source term $\overline{\dot{\omega}}$ itself.

EXPERIMENTAL AND NUMERICAL SETUPS

In this chapter, the experimental setup is outlined, numerical setups are described, cold-flow results are compared with the cold-flow experimental data, and the look-up tables used in the CFDs are presented.

4.1. EXPERIMENTAL SETUP

The experimental data used to validate the models in this paper were measured in an atmospheric bluff body stabilized test rig at the *Norwegian University of Science and Technology* (NTNU) by Æsøy et al. [3]. The test rig is shown in Figure 4.1 and consists of a cylindrical combustion chamber that has an inner diameter of $d_q = 44$ mm with 3 mm thick quartz walls and has a length of $L_q = 75$ mm. In CFD simulations, the length of the combustion chamber is doubled in order to facilitate the flow continuity ($L_q = 150$ mm in Figure 4.2). The combustor has been operated $P = 1$ atm and $T_\infty = 296$ K with five different mixtures of CH$_4$/H$_2$/air premixed gas, from 0% H$_2$ to 100% H$_2$ content in the fuel. The mixture properties and inlet conditions are presented in Table 4.1. The flow rates are adjusted by *Alicat* mass flow controllers, and the bulk flow velocity is calculated from the volumetric flow rate. Air and fuel are mixed a meter before the plenum entrance in order to provide a fully premixed condition. The mixture enters a pipe section with $d_p = 19$ mm. The flame is stabilized by a bluff-body ($d_b = 13$ mm) producing a blockage ratio of 47% and supported by a center rod ($d_r = 5$ mm). The rod is held by three grub screws ($d_g = 4$ mm) at 45 mm upstream from the dump plane as sketched in 4.1. Particle image velocimetry measurements of the cold flow were carried out using *Phantom V2012* (*LaVision IRO*) camera and a *Photonics DM100* dual head laser, by ensemble averaging of 5000 vector fields. The OH* chemiluminescence line-of-sight measurements were captured using the same camera setup with a *Cerco 2178UV 100F/2.8* lens equipped with a 310610-nm bandpass filter, and were converted to $x - z$ planar (see Figure 4.2) views using a three-point Abel deconvolution.

Table 4.1: Operating conditions in terms of thermal power, the volume fraction of H$_2$ in the fuel, equivalence ratio, and inlet bulk velocity.

Power [kW]	V_{H_2} [%]	ϕ [-]	u_{inlet} [m/s]
7	0	0.7	11.8
7	25.2	0.7	11.8
7	56.6	0.7	11.5
7	67	0.7	11.4
7	100	0.4	17.1

Acoustic forcing was provided by horn drivers with harmonic signals having an amplitude equal to 4% of the inlet bulk velocity (u_{inlet}) for a range of discrete frequencies between 200 Hz
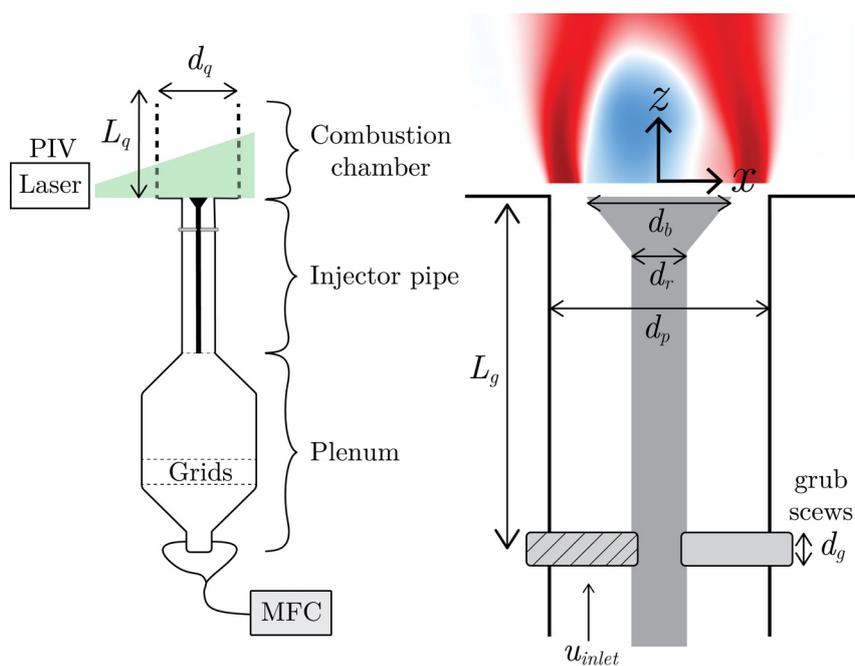
Figure 4.1: NTNU single sector atmospheric test rig schematical view.
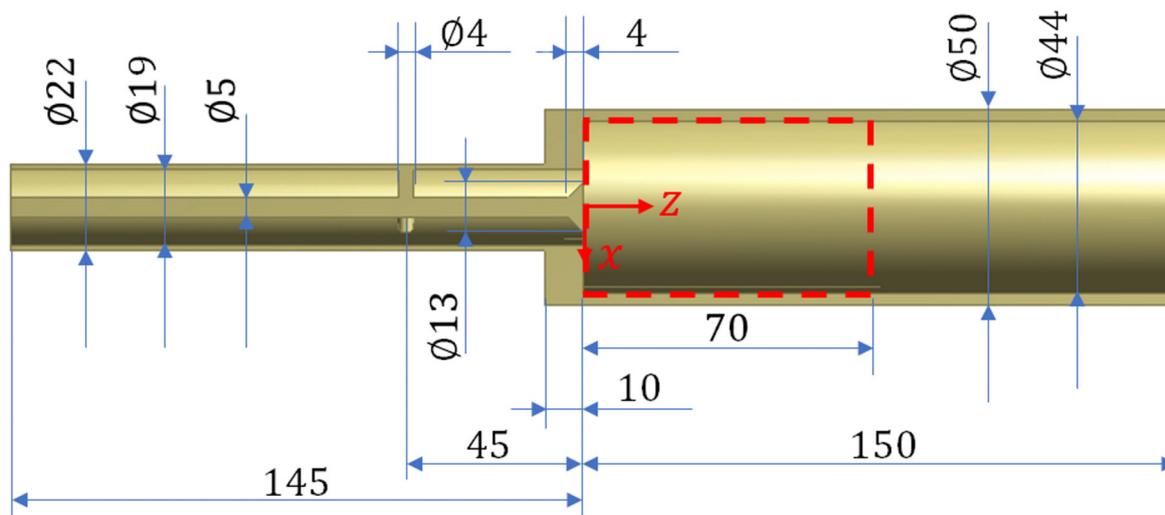
Figure 4.2: NTNU single sector atmospheric test rig CAD model measurements (combustion chamber length is doubled in the CFD simulations). The red dashed rectangle refers to the $x - z$ comparison plane between CFD and experimental results.

and 2200 Hz. The flame response to acoustic forcing was measured by spatially integrating the heat release rate measured by tracking the radiation emitted from OH* radicals, using a photo-multiplier tube (PMT) equipped with an ultra-violet (UV) bandpass filter. Velocity fluctuations at the dump plane were measured by means of a multiple microphone method (MMM). Further details about the experimental setup and the measurement methods can be found in [3].

4.2. NUMERICAL SETUP

CFD simulations are carried out in the *ANSYS FLUENT 2019 R3* CFD solver. An incompressible gas formulation is used to calculate the local gas density under atmospheric pressure. The turbulent premixed combustion models are implemented via User Defined Functions (UDF). The turbulence models are selected as follows; ϵ based linear pressure-strain RSM model with non-equilibrium wall functions in RANS calculations, ω-based stress-omega RSM model in SAS calculations, and the dynamic kinetic energy SGS model with wall resolving approach in LES calculations. Mixture thermal conductivities and viscosities are defined as temperature-dependent polynomial coefficients in the CFD solver. The coefficients are obtained by curve fitting the calculated properties across the flame thickness in freely propagating flamelet configuration in *CANTERA*.

4.2.1. Discretization schemes

Numerical discretization schemes are selected as follows: pressure velocity coupling is discretized using the coupled scheme in the RANS calculations, and the SIMPLEC scheme for the SAS and LES calculations. Second-order discretization is used for pressure in all the calculations. Second-order upwind discretization is selected for the Reynolds stress equations, and QUICK scheme is selected for the other equations. For LES and SAS, the second-order implicit transient formulation is selected for the time discretization, and bounded central differencing is selected for the momentum equations. $\Delta t = 10^{-5}$ s is used as the time step for the transient calculations (SAS and LES). It is specified provided that the maximum convective CFL (Courant-Friedrichs-Levy) number is around unity in the combustion chamber, and the same Δt is used for both unforced and acoustically forced cases. Mean quantities are obtained by averaging the solution over 2 flow-through times after a steady state condition is achieved. Collecting statistics over 4 flow-through times was also attempted for some cases, and no change was observed in the quantities investigated in this study (i.e. mean velocity field, mean flame shape, axial heat release rate, etc.).

4.2.2. Mesh configurations and boundary conditions

Four different mesh configurations are used in this study and the meshes were generated in *BE-TACAE ANSA 20* software. Figures 4.3 and 4.4 show the mesh configurations and the boundary conditions (BC) nomenclature for the CFD simulations.

C1 mesh configuration for RANS cases

The C1 mesh configuration (see Figure 4.3 a)) was generated for RANS cases and is composed of 4.5 million fluid and 0.5 million solid cells. This mesh has the average $y^+ \approx 2$ value in the whole domain, having $y^+ \approx 3$ in the inlet pipe and $y^+ \approx 1$ in the combustion chamber section.

The velocity inlet BC is defined at the inlet boundary (BC 1 in Figure 4.4), and the inlet

a) C1, Fluid zone: 4.5 million cells, Solid zone: 0.5 million cells

b) C2, Fluid zone: 13.5 million cells

c) C3, Fluid zone: 13.5 million cells, Solid zone: 1.5 million cells

d) C4, Fluid zone: 3.5 million cells, Solid zone: 0.5 million cells
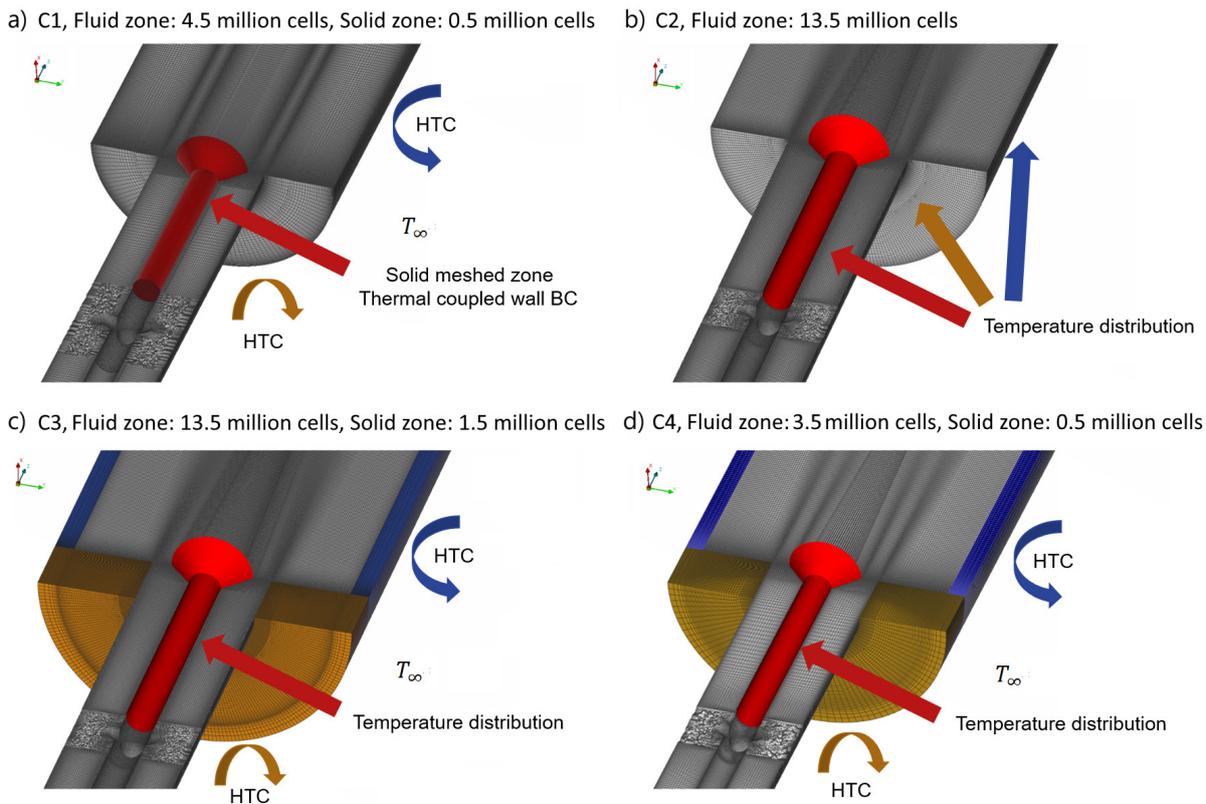
Figure 4.3: Mesh configurations used in the CFD simulations.
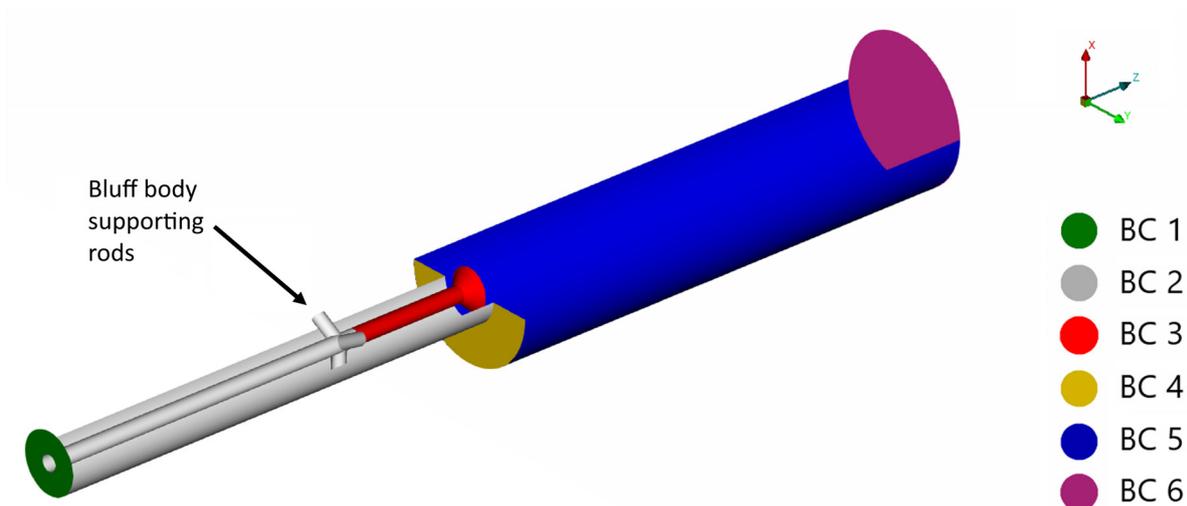
Figure 4.4: Boundary conditions nomenclature.

turbulence level is defined from the turbulence intensity and hydraulic diameter option in *ANSYS FLUENT 2019 R3* with the values of $I = 5\%$ and $d_{hyd} = 0.014$ m, respectively. The pressure outlet is defined as the outlet boundary condition (BC 6 in Figure 4.4).

The bluff body (BC 3 in Figure 4.4) was modelled as a solid meshed zone up to 35 mm

upstream of the dump plane, and a thermally coupled wall boundary condition was applied to its surfaces, which allows conjugate heat transfer between adjacent solid and fluid zones. The length of 35 mm of the solid modelled bluff body was tested in the RANS calculations, and it was observed that the solid temperature reaches the unburnt mixture temperature before the cut of the solid meshed zone 35 mm upstream from the bluff body top surface. Therefore, adiabatic wall boundary condition was assigned to the walls beyond this point ($z < -35$ mm). In Figure 4.4, BC 2 refers to the adiabatic wall boundary condition.

The back and side walls of the combustion chamber (BC 4 and BC 5 in Figure 4.4) were modelled from *ANSYS FLUENT 2019 R3* shell conduction model which is defined by the wall thickness, the number of cells across the thickness, and thermal boundary condition at the wall boundaries. It automatically grows solid cell layers in the surface normal direction and allows conjugate heat transfer during the solution process [50]. Four cells are defined across the back (BC 4, $t_{bw} = 10$ mm) and side wall (BC 5, $t_{sw} = 3$ mm) thicknesses, and conjugate heat transfer is solved by defining heat transfer coefficient (HTC) and ambient temperature T_∞.

C2 & C3 mesh configurations for LES cases

C2 and C3 mesh configurations were formed for the LES simulations. They have the same fluid zone mesh composed of 13.5 million cells. The difference is that the C2 configuration does not include a solid meshed zone, and temperature distribution obtained from RANS cases (C1 mesh configuration) imposed at combustion chamber walls, while in the C3 mesh configuration, combustion chamber back and side walls (BC 4 and BC 5 in Figure 4.4) are modelled as solid meshed zones and conjugate heat transfer is solved. These mesh configurations have $y^+ \leq 1$ in the fluid domain. The mesh resolution is tested with the Çelik LES quality indicator [71]:

$$IQ_{LES,\nu} = \frac{1}{1 + 0.05 \left[\frac{\nu + \nu_{SGS}}{\nu}\right]^{0.53}} \qquad (4.1)$$

Figure 4.5 shows the $IQ_{LES,\nu}$ values at various section planes in the computational domain for the cold and reacting flow cases corresponding to the 0% H_2 case in Table 4.1. For a good quality LES simulation, resolving minimum 80% of kinetic energy, $0.8 \geq IQ_{LES,\nu} \geq 1$ is suggested in [71]. As observed from Figure 4.5, the mean value of $IQ_{LES,\nu}$ is varying between 0.9 to 0.95 for the cold flow and varies in a higher range for reacting flow, which confirms the sufficient resolution of the LES mesh, used in this study.

For both C2 and C3 mesh configurations, BC 1, BC 2, BC 3 and BC 6 boundary conditions (see Figure 4.4) are defined the same as follows; velocity inlet, adiabatic wall, temperature distribution from C1 mesh configuration and pressure outlet, respectively. In the C2 mesh configuration, BC 4 and BC 5 are also defined as temperature distributions, which are obtained from the RANS solution in the C1 mesh configuration. However, in the C3 mesh configuration, HTC and T_∞ are defined for BC 4 and BC 5, and the conjugate heat transfer is solved. The inlet turbulence levels are defined from the turbulence intensity ($I = 5\%$) and hydraulic diameter ($d_{hyd} = 0.014$ m) option as the same in RANS with C1 mesh configuration for both C2 and C3 setups, and the inlet turbulence is generated with the spectral synthesizer method.

C4 mesh configuration for SAS cases

C4 mesh configuration was prepared for the SAS simulations. This configuration has 3.5 million cells in the fluid zone and 0.5 million cells in the solid zone. This mesh was constructed by
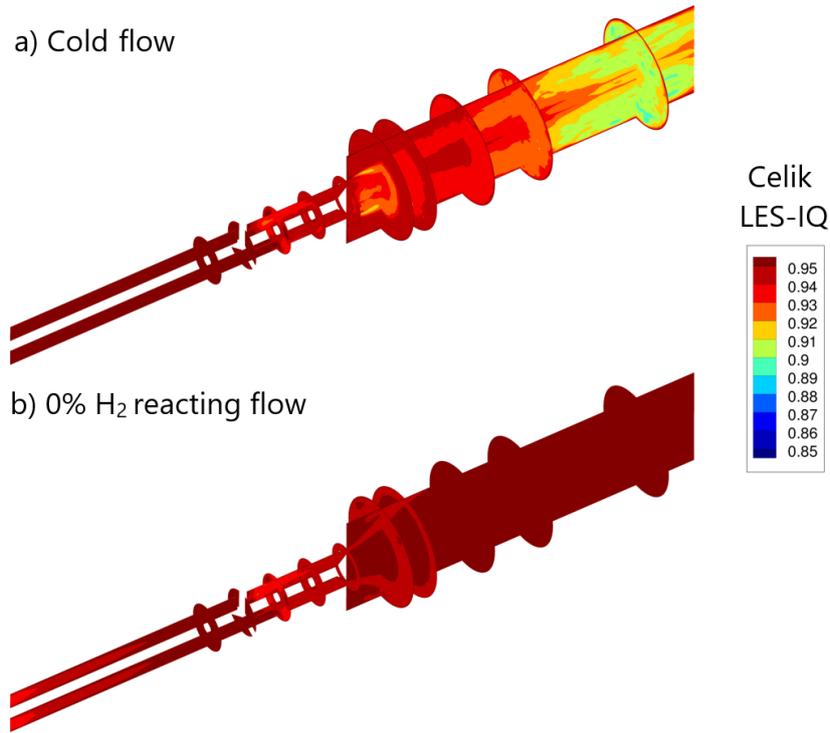
Figure 4.5: Mean $IQ_{LES,\nu}$ contours for a) cold flow and b) 0% H_2 reacting flow.

coarsening the RANS mesh in the streamwise direction but preserving similar y^+ values. As explained in Chapter 2, SAS is an improved URANS formulation exhibiting LES-like behaviour (reflects the scales of turbulence) through an additional source term in the specific dissipation rate ω equation. To this end, it requires a mesh finer than RANS, which is contradictory to what was done in this study. However, in this study, the SAS cases were conducted to show the proposed combustion model applicability with different turbulence modelling approaches and to see whether the SAS could be a low-cost alternative to LES with the proposed combustion modelling approach. Thus, a coarse mesh was constructed for the SAS cases. Note that the RSM-based SAS version selected in this study solves 7 equations for turbulence modelling (see Chapter 2), meaning that for an equal size of the mesh, SAS would require much higher computational resources than LES.

For this configuration, the boundary conditions are identical to those in the C3 mesh configuration used for LES with conjugate heat transfer. In both C3 and C4 mesh configurations, the back and side walls of the combustion chamber (BC 4 and BC 5 in Figure 4.4) were modelled as solid zone mesh rather than a shell conduction model used for RANS cases in the C1 mesh configuration. The shell conduction model is beneficial in RANS calculations for saving time spent on meshing, however, in transient calculations, *ANSYS FLUENT 2019 R3* this model does not allow defining a solid time step uncoupled from the flow time for the shell conduction zones, instead, it requires physically generated solid mesh zones. Defining an uncoupled time step for solid zones is crucial in transient simulations in order to quickly reach the thermally steady state condition. For that reason, in C3 (for LES) and C4 (for SAS) configurations with conjugate heat transfer, solid mesh zones were generated in the meshing software, and a higher

time step ($\Delta t = 0.1$ s) than the flow time step ($\Delta t = 10^{-5}$ s) was defined for the solid walls until the steady state condition was achieved. The required time to reach the thermal steadiness τ_s was calculated following [27]:

$$\tau_s = \frac{V_s \rho_s C_{p,s}}{\text{HTC} \cdot S} \tag{4.2}$$

where $V_s, \rho_s, C_{p,s}$ represent the volume, density and specific heat of the solid zone, S is the heat transfer surface area and HTC is the external flow heat transfer coefficient. When the thermally steady state condition was achieved, the solid time step was equated to the flow time step.

Solid cell zone thermal properties for the quartz side wall, Inconel back wall and the bluff body are introduced as temperature-dependent polynomials and the temperature-dependent data is obtained from [72, 73] for the quartz, and from [74] for the Inconel materials in all the mesh configurations.

4.2.3. Heat transfer coefficient (HTC) predictions

In the experiments, wall temperatures had not been measured, and the experimental setup had been placed under a large diffuser flue-gas stack which induces forced convection over the side wall of the combustion chamber. To estimate the HTC at the side wall surface, temperature measurements taken for a similar setup (square section combustion chamber operated with an ethylene flame) were used. For these measurements, the average temperature was in the range of 593–833 K (at different axial locations from $z = 0.01$ m to $z = 0.03$ m) on the outside surface of the combustor wall. Aiming at the best match in the mean flame shape and the wall temperature, a parametric study was carried out by assigning different HTCs. In the end, it was revealed that the HTC $= 100 - 150$ W/m²K range provided the best agreements with experiments. The specific value used in CFDs is stated in the results chapter. For the back wall heat transfer coefficient, HTC $= 8.6$ W/m²K is calculated from Yang's natural convection relation for cylindrical bodies [75] as follows:

$$Nu_D = 0.36 + \frac{0.670 \left(Ra_D D/H \right)^{1/4}}{\left[1 + (0.492/Pr)^{9/16} \right]^{4/9}}$$

$$Nu_H^{0.5} = 0.60 \left(\frac{H}{D} \right)^{0.5} + 0.387 \left[\frac{Ra_H}{\left[1 + (0.492/Pr)^{9/16} \right]^{16/9}} \right]^{1/6} \tag{4.3}$$

where D and H are the diameter and the length of the cylindrical body, and Nu, Ra, and Pr are the Nusselt, Rayleigh and Prandtl numbers, respectively. The HTC calculation was done based on both the diameter $Nu_D = \frac{\text{HTC} \cdot D}{k}$ and the length $Nu_H = \frac{\text{HTC} \cdot H}{k}$ of the combustion chamber and very close values were obtained. Finally, the average value of HTC $= 8.6$ W/m²K was used in the CFDs. For the ambient temperature, $T_\infty = 296$ K was assigned.

4.3. COLD FLOW RESULTS

The cold flow validations of RANS, SAS, and LES implementations are presented in this chapter. Figure 4.6 shows the axial and transversal velocity contours, and Figure 4.7 shows the mean and RMS (root mean square) values of the axial and transversal velocity plots for the case with $u_{inlet} = 11.8$ m/s (representative of the fuel mixtures 0-67% H_2 in Table 4.1) from cold flow experiment against RANS, SAS and LES simulations. In RANS, RMS velocities were evaluated by computing the square root of the respective Reynolds stresses, in SAS and LES, mean and RMS values were obtained by averaging the flow over 4 flow-through times.
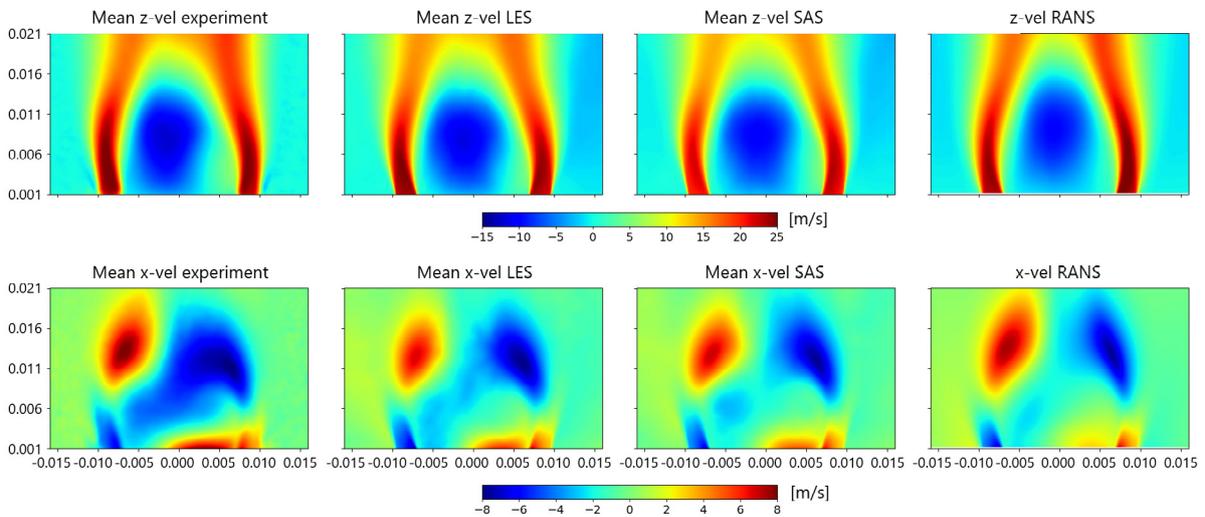
Figure 4.6: Cold flow axial (z-vel.) and transversal (x-vel.) velocity contours comparison: Experiment vs LES vs SAS vs RANS.

The asymmetric axial velocity distribution seen in Figures 4.6 and 4.7 is due to the bluff body supporting rods shown in Figure 4.4. It is well reproduced by the CFD simulations, especially with LES and SAS for the mean velocity (see Figures 4.6 and 4.7), and with some deviations in the RMS plots (see Figure 4.7). Similar trends are also observed in transversal velocity plots, having good agreements in the mean velocity plots, with slight over/under-predictions in the RMS plots.

Figure 4.8 shows the velocity power spectral density (PSD) measured by a hotwire and sampled from SAS and LES at a point ($x = -8$ mm, $y = 0$ mm, $z = 0$ mm). A relatively good agreement between the experiment, SAS, and LES is achieved. Calculated and measured PSD curves have the same slope up to the high-frequency range (around 10^3 Hz for SAS, 10^4 Hz for LES) showing that SAS and LES capture the correct characteristics of the flow for the large scales of turbulence. The deviations at the high-frequency range are attributed to the modelling effects at the sub-grid-scale. The deviation starts earlier for SAS due to its lower resolution mesh compared to LES mesh (see Figure 4.3).
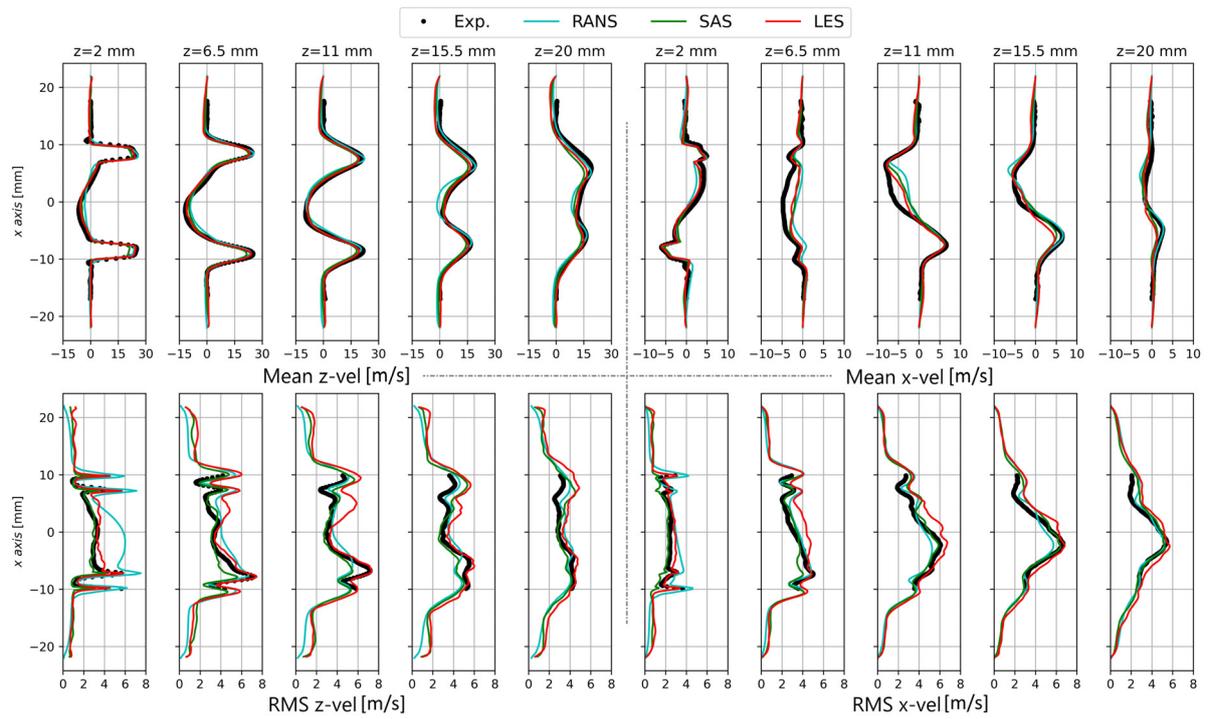
Figure 4.7: Cold flow axial (z-vel.) and transversal (x-vel.) mean and root-mean-square (RMS) plots at various axial plane locations: Experiment vs RANS vs SAS vs LES.
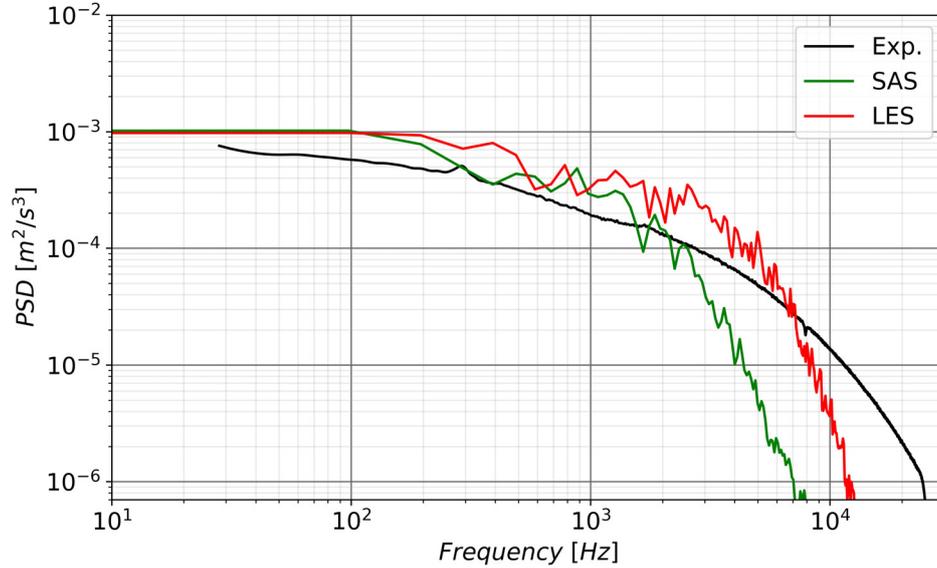
Figure 4.8: Power spectral density of sampled velocity signals at a point ($x = -8$ mm, $y = 0$ mm, $z = 0$ mm) from cold flow experiment, SAS and LES.

4.4. LOOK-UP TABLES

Figure 4.9 shows the tabulated laminar flame consumption speed S_c plots against various stretch κ and heat loss levels β for the mixtures listed in Table 4.1. These look-up tables are generated
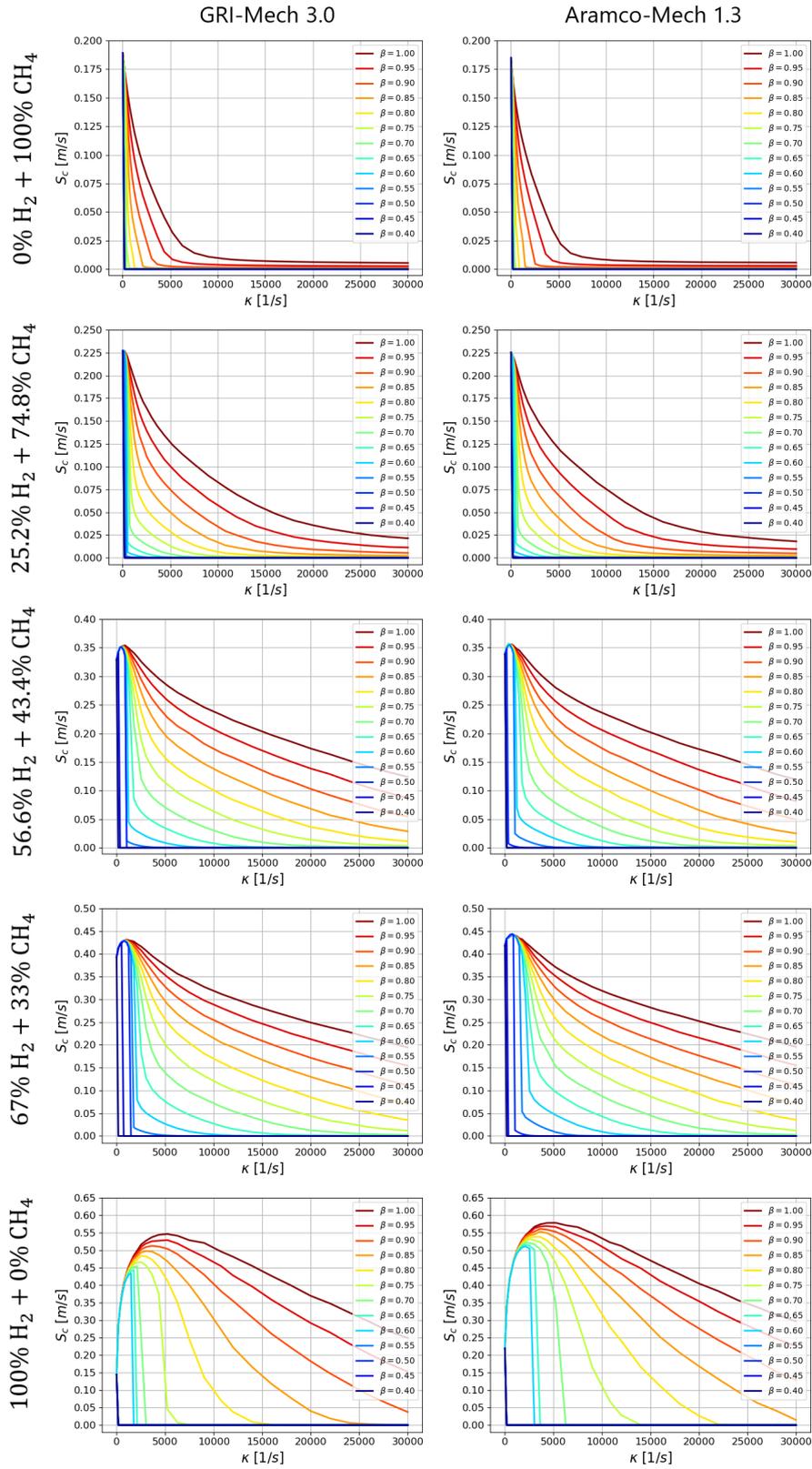
Figure 4.9: Tabulated laminar flame consumption speeds S_c at various stretch κ and heat loss levels β for different contents of H_2 with GRI-Mech 3.0 [22] and Aramco-Mech 1.3 [76] detailed chemistry mechanisms. Calculations are done in fresh-to-burnt counter flow flame configuration in *CANTERA*.

as explained in Section 3.1.1., called by the CFD solver during the solution, and the $S_c(\kappa, \beta)$ value is interpolated, based on the modelled total stretch (κ from Eq. 3.4) and heat loss parameter (β from Eq. 3.9) values, over the computational domain.

In this study, two different detailed chemistry mechanisms namely the GRI-Mech 3.0 [22] and the Aramco-Mech 1.3 [76] are used for the tabulation calculations. Past studies in the literature found that laminar flame speeds for CH_4/H_2/air mixtures calculated with these two mechanisms are in reasonable agreement with experimental data [77, 78]. Multicomponent transport formulation is used with enabled Soret effects (thermal diffusion effects). While the look-up tables were generated, the heat loss parameter β was sampled between 1-0.4, and the stretch κ was sampled between 0-150000 1/s, where the ranges up to 30000 1/s are shown in Figure 4.9.

Figure 4.9 shows that at high values of stretch and heat losses a high decrement in the consumption speed is observed indicating strong levels of quenching [79]. Increasing hydrogen content decreases the sensitivity of consumption speed to flame stretch and heat losses [20, 80]. For the mixtures with H_2 addition, flame stretch increases the consumption speed initially and then decreases. This trend is not observed on the pure CH_4 flames as S_c has a monotonic decrease with increasing flame stretch. The increment of S_c from low stretch values is attributed to the high diffusivity (Le number effect) of H_2, and this effect increases and becomes more remarkable with the increasing content of the hydrogen in the mixture [81].

Another observation from Figure 4.9 is that the GRI-Mech 3.0 [22] and the Aramco-Mech 1.3 [76] chemistry mechanisms calculate almost the same results for low contents of hydrogen (see the first three rows in Figure 4.9), however, for the high content hydrogen, especially for the pure hydrogen flame, the Aramco-Mech 1.3 calculates higher S_c values than the GRI-Mech 3.0.

FLAME STABILIZATION PREDICTIONS

In this chapter, the premixed combustion models described in Chapters 2 and 3 are implemented in RANS, SAS and LES context CFDs, and the mean flame shape predictions are compared with the experiments. The chapter is split into four sections;

The first section aims at showing the effects of including the stretch κ, heat loss β and effective Lewis number Le^* into the reaction rate closure. To this end, the proposed turbulent flame speed expression $S_t = f(\kappa, \beta, Le^*)$ (Eq. 3.10) is incorporated into the TFC closure ($\overline{\omega} = \rho_u S_t |\nabla \tilde{c}|$) in the RANS context CFDs and its flame shape predictions are compared with experiments and the other two TFC-based closures with $S_t = f(\kappa, \beta)$ and $S_t = f(Le^*)$.

The purpose of the second and third sections is to seek the best match with experiments in RANS and LES context CFDs for the mean flame shape predictions. In this regard, the proposed S_t expression (Eq. 3.10) is incorporated into four different reaction rate closures which are selected as the two having the $\overline{\omega} \propto |\nabla \tilde{c}|$ dependency, and the other two having the $\overline{\omega} \propto \tilde{c}(1 - \tilde{c})$ dependency. In the second section, all four closures are implemented in RANS context CFDs, and the two closures (one with $\overline{\omega} \propto |\nabla \tilde{c}|$ and the other with $\overline{\omega} \propto \tilde{c}(1 - \tilde{c})$) best representing the experimental flame shapes are selected. These two closures are then implemented in LES context CFDs in the third section. In conclusion, the model with which the best match was achieved in both RANS and LES CFDs is selected as the proposed closure (ExtH$_2$LV closure, see Section 3.3.).

In the last section, the sensitivies in the mean flame shape predictions of the proposed ExtH$_2$LV closure to the different turbulence modelling approaches, different stretch modelling approaches and different heat loss levels are investigated. The ExtH$_2$LV closure is implemented in RANS, SAS and LES context CFDs: in SAS and LES implementations, different resolved stretch modelling approaches are tested for their impacts on the flame stabilization, and in RANS and LES context CFDs, the effect of different heat loss levels is investigated.

5.1. EFFECT OF TURBULENT FLAME SPEED IN RANS CFD

In this section, performances of the three turbulent flame speed S_t correlations; Eq. 2.76, Eq. 2.77, and the proposed Eq. 3.10, are tested in TFC based closure in RANS context CFDs. The progress variable $\tilde{c}$ equation (Eq. 2.37) is solved, and the reaction rate source term $\overline{\omega}$ is modelled from Eq. 2.68 for all the S_t correlations. Thus, the influence of only the S_t on the flame shape is able to be tested.

The reaction rate closure $\overline{\omega}$ and the three S_t correlations are restated below. For simplicity in results interpretation, Eqs. 2.76, 2.77 and 3.10 are referred to as ExtTFC, AFSW and ExtH$_2$TFC models, respectively.

$$\overline{\omega} = \rho_u S_t |\nabla \tilde{c}| \tag{2.68}$$

$$S_t = 0.52u'^{0.75}S_c^{0.5}\alpha_u^{-0.25}l_t^{0.25}, \quad \text{(ExtTFC)} \tag{2.76}$$

$$S_t = S_{L0} + \frac{0.46}{\exp{(Le^* - 1)}}u'^{0.55}S_{L0}^{0.7}\nu_u^{-0.25}l_t^{0.25}\left(\frac{P}{1 \text{ atm}}\right)^{0.2}, \quad \text{(AFSW)} \tag{2.77}$$

$$S_t = S_c + \frac{0.4}{\sqrt{Le^*}}u'^{0.8}S_c^{0.45}\alpha_u^{-0.25}l_t^{0.25}, \quad \text{(ExtH}_2\text{TFC)} \tag{3.10}$$

The RANS CFD calculations are carried out for all the mixtures listed in Table 4.1, and compared with the experimental data described in Section 4.1. C1 mesh configuration (see Figures 4.3 and 4.4) is used for the simulations, with the numerical details given in Section 4.2. for the RANS implementation. The ϵ based Reynolds stress model with non-equilibrium wall functions is selected as the turbulence model. Stretch and heat loss are modelled from Eqs. 3.4 and 3.9 for ExtTFC and ExtH$_2$TFC models as explained in Chapter 3, and the HTC = 150 W/m^{2}K is assigned as the heat transfer coefficient to the side walls of the combustion chamber (BC 5 in Figure 4.4). The effective Lewis number Le^* is calculated from Eq. 2.79 for AFSW and ExtH$_2$TFC models. The strained non-adiabatic S_c tabulation is done as explained in Section 3.1. and plotted in Section 4.4. with GRI-Mech 3.0 [22] detailed chemistry mechanism.

In Figure 5.1, the normalized heat release rate contours from the three different turbulent flame speed models are compared with the normalized Abel deconvoluted OH* chemiluminescence images from experiments. The heat release rate is linearly proportional to the reaction rate source term $\overline{\dot{\omega}}$ (Eq. 2.68) in CFD simulations and to OH* chemiluminescence in experiments for perfectly premixed flames [82, 83].

5.1.1. Mean flame shapes

For 0% H$_2$ (first row of Figure 5.1), the ExtTFC and ExtH$_2$TFC models can correctly capture the mean flame shape producing a V-flame (stabilization mainly in the inner shear layer) as in the experiment due to quenching effects in the outer shear layer. Flame stretch combined with heat loss is present in the outer shear layer (see Figure 5.1 b) and c)), inducing quenching effects. The AFSW model produced the M-flame shape (strong reaction in the inner and outer shear layers) even under non-adiabatic conditions. The quenching in the outer layer seen in experiments is not captured (see Figure 5.1 a)) because the AFSW model does not consider the combined quenching effect of stretch and heat losses. The angle (with respect to the axial axis) of the inner flame with the AFSW model is smaller than in experiments and extended models. Axial velocity contours in Figure 5.2 show strong variations in the flow field between the M-flame with the AFSW model and the V-flame with the ExtH$_2$TFC model. This indicates that the prediction of flame topology has a strong impact on the flow field prediction.

The normalized axial heat release distribution is shown in the right column of Figure 5.1. The AFSW model shows high values close to the dump plane producing a shorter flame than experiments and extended models. Extended models show a better agreement to experiments due to the similar flame shape. Results with 0% H$_2$ using the ExtTFC and ExtH$_2$TFC models are similar as Lewis number is close to 1.
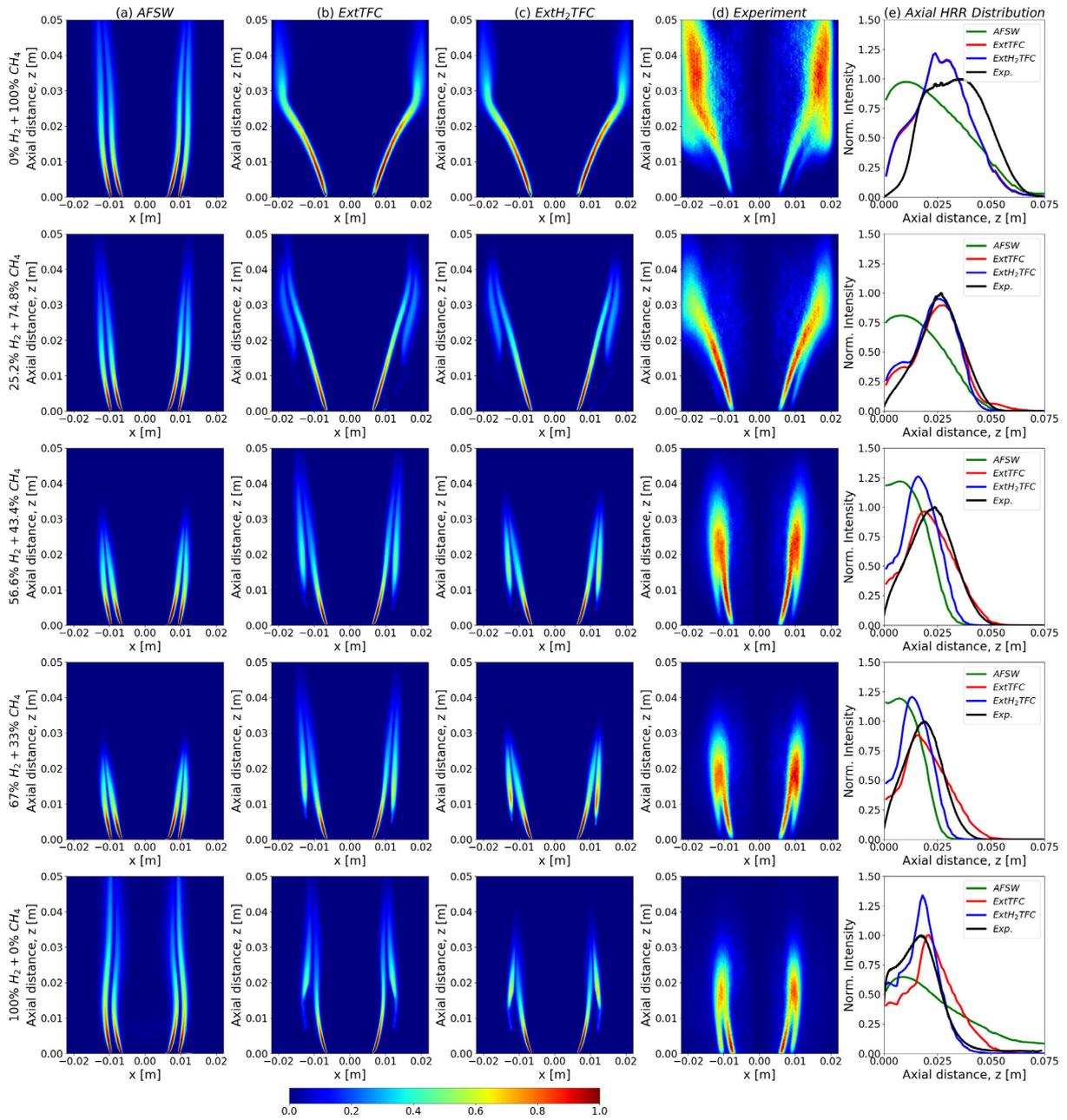
Figure 5.1: Heat release rate distributions from three different turbulent flame speed models: a) AFSW, b) ExtTFC, c) ExtH$_2$TFC and d) Abel deconvoluted OH* chemiluminescence images from experiments. e) Normalized axial heat release rate distributions are shown in the right column. In columns a) to d) values are normalized with the maximum local intensity and in column e) axial HRR curves are normalized provided that the areas under the curves are equal to those from experiments. Figure is taken from [20].

The impact of H$_2$ addition into the mixture is shown in Figure 5.1. The 100% H$_2$ case has higher inlet velocity and leaner mixture than the other cases (see Table 4.1). Reactivity and turbulent flame speed increase with H$_2$ addition, producing a decrease in flame length and a change in flame topology after a certain % of H$_2$ content. In experiments, flame stabilization in
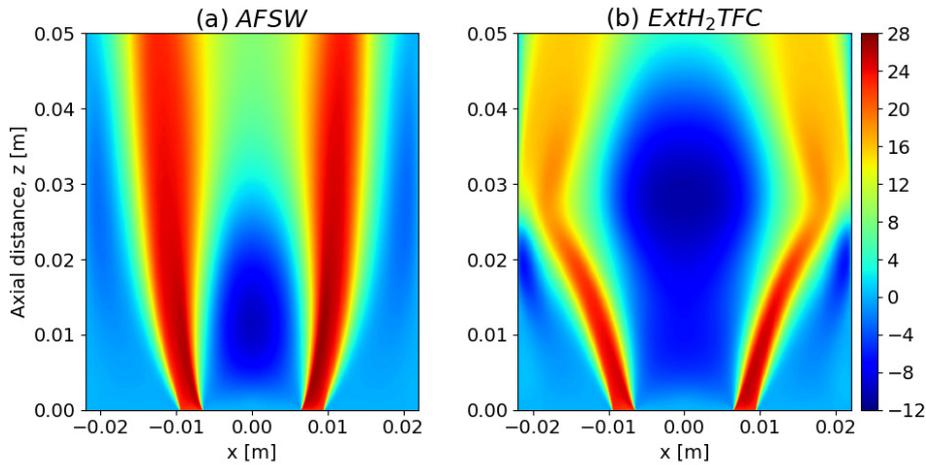
Figure 5.2: Axial velocity contours from reacting flow for a) AFSW and b) ExtH$_2$TFC models. Figure is taken from [20].

the outer shear layer starts to develop with 25.2% H$_2$, leading to M-flame with 56.6% H$_2$. This transition effect is captured by the ExtTFC and ExtH$_2$TFC models (see the second row of Figure 5.1 b) and c)). Calculations with the AFSW model show the M-flame shape for all H$_2$ contents with similar heat release intensity in both inner and outer layers (Figure 5.1 a)). M-flames with extended models show a lower reaction rate in the outer shear layer compared to the inner layer due to quenching effects.

Comparing extended models with experiments (Figure 5.1 b), c) and d)), the heat release contours with the ExtH$_2$TFC model show good agreement in the flame shape for all the H$_2$ contents. For cases with H$_2$ > 50%, both extended models (see Figure 5.1 b) and c)) overpredict the flame quenching in the outer shear layer region close to the dump plane which is highly affected by heat losses. Experiments show a certain level of reaction rate in that area. As shown in Figure 5.3 a), quenching occurs with $\beta \leq 0.5$, producing overprediction of quenching on that region.

In addition, the ExtTFC model for the 56.6%, 67% and 100% H$_2$ cases show that the model predicts the same flame length for all three cases (see red lines belonging to 56.6%, 67% and 100% H$_2$ cases in Figure 5.1 e), all three reach to zero intensity at $z = 0.05$ m) while both AFSW and ExtH$_2$TFC models predict decreasing flame lengths as H$_2$ percentage is increasing due to the inclusion of the effective Lewis number Le^* term in the expressions. The ExtH$_2$TFC model has an improvement compared to the AFSW and ExtTFC models as it includes together the quenching effects due to stretch and heat losses and the increase in flame reactivity due to Lewis number effects by H$_2$ addition.

For 100% H$_2$, the AFSW model shows a longer flame than experiments and extended models, which is opposite to all other %H$_2$ cases shown in the results. The reason for this low reactivity is associated with the fact that with high H$_2$ content, the consumption speed S_c increases with stretch until a certain level and then decreases as seen in Figure 5.3 a). These values even under heat loss effects are higher than the unstretched adiabatic laminar flame speed S_{L0} (Figure 5.3 a) and b)), leading to lower laminar flame speed values in AFSW model than with extended models. The AFSW 100% H$_2$ case is longer than the AFSW 67% H$_2$ case because it
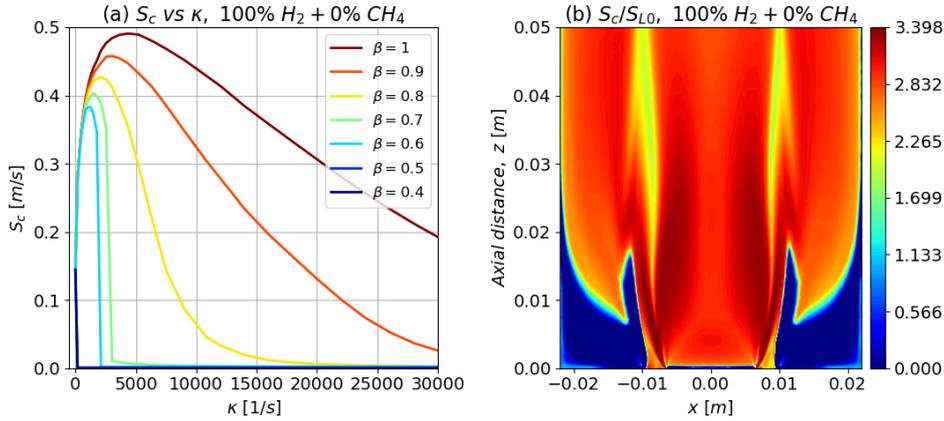
Figure 5.3: a) Tabulated stretched nonadiabatic laminar consumption speed S_c plot b) the contour plot of the ratio of laminar consumption speed S_c to unstretched laminar flame speed S_{L0} (from ExtH$_2$TFC model) for the case with 100% H$_2$ content. Figure is taken from [20].

has a lower equivalence ratio with higher inlet velocity (Table 4.1).

5.1.2. Hydrogen impact on flame stretch and heat loss

The impact of H$_2$ addition on stretch and heat loss is shown in Figure 5.4 with a comparison of the cases with 0% H$_2$ and 56.6% H$_2$. Total stretch values are higher with H$_2$ addition (Figure 5.4 a)) as the term with Le number in Eq. 3.4 produces an increase in the efficiency function, and κ_{mean} also increases in some regions due to the different flow and flame shapes. Similarly, different flow and flame structures affect heat losses too (Figure 5.4 b)).

5.1.3. Conclusions

The proposed turbulent flame speed ($S_t = f(\kappa, \beta, Le^*)$) is compared with the two other relations ($S_t = f(\kappa, \beta)$ and $S_t = f(Le^*)$) against experiments in RANS-based TFC closure. The conclusions from this comparison are listed as follows:

- The proposed $S_t = f(\kappa, \beta, Le^*)$ expression in the TFC closure predicts flame shapes with good agreement with experiments and presents improvements with respect to the other models.

- The inclusion of the effective Lewis number Le^* in the closure is important for the prediction of flame length, especially at high H$_2$ contents in the mixture.

- The predicted correct flame stabilization topology is attributed to the quenching effects produced by the combined effect of flame stretch and heat loss.
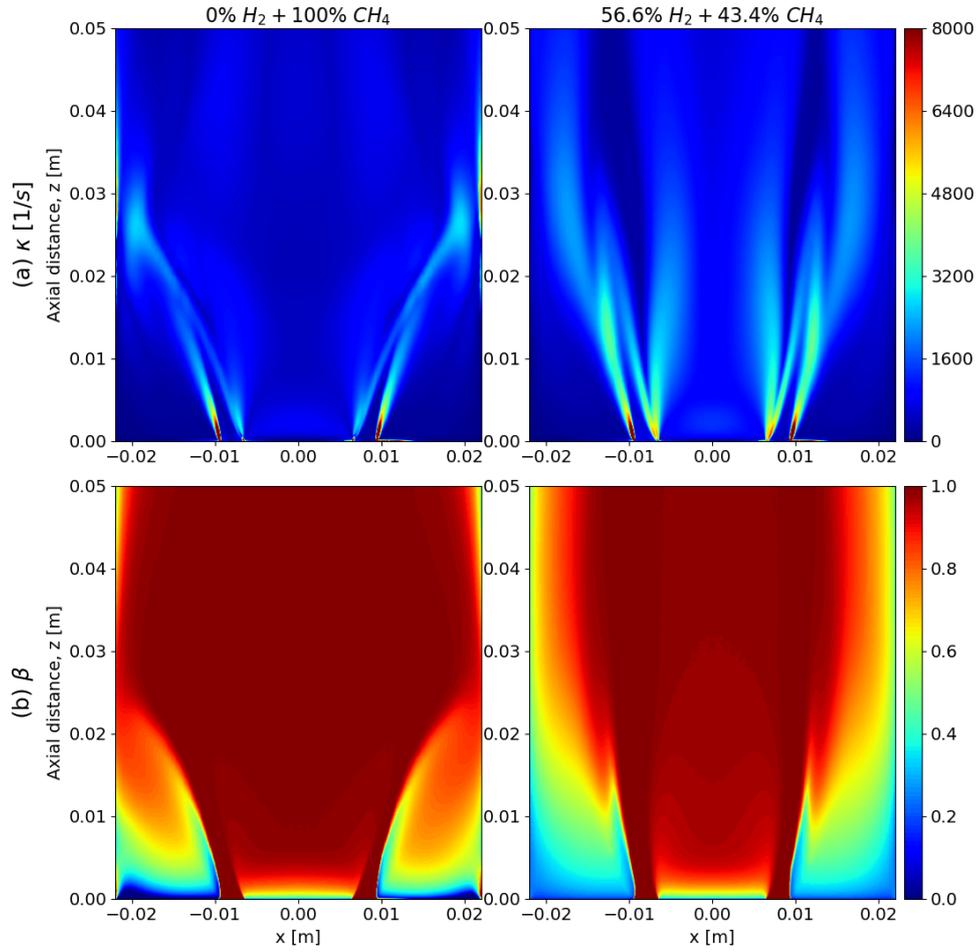
Figure 5.4: a) Total stretch κ and b) heat loss parameter β contours from the cases with 0% and 56.6% H$_2$ contents (obtained with ExtH$_2$TFC model). Figure is taken from [20].

- For improvements in the model, it is observed that close to the dump plane ($z = 0$ in Figure 5.1 e) column, axial HRR distribution plots) there are stronger heat release values in CFD models than in experiments, and the flame brush thickness is predicted thinner than those in experiments.

5.2. EFFECT OF REACTION RATE CLOSURE IN RANS CFD

In this section, the reaction rate closure which can be best coupled with the proposed turbulent flame speed expression Eq. 3.10 is investigated in RANS-based CFD. In this regard, the proposed S_t (Eq. 3.10) is incorporated into four different reaction rate closures explained in Chapters 2 and 3 which are restated here as follows:

$$\overline{\dot{\omega}} = \rho_u S_t |\nabla \tilde{c}| \quad (\text{ExtH}_2\text{TFC}) \tag{2.68}$$

$$\overline{\dot{\omega}} = \rho_u S_t \left[1 + \frac{\tau'}{t_{fd}} \left[\exp\left(-\frac{t_{fd}}{\tau'} - 1 \right) \right] \right]^{0.5} |\nabla \tilde{c}| \quad \text{(ExtH}_2\text{FSC)} \tag{2.74}$$

$$\overline{\dot{\omega}} = C_{KPP} \rho_u \frac{S_t^2}{u'^2} \frac{\tilde{\epsilon}}{\tilde{k}} \tilde{c}(1 - \tilde{c}) \quad \text{(ExtH}_2\text{KPP)} \tag{2.85}$$

$$\overline{\dot{\omega}} = \rho_u \frac{S_t}{u_{\eta_K}} \frac{\tilde{\epsilon}}{\tilde{k}} \tilde{c}(1 - \tilde{c}) \quad \text{(ExtH}_2\text{LV)} \tag{3.14}$$

with

$$S_t = S_c + \frac{0.4}{\sqrt{Le^*}} u'^{0.8} S_c^{0.45} \alpha_u^{-0.25} l_t^{0.25} \tag{3.10}$$

The restated closures coupled with the proposed S_t (Eq. 3.10) are referred to as ExtH$_2$TFC, ExtH$_2$FSC, ExtH$_2$KPP and ExtH$_2$LV models. The model coefficient C_{KPP} in the ExtH$_2$KPP closure was calibrated to best match the experimental flame length of the mixture with 56.6% H$_2$ content. The resulting $C_{KPP} = 2.5$ (see Figure 5.5) was applied to all hydrogen contents.
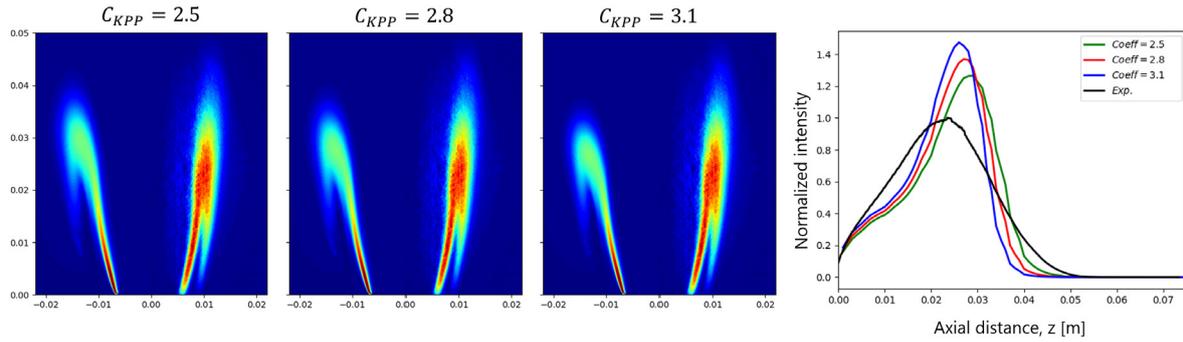
Figure 5.5: ExtH$_2$KPP model coefficient C_{KPP} adjustment against the experimental case with 56% H$_2$. $C_{KPP} = 2.5$ is the selected value, and the plot on the right shows the normalized axial HRR distributions against the experimental one.

The C1 mesh configuration is used for the CFD simulations with the ϵ based RSM model with non-equilibrium wall functions, and the stretch and heat loss are modelled as explained for RANS implementation in Section 3.1.. The HTC = 150 W/m^{2}K is assigned for the side wall heat transfer coefficient, and the Le^* is calculated from Eq. 2.79. The only difference in the model setup from the cases in the previous section is that the Aramco-Mech 1.3 [76] is used as the chemistry mechanism in S_c tabulation instead of the GRI-Mech 3.0 [22].

5.2.1. Mean flame shapes

In Figure 5.6, the normalized HRR contours at the mid-section plane obtained from the CFD computations are compared to the experimentally measured normalized Abel deconvoluted OH* chemiluminescence contours, and in Figure 5.7 axial HRR distributions are plotted.
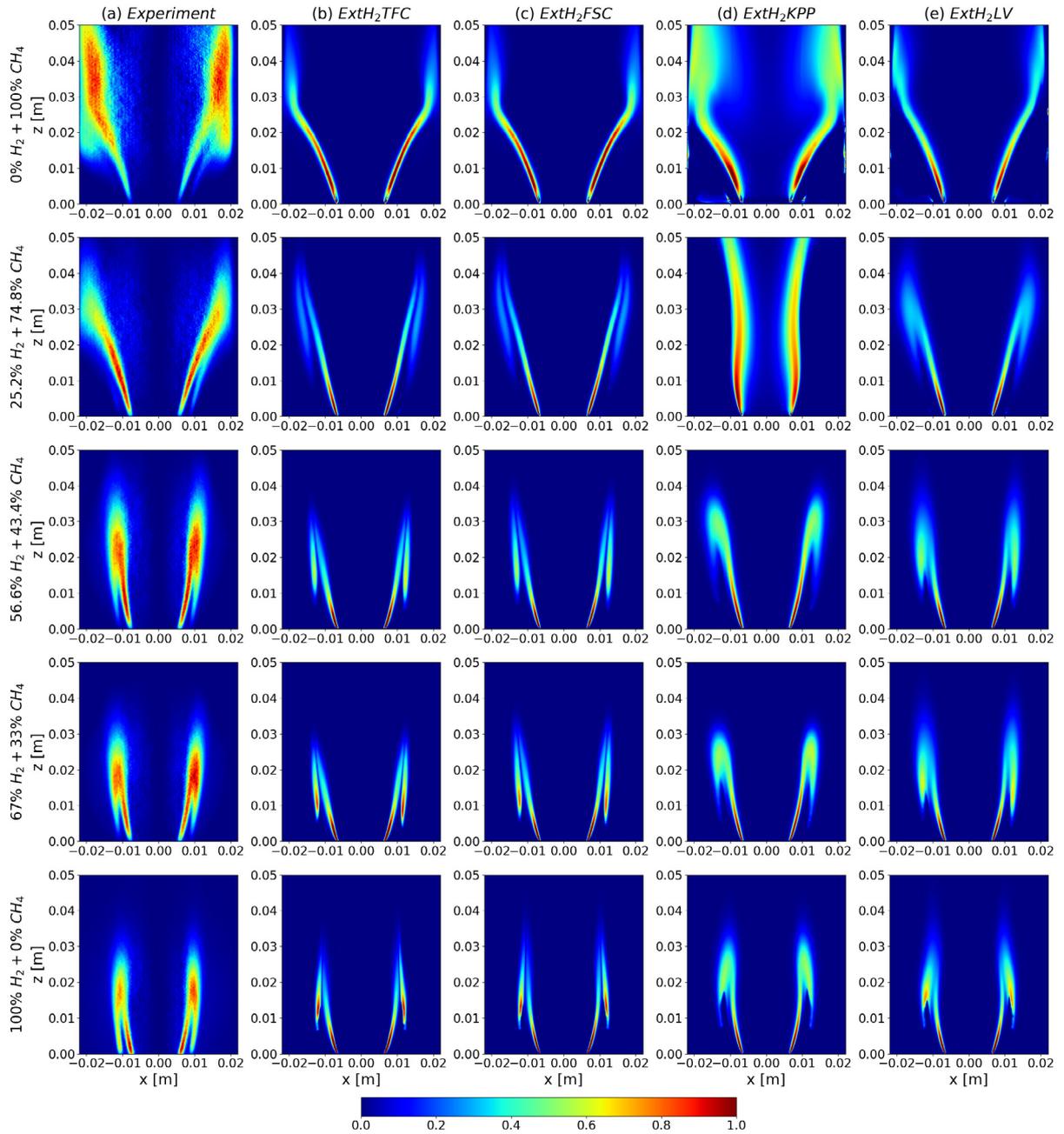
Figure 5.6: Heat release rate distributions from four different combustion models against experimental mean flame shapes: a) Abel deconvoluted OH* chemiluminescence images from experiments, b) ExtH$_2$TFC c) ExtH$_2$FSC d) ExtH$_2$KPP and e) ExtH$_2$LV models. Values are normalized with the maximum local intensity. Figure is taken from [57].

As observed from 5.6, all models (except ExtH$_2$KPP with 0% and 25.2% H$_2$) could correctly capture the mean flame shape and the transition from V to M flame (between 0% H$_2$ and 56.6% H$_2$) for all the cases listed in Table 4.1. This shows that the proposed S_t expression Eq. 3.10 works well for these experimental conditions.
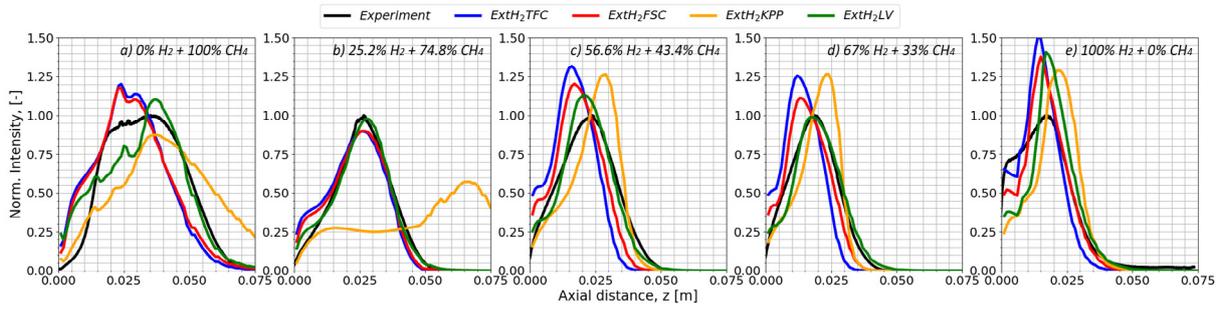
Figure 5.7: Axial heat release rate distributions from four different combustion models against experimental axial OH^* intensity distributions. Axial HRR curves are normalized provided that the areas under the curves are equal to those from experiments. Figure is taken from [57].

For the cases with 0% and 25.2% H_2 with the $ExtH_2KPP$ model, the flames could not stabilize, due to a low value of the calibration coefficient C_{KPP} in Eq. 2.85. In order to achieve stabilization, further calibration studies exclusively for these cases, are required.
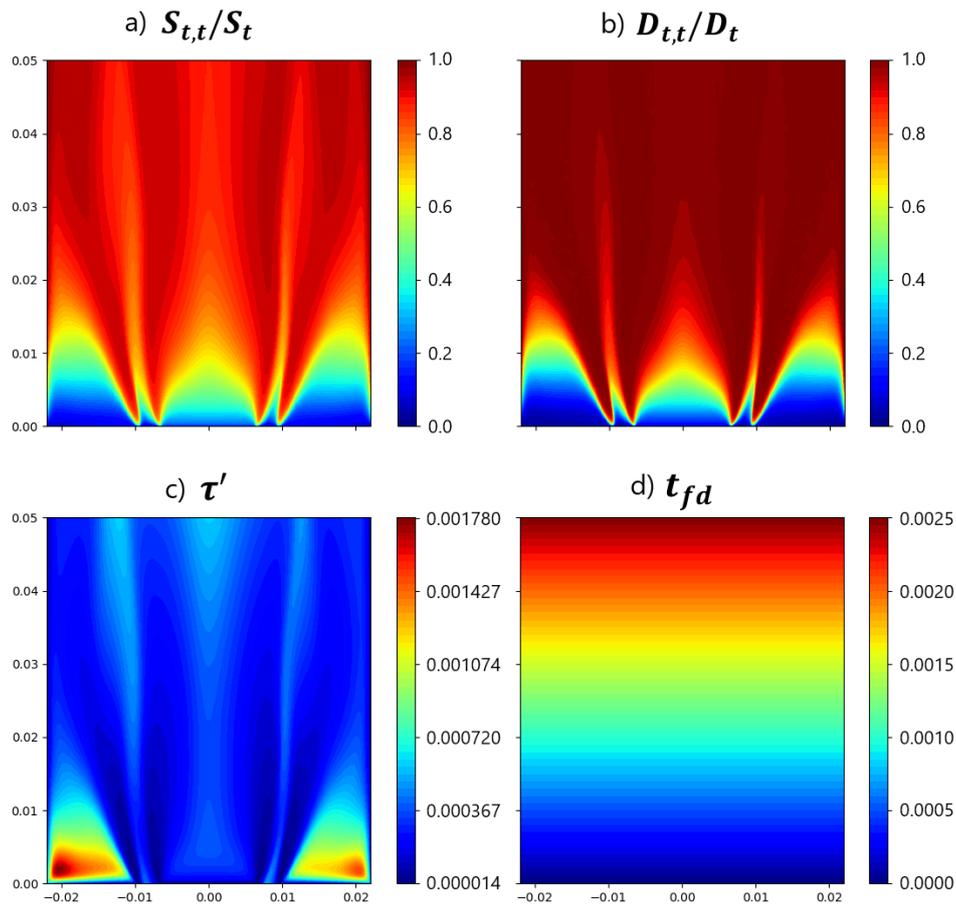
Figure 5.8: Flame brush thickness development terms of the FSC model. Contours are plotted for the case with 56.6% H_2 from the $ExtH_2FSC$ solution.

$ExtH_2TFC$ and $ExtH_2FSC$ models predict almost identical flame stabilization shapes (see

Figure 5.6 b) and c)) and axial HRR distributions (see Figure 5.7), demonstrating that for the cases investigated in this paper, the flame brush development terms described in Eq. 2.73 [46] do not significantly affect the predicted HRR distribution (see Figure 5.8). As observed from Figure 5.8 a) and b), the terms $S_{t,t}/S_t$ and $D_{t,t}/D_t$ reach unity very early at a region close to the flame attaching points to the bluff body. ExtH$_2$FSC predicts a bit longer flame lengths than ExtH$_2$TFC does, closer to experimental results, but this does not have an impact on the flame brush thickness prediction. Due to the gradient dependency $\overline{\dot{\omega}} \propto |\nabla\tilde{c}|$ in the closure, the ExtH$_2$TFC and ExtH$_2$FSC models, predict thinner flame brush thicknesses than those observed in the experiments. Instead, the ExtH$_2$KPP and ExtH$_2$LV models predict flame brush thickness distribution closer to the experiments with their $\overline{\dot{\omega}} \propto \tilde{c}(1 - \tilde{c})$ dependency. Additionally, ExtH$_2$TFC and ExtH$_2$FSC models predict almost zero heat release at the flame tip and maximum heat release at the flame attaching points to the wall (at $z = 0$) due to $\overline{\dot{\omega}} \propto |\nabla\tilde{c}|$ dependency.

All models show more substantial quenching than the experiments at the outer shear layers. The ExtH$_2$KPP model predicts even stronger flame quenching than all the other models. This is due to the different dependence of ExtH$_2$KPP reaction rate source term $\overline{\dot{\omega}}$ on the laminar consumption speed S_c (which is responsible for modelling of the quenching effects) compared to the other models: for ExtH$_2$KPP $\overline{\dot{\omega}} \propto S_t^2 \propto S_c^{0.9}$, while for the other models $\overline{\dot{\omega}} \propto S_t \propto S_c^{0.45}$.

5.2.2. Conclusions

Four different reaction rate closures derived as function of the proposed turbulent flame speed S_t (Eq. 3.10), namely; the ExtH$_2$TFC, the ExtH$_2$FSC, the ExtH$_2$KPP, and the ExtH$_2$LV were implemented in RANS context CFDs for assessing their mean flame shape and axial heat release rate predictions against experiments. The conclusions are listed as follows:

- The proposed S_t expression (Eq. 3.10) is able to reproduce the transition from V to M flame shapes for increasing hydrogen content for all the investigated closure models, except for the ExtH$_2$KPP model. For ExtH$_2$KPP model, case-specific model coefficient adjustment was needed.

- The closure models based on $\overline{\dot{\omega}} \propto \tilde{c}(1 - \tilde{c})$ predicts the flame brush thickness better than models based on $\overline{\dot{\omega}} \propto |\nabla\tilde{c}|$ proportionality. The flame brush development terms in the ExtH$_2$FSC model do not appreciably affect the calculated HRR distribution (see Figure 5.7).

- All the models show stronger quenching in the outer shear layer than the experiments.

- Among the models tested, the best match with the experimental data is obtained by the ExtH$_2$LV model.

5.3. EFFECT OF REACTION RATE CLOSURE IN LES CFD

In this section, LES implementations of the ExtH$_2$TFC and the ExtH$_2$LV models are presented. The LES version of the ExtH$_2$LV model has already been given in Chapter 3 with Eqs. 3.15 and 3.16 which are restated below. For the ExtH$_2$TFC model implementation in LES, the RANS version of the proposed turbulent flame speed S_t (Eq. 3.10) is replaced by its LES version $\overline{S}_{t,SGS}$ (Eq. 3.15) in the reaction rate closure $\overline{\dot{\omega}}$. However, different from the ExtH$_2$LV model, the coefficient of $S_{t,SGS}$ (Eq. 3.15) is recalibrated in order to stabilize the flame. As mentioned previously in the Introduction chapter, the recalibration of the coefficient with a parametric CFD study is a necessary step for the transformation of the TFC-based closures from RANS to LES (see also [39, 42, 43]). In this study, the recalibration was done only for the case with 0% H$_2$ by comparing the mean flame length prediction of the ExtH$_2$TFC-LES model with the experimental one, and the found value $A = 0.7$ was used in all the cases listed in Table 4.1.

$$S_{t,SGS} = S_c + \frac{A}{\sqrt{Le^*}} u_{SGS}'^{0.8} S_c^{0.45} \alpha_u^{-0.25} \Delta_{LES}^{0.25}, \quad A = \begin{cases} 0.4, & \text{for (ExtH}_2\text{LV-LES)} \\ 0.7, & \text{for (ExtH}_2\text{TFC-LES)} \end{cases} \tag{3.15}$$

$$\overline{\dot{\omega}} = \rho_u \frac{S_{t,SGS}}{u_{\eta K,SGS}} \frac{\sqrt{\tilde{k}_{SGS}}}{\Delta_{LES}} \tilde{c}(1 - \tilde{c}) \quad \text{(ExtH}_2\text{LV-LES)} \tag{3.16}$$

$$\overline{\dot{\omega}} = \rho_u S_{t,SGS} |\nabla \tilde{c}| \quad \text{(ExtH}_2\text{TFC-LES)} \tag{5.1}$$

The C2 mesh configuration is used for the simulations with the dynamic kinetic energy SGS model. Stretch and heat loss are modelled as explained for LES in Section 3.1. with the orientation factors $\widetilde{n_i n_j}$ in Eq. 3.4 evaluated following s1 approach in Table 3.2. For thermal wall boundary conditions, the temperature distributions obtained from previous RANS studies in C1 mesh configuration are imposed (see Section 4.2.). Aramco-Mech 1.3 [76] is used for the laminar consumption speed (S_c) tabulation. The simulations are carried out for all the mixtures listed in Table 4.1.

5.3.1. Mean flame shapes

Figure 5.9 shows on the left the normalized heat release rate (HRR) contours at the $x - z$ comparison plane and the axial HRR distributions from LES simulations in comparison with the Abel deconvoluted OH* chemiluminescence images and axial intensity plots from experiments. In Figure 5.9 d), the vertical dashed lines show the flame centroid heights $h_{cent.}$ which is calculated as follows:

$$h_{cent.} = \frac{\int z\overline{q}dz}{\int \overline{q}dz} \tag{5.2}$$

where z is the axial coordinate, $\overline{q}$ is the heat release rate integrated over planes normal to z axis.
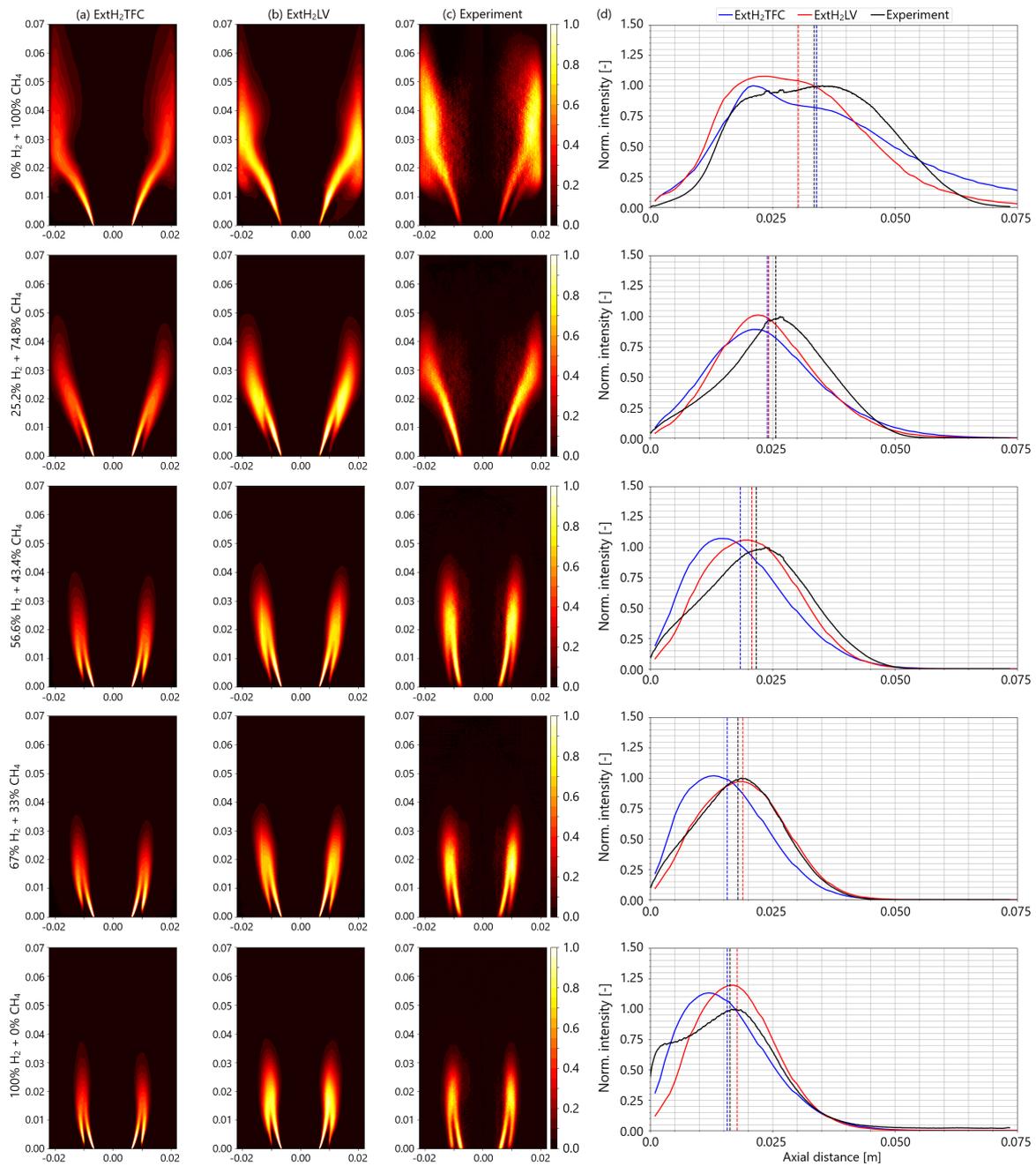
Figure 5.9: Heat release rate distributions from two different LES modelling approaches: a) ExtH$_2$TFC, b) ExtH$_2$LV, and c) Abel deconvoluted OH* chemiluminescence images from experiments. d) Normalized axial HRR distributions are shown in the right column. Contour values are normalized with the maximum local intensity. Axial HRR distributions from LES are normalized provided that the areas under the curves are equal to those from experiments. Figure is taken from [58].

As observed from Figure 5.9, both models could capture the correct flame stabilizations for all the cases (i.e. the V-flame to the M-flame shape transition). This is achieved due to the inclusion of stretch and heat loss effects in the formulations through the tabulated consumption

speed S_c in the proposed turbulent flame speed $S_{t,SGS}$ (Eq. 3.15). The importance of such effects on the correct stabilization of the flames was shown in Section 5.1..

Comparing Figure 5.9 a) vs c) for the mixtures, the ExtH$_2$TFC model slightly over-predicts the flame length for the case with 0% H$_2$, while under-predicts it for the other mixtures. On the other hand, the ExtH$_2$LV model predicts correct flame lengths for all the mixtures (see Figure 5.9 b) vs c)) except for the 0% H$_2$ case where it is under-predicted.

Figure 5.9 d) shows that the HRR distributions are better predicted with the ExtH$_2$LV model compared to ExtH$_2$TFC, as the peaks of the ExtH$_2$TFC model curves are biased towards the dump plane ($z = 0$ mm plane). The ExtH$_2$LV model curves show more uniform distributions similar to the experimental ones. This is also observed from contour plots, comparing Figure 5.9 a) and b), HRR contours intensify towards the dump plane (max HRR is reached at the dump plane) in the ExtH$_2$TFC model, while the ExtH$_2$LV model contours exhibit more uniform distributions which are also seen in the experiments. The main reason is that the ExtH$_2$TFC model is proportional to the gradient of progress variable $\bar{\omega} \propto |\nabla \tilde{c}|$ which takes its maximum value at the flame attaching points to the solid zones. On the other hand, the ExtH$_2$LV model also takes its maximum value at the flame attaching points due to its dependency on turbulent dissipation rate through $\bar{\omega} \propto \frac{\tilde{\epsilon}}{\tilde{k}} \approx \frac{\sqrt{\tilde{k}_{SGS}}}{\Delta_{LES}}$. However, the variation of this term from walls to the flow field is not strong as the gradient term $|\nabla \tilde{c}|$, and secondly, the variation of $\frac{\tilde{\epsilon}}{\tilde{k}} \approx \frac{\sqrt{\tilde{k}_{SGS}}}{\Delta_{LES}}$ term is further smoothed by the multiplication with the $\tilde{c}(1 - \tilde{c})$ term in the ExtH$_2$LV closure.

For the cases with 100% H$_2$, both models over-predict the outer shear layer quenching (see the last row of Figure 5.9 a), b) and c)). This causes discrepancies in the axial HRR distribution plots (see Figure 5.9 d)) in the region close to the dump plane ($z = 0$ mm). This over-quenching at the outer shear layer for the case with 100% H$_2$ was also observed in the previous RANS calculations (see Sections 5.1., and 5.2.). To elaborate on this behavior, heat loss parameter β, total stretch κ, and interpolated consumption speed S_c contours are plotted in Figure 5.10 together with the tabulated laminar consumption speed.

The over-quenched region for the case with 100% H$_2$ is indicated with black circles in the heat loss, stretch, and consumption speed contour plots in Figure 5.10 a), b) and c). The corresponding region in the consumption speed tabulation plot is also indicated with a black rectangle in Figure 5.10 d). As can be observed, calculated stretch κ and beta heat loss parameter β values correspond to the region where the steep gradients occur in the tabulated S_c curves, and causes abrupt extinctions.

Comparing the flame centroid heights $h_{cent.}$ in Figure 5.11, despite small deviations, both models could correctly capture the center of HRR distributions for all the mixtures, which is important in terms of time delay predictions under acoustically forced conditions.

5.3.2. Conclusions

Two closure models for the reaction rate source term; the ExtH$_2$TFC and the ExtH$_2$LV were validated in LES context CFD against experiments, for mean flame shape and axial heat release rate predictions. The conclusions are listed as follows:

- The inclusion of stretch, heat loss, and Lewis number effects in their formulations (via
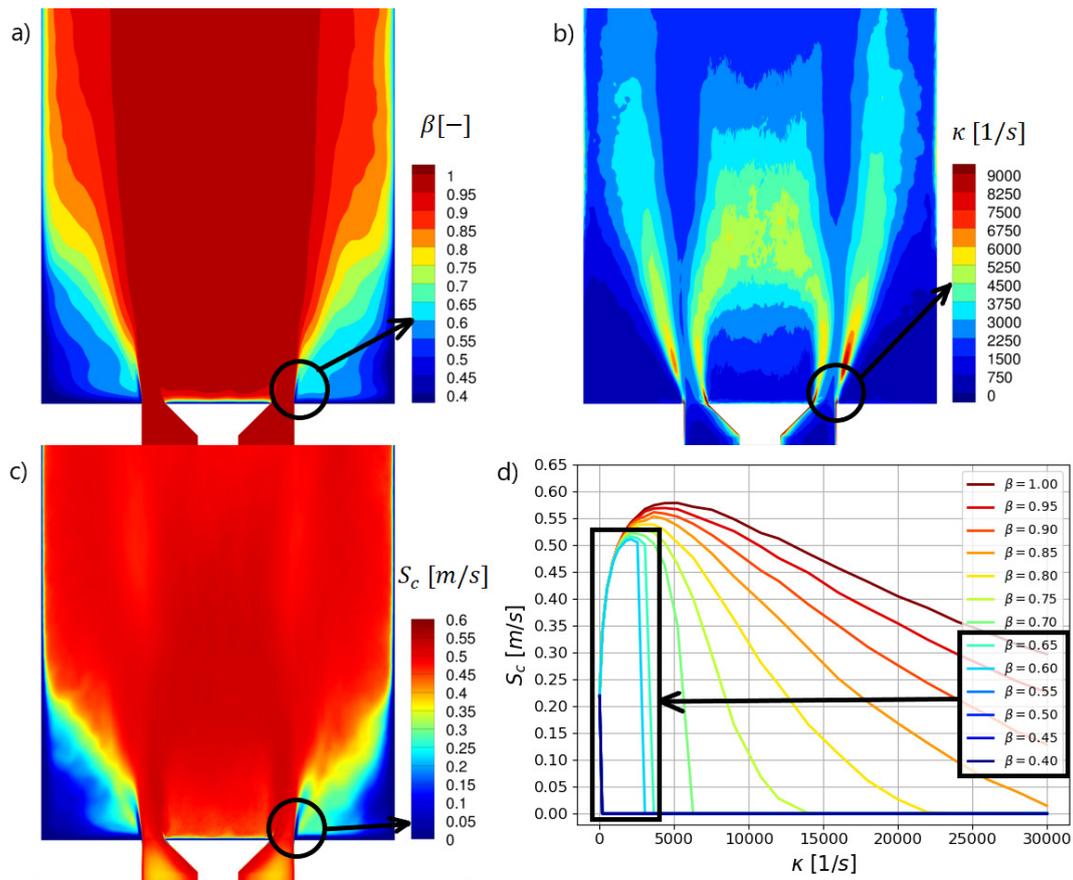
Figure 5.10: a) Mean β heat loss parameter contours, b) mean total stretch κ contours, c) mean interpolated laminar consumption speed S_c contours and d) the tabulated laminar consumption speed S_c plot for the case with 100% H_2 from the ExtH$_2$LV-LES simulation. Figure is taken from [58].
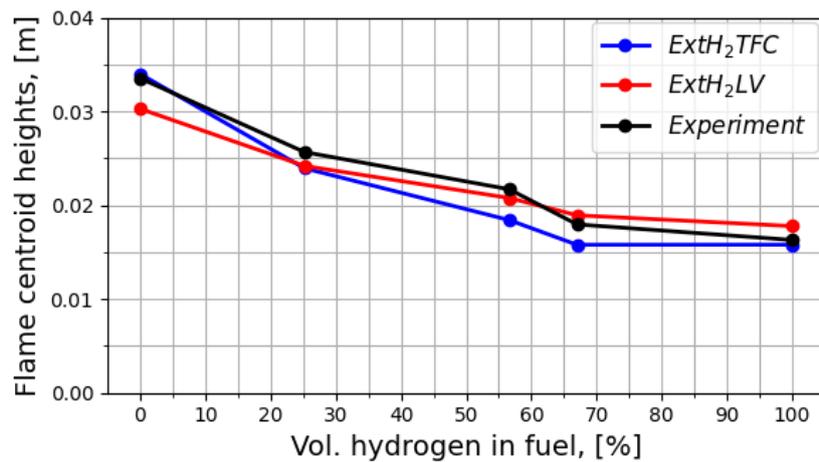
Figure 5.11: Flame centroid height variation against volumetric H_2 content in the fuel mixture. Figure is taken from [58].

the proposed S_t relation, Eq. 3.10) allows both models to correctly predict the flame stabilizations and the V to M flame shape transition as the H_2 content in the mixture increases. The ExtH$_2$LV shows improvements over the ExtH$_2$TFC in the mean flame shape and axial HRR distribution predictions.

- The ExtH$_2$LV model predicts the flame shapes in very good agreement with experiments in terms of flame shape, axial HRR distribution, and flame length. With slight deviations in terms of HRR distribution along the flame, the ExtH$_2$TFC model also predicts the flame stabilizations in good agreement with experiments. Compared to its RANS implementation (see Sections 5.1. and 5.2.), the mean flame brush thickness predictions are improved in the LES implementation of the ExtH$_2$TFC model.

- In the proposed ExtH$_2$LV closure as well as in the ExtH$_2$TFC closure, stretch and heat loss modelling is responsible for the mean flame shape and stabilization, while the model coefficient A, together with the effective Lewis number Le^* is responsible for the flame length ($\overline{\dot{\omega}} \propto S_{t,SGS} \propto \frac{A}{\sqrt{Le^*}}$) prediction.

5.4. RANS/SAS/LES IMPLEMENTATIONS OF THE PROPOSED CLOSURE

In this section, the proposed modelling closure is implemented in RANS, SAS and LES context CFDs. Its applicability with different turbulence modeling approaches is shown by the consistent results obtained from RANS, SAS, and LES, and the agreements with the experiments. The sensitivities of the flame shape predictions to different stretch modelling approaches and heat loss levels are also investigated.

For RANS and SAS simulations, Eq. 3.14, and for LES simulations Eq. 3.16 are used for closing the reaction rate source term $\overline{\dot{\omega}}$. These closures are restated below:

$$\overline{\dot{\omega}} = \rho_u \frac{S_t}{u_{\eta_K}} \frac{\tilde{\epsilon}}{\tilde{k}} \tilde{c}(1 - \tilde{c}) \quad \text{(ExtH}_2\text{LV-RANS/SAS)} \tag{3.14}$$

$$S_t = S_c + \frac{0.4}{\sqrt{Le^*}} u'^{0.8} S_c^{0.45} \alpha_u^{-0.25} l_t^{0.25} \quad (S_t \text{ for RANS/SAS}) \tag{3.10}$$

and

$$\overline{\dot{\omega}} = \rho_u \frac{S_{t,SGS}}{u_{\eta_{K,SGS}}} \frac{\sqrt{\tilde{k}_{SGS}}}{\Delta_{LES}} \tilde{c}(1 - \tilde{c}) \quad \text{(ExtH}_2\text{LV-LES)} \tag{3.16}$$

$$S_{t,SGS} = S_c + \frac{0.4}{\sqrt{Le^*}} u'^{0.8}_{SGS} S_c^{0.45} \alpha_u^{-0.25} \Delta_{LES}^{0.25}, \quad (S_t \text{ for LES}) \tag{3.15}$$

In this section, all the cases are carried out by solving conjugate heat transfer, and accordingly, the C1, C3 and C4 mesh configurations (see Figure 4.3) are used for RANS, LES and SAS implementations, respectively. For the thermal boundary conditions, HTC $= 8.6$ W/m^{2}K and HTC $= 100$ W/m^{2}K are assigned to the back and side walls of the combustion chamber

(BC 4 and BC 5 in Figure 4.4), respectively, with $T_\infty = 296$ K assigned for the ambient temperature. Note that in simulations presented in previous sections (see Sections 5.1., and 5.2.) an HTC = 150 W/m^{2}K was set for the side wall thermal boundary condition for RANS cases, and the temperature distributions obtained from the RANS cases were imposed in the LES simulations (see Section 5.3.). However, for the current LES cases with the C3 mesh configuration, an HTC = 150 W/m^{2}K value was found too high, and the best match with experiments were obtained with the HTC = 100 W/m^{2}K.

The ϵ and ω based RSM turbulence models are selected for RANS and SAS simulations, respectively, and the dynamic kinetic energy SGS model is selected for the LES simulations. Further numerical details are set up as explained in Section 4.2..

The stretch and heat loss are modelled as explained in Section 3.1.. The orientation factors ($n_i\tilde{n}_j$ in Eq. 3.4) which are needed to evaluate the mean/resolved flow contribution to stretch, are modelled following Eq. 3.8 in RANS. For LES implementation, they are modelled following both s1 and s2 in Table 3.2, and these two implementations are referred to as LES-s1 and LES-s2 in results and discussion. For SAS, they are evaluated in three different ways such as; following Eq. 3.8 as in RANS, and following s1 and s2 in Table 3.2 as in LES, accordingly, these are referred to as SAS, SAS-s1 and SAS-s2, respectively, in results and discussion.

5.4.1. Mean flame shapes

Figure 5.12 shows the calculated mean flame shapes and compares them with those measured in the experiments. As observed from the flame shapes predicted by CFDs (Figure 5.12 a) to f) against experiments Figure 5.12 g)), it can be concluded that, despite some quantitative differences, for all the turbulent flow models, the proposed modelling closure is able to qualitatively predict the transition from the V to M flame shape and the flame shortening effect (while the hydrogen content in the fuel increases).

Comparing the spatial distribution of the heat release, SAS and LES produced a better prediction of the heat release distribution in the flame brush thickness compared to RANS. The flame shapes and lengths are well predicted (see Figure 5.12 a) vs f)). For the pure methane case, the model captures the quenching effects at the outer shear layer which produces a V flame shape as in the experiment. While this quenching effect is important for the pure methane flame; in the pure hydrogen case, the quenching at the outer shear layer is significantly over-predicted in RANS (the last row in Figure 8 a)), as experiments showed a strong flame stabilization in the outer flame. Looking at the flame angle, SAS approaches cannot reproduce similar flame angles seen in the experiments for the cases with 56.6% and 67% H$_2$. LES and RANS reproduce well the flame angle for both cases. It is observed that the SAS cases at those H$_2$ % produce a larger inner recirculation zone (IRZ) as discussed further in Figure 5.13.

Comparing the impact of different resolved stretch modelling approaches (SAS, SAS-s1, SAS-s2, LES-s1 and LES-s2 in Figure 5.12 e) and f)), the flame shapes are very similar between cases with slight differences in flame lengths. The SAS-s2 and LES-s2 cases predict a higher level of a stretch, especially at the outer shear layer (see also Section 5.4.2.). The increase in stretch produces higher quenching in the outer shear layer in SAS-s2 and LES-s2. For the pure methane flame, where a stronger flame-wall interaction is present compared to the other
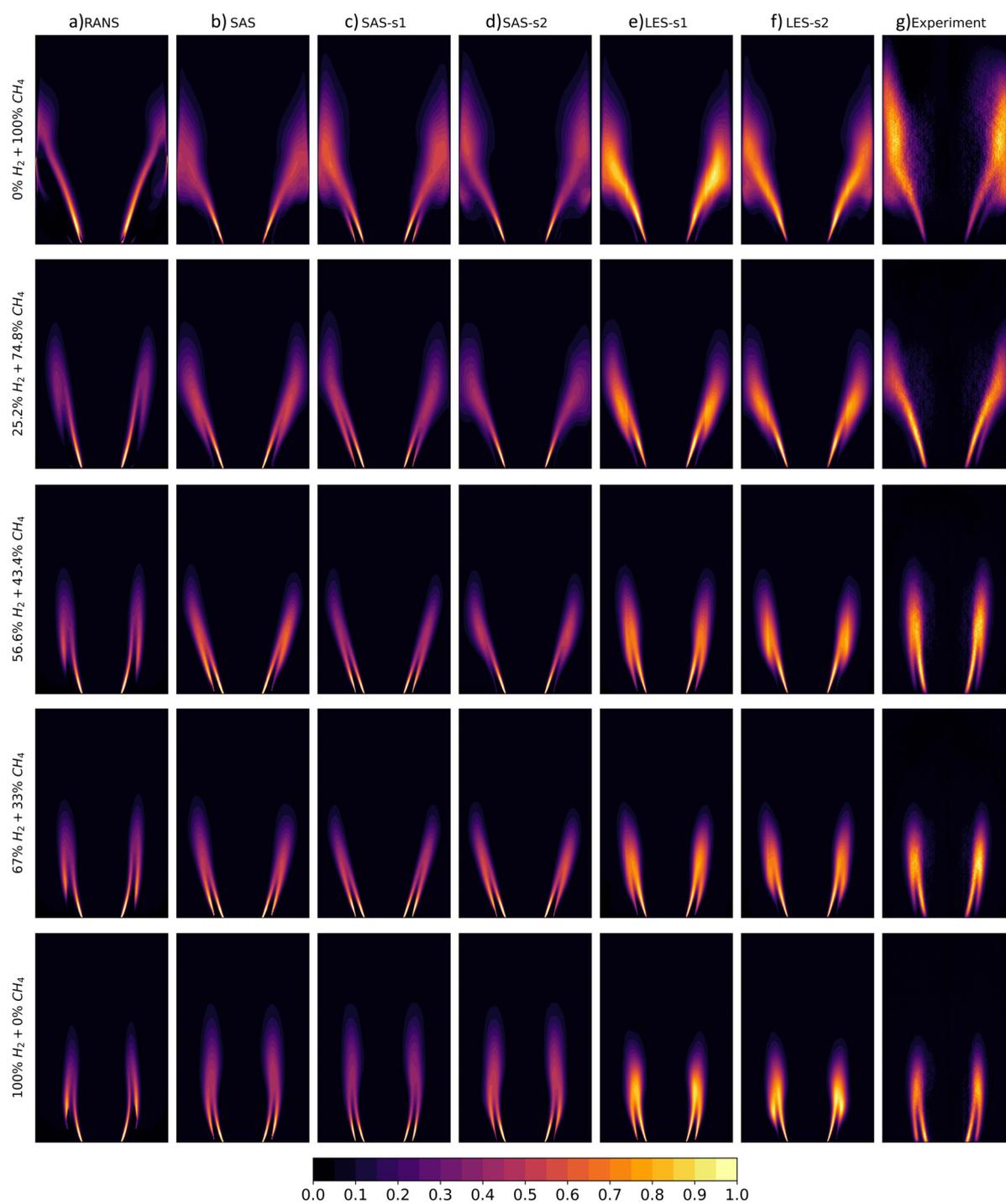
Figure 5.12: Mean flame shapes predicted with a) RANS, b) SAS, c) SAS-s1, d) SAS-s2, e) LES-s1, f) LES-s2 setup, and g) normalized Abel deconvoluted OH* chemiluminescence intensities measured in the experiments.
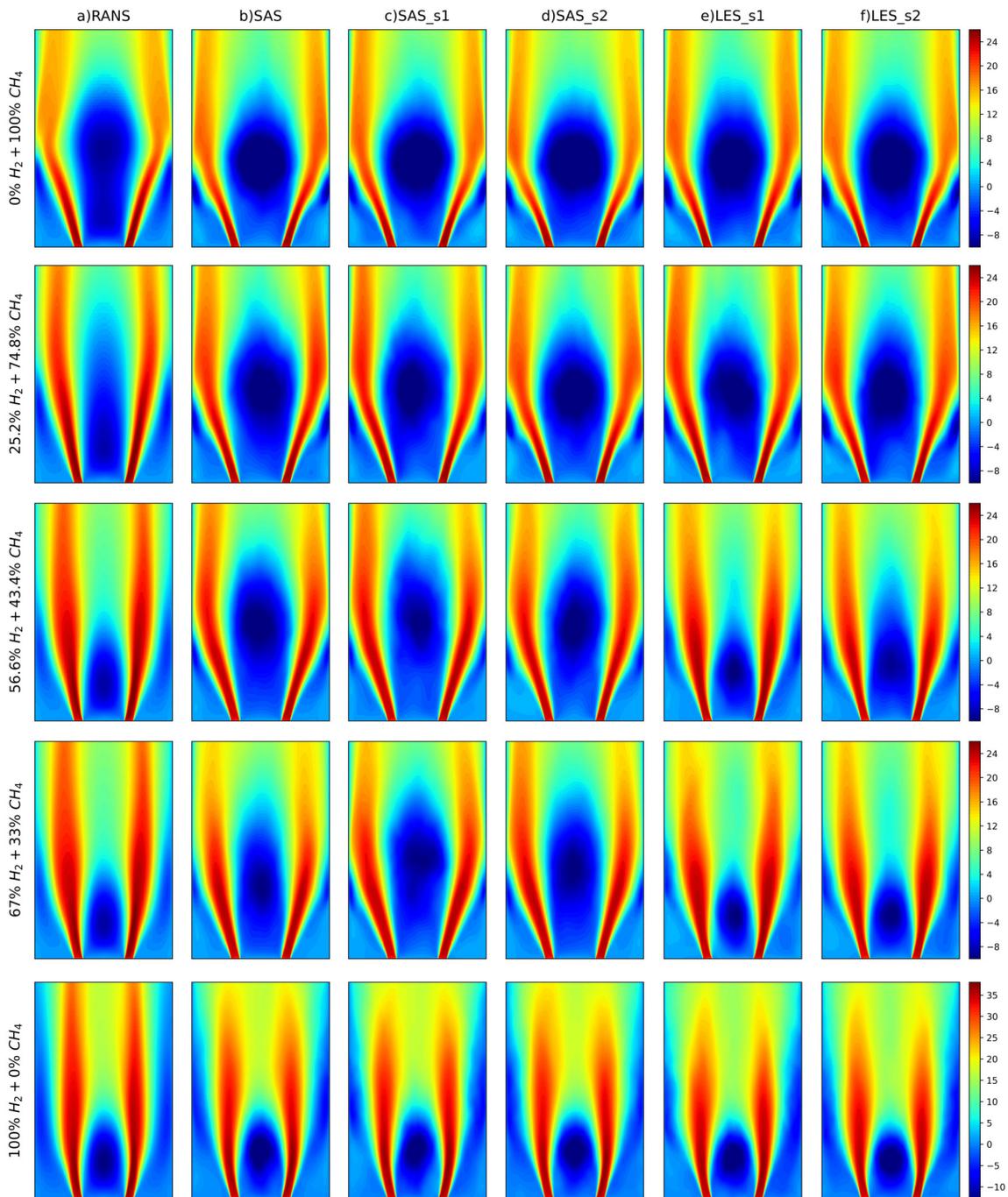
Figure 5.13: Axial velocity [m/s] contours predicted with a) RANS, b) SAS, c) SAS-s1, d) SAS-s2, e) LES-s1 and f) LES-s2.

cases, SAS-s2 and LES-s2 predict a heat release distribution and flame length in slightly better agreement with the experiment. For this hydrogen content, SAS-s1 predicts flame stabilization in the outer shear layer, different from the others (see the first row of Figure 5.12 c)).

Comparing the performance in the M-flames with H_2 content, the higher stretch in the outer

shear layer produces stronger quenching with SAS-s2 and LES-s2, which is not seen in the experiments. In LES-s2 the level of quenching is higher compared to SAS-s2 (see Figure 5.12 d) and f)). For the cases with H_2 content, LES-s1 produces a better agreement on the spatial distribution of heat release and flame stabilization than LES-s2. On the contrary, SAS and SAS-s2 produce a better agreement with experiments compared to SAS-s1, as SAS-s1 predicts stronger flame stabilizations than the experiments at the outer shear layer.

To show the impact of flame stabilization on the velocity field, Figure 5.13 plots the axial velocity contours predicted with different turbulence modelling approaches. The size of the IRZ is influenced by the flame topology, having a larger IRZ in the V flame topology. As the flame stabilization gets a narrower shape (i.e. V to M flame transition), the IRZ gets smaller and moves upstream. In SAS approaches, for the cases with 56.6% and 67% H_2, the IRZs are bigger than those predicted by LES approaches and RANS, which is also seen as a flame stabilization with a more open angle.
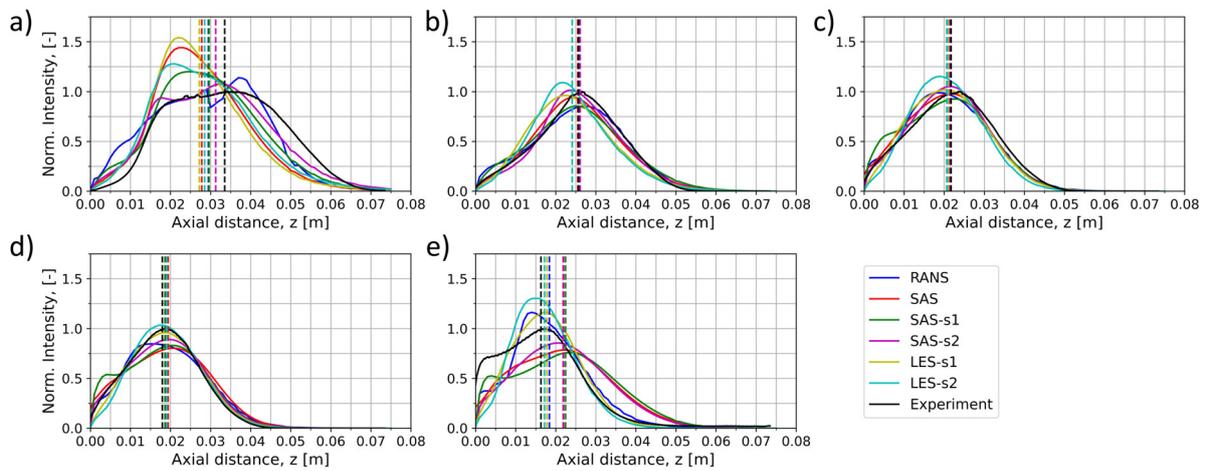
Figure 5.14: Normalized axial heat release rate distributions predicted with RANS, SAS, SAS-s1, SAS-s2, LES-s1 and LES-s2 approaches against normalized OH* chemiluminescence intensity plots for a) 0% H_2 + 100% CH_4, b) 25.2% H_2 + 74.8% CH_4, c) 56.6% H_2 + 43.4% CH_4, d) 67% H_2 + 33% CH_4, e) 100% H_2 + 0% CH_4. CFD distributions are scaled provided that the area under the axial HRR curves is equal to those from experiments. Vertical dashed lines show the flame centroid heights $h_{cent.}$.

The normalized axial heat release rate distributions are plotted in Figure 5.14, which is important to estimate the performance of the combustion model as it provides a measure for a quantitative comparison with experiments. As observed from Figure 5.14, despite small discrepancies, quite good agreements are achieved for the cases with 25.2%, 56.6% and 67% H_2 contents, but for the cases with 0% and 100% H_2, the discrepancies are significant. This can be observed also from the flame centroid heights, as they are distributed in a wide gap for the pure methane and pure hydrogen flames, while for the other cases, they are accumulated in a narrow gap. Another observation is that the flame centroid heights, calculated from CFDs, tend to be shorter for the pure methane flame and to be longer for the pure hydrogen flame, compared to the experiments.

Mean flame shape results (Figure 5.12) show that the HRR distribution over the flame, differs depending on the model's implementation with different turbulence modelling approaches.

The HRR is more uniformly distributed over the flame in LES while it intensifies towards the dump plane ($z = 0$) in RANS and SAS implementations. This is the natural consequence of the proposed closure for $\overline{\dot{\omega}}$, as it is a function of $\tilde{\epsilon}/\tilde{k}$ term in RANS and SAS implementations (see Eq. 3.14), which takes its maximum value ($\tilde{\epsilon}$ increases, $\tilde{k}$ decreases) over the wall boundaries. On the other hand, in LES implementation, the equivalent term is $\sqrt{\tilde{k}_{SGS}}/\Delta_{LES}$, where both $\tilde{k}_{SGS}$ and Δ_{LES} decrease towards the wall boundaries.

Giving insight to this phenomenon, $\tilde{\epsilon}/\tilde{k}$ and $\sqrt{\tilde{k}_{SGS}}/\Delta_{LES}$ terms are plotted in Figure 5.15 for RANS, SAS and LES-s1, respectively. As observed from Figure 5.15, $\tilde{\epsilon}/\tilde{k}$ term in RANS and SAS, and $\sqrt{\tilde{k}_{SGS}}/\Delta_{LES}$ term in LES take high values at the early development regions of the inner and outer shear layers close to the dump plane. Similar to observations in the mean flame shape plots, there is a steep gradient in $\tilde{\epsilon}/\tilde{k}$ term in RANS and SAS implementations towards the dump plane while this increase is not so marked for the $\sqrt{\tilde{k}_{SGS}}/\Delta_{LES}$ term in LES implementation. This allows LES to predict more uniformly distributed HRR over the flame.
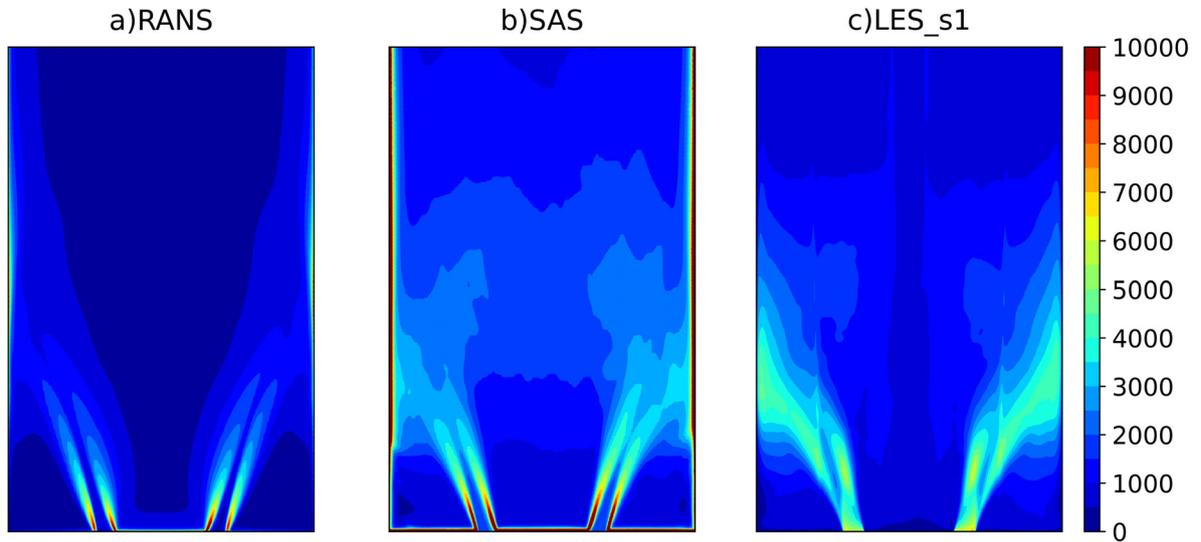
Figure 5.15: $\tilde{\epsilon}/\tilde{k}$ [1/s] contours obtained with a) RANS, b) SAS and c) $\sqrt{\tilde{k}_{SGS}}/\Delta_{LES}$ [1/s] contours obtained with LES-s1 setup. Contours are plotted for the case with 0% H$_2$.

In Figure 5.15, the red contour layer (indicating maximum value) observed in SAS but not in RANS along the wall boundaries is due to the implementation of wall functions in RANS calculations owing to the ϵ based RSM turbulence model, which applies log-law to the wall boundaries [50] without having a laminar sublayer. On the other hand, ω based RSM SAS turbulence model applies wall resolving approach when the y^+ value allows, in which the laminar sublayer is resolved, where the dissipation rate goes infinity, and turbulent kinetic energy goes to zero.

Due to abovementioned turbulence dependencies of the proposed combustion model near wall boundaries, for the cases where the flame interacts with walls, the proposed closure $\overline{\dot{\omega}} \propto \tilde{\epsilon}/\tilde{k}$ can cause numerical ignition problem at the wall boundaries in RANS simulations (especially in unsteady RANS (URANS)). This does not cause a problem in SAS and LES, as their scale-dependent formulations do not let the artificially ignited regions grow. However, in

URANS when the numerical ignition occurs over the wall boundaries depending on local turbulence, stretch, and heat loss levels, it cannot break into smaller scales due to its formulation, instead starts growing locally and it can end up with unrealistic flame stabilizations. In RANS, and in the URANS cases without flame wall interactions, this problem has not been seen. However, for such URANS cases where flame wall interactions are present, it is advised to couple the model with a suitable wall quenching model like in [84].

5.4.2. Combined effect of stretch and heat loss

To investigate how the stretch and heat loss change between the different turbulence modelling approaches Figure 5.16 is plotted for the pure methane flame, where the mean flame shape (normalized $\bar{\omega}$), total stretch κ, and β heat loss parameter contours are plotted with axial wall temperature distributions for RANS, SAS, LES-s1 and LES-s2 setups.
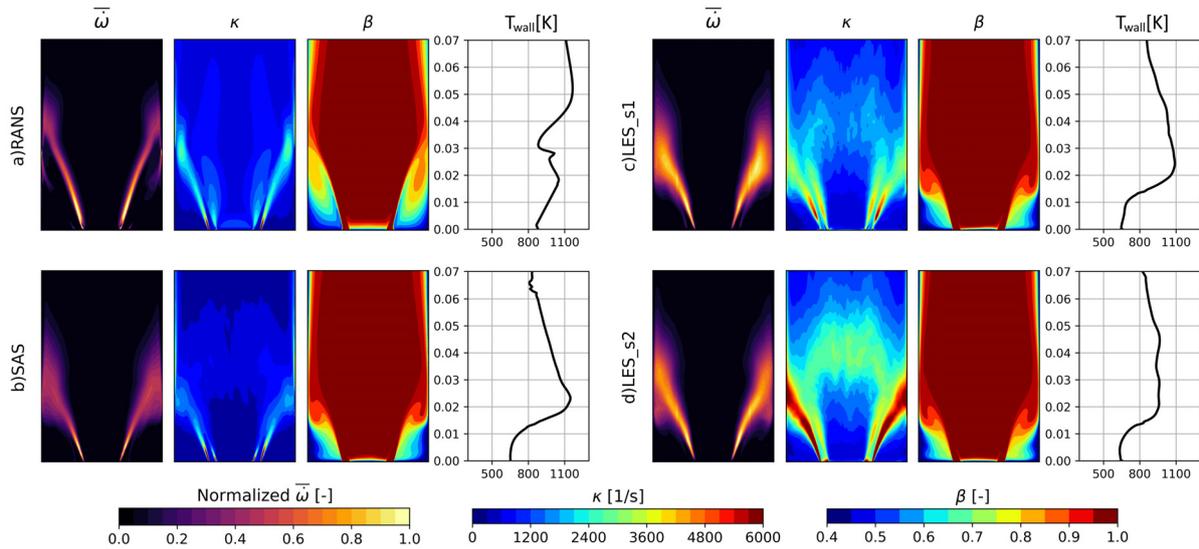
Figure 5.16: Mean contour plots of normalized reaction rate source term $\bar{\omega}$, total stretch κ, heat loss parameter β and axial wall temperature distribution from a) RANS setup, b) SAS setup, c) LES-s1 setup, d) LES-s2 setup for the case with 0% H_2. In axial wall temperature plots horizontal axis refers to temperature scale [K], vertical axis refers to axial distance scale [m].

Comparing β contours in Figure 5.16, scale resolving approaches (SAS, LES-s1 and LES-s2) have almost the same heat loss β distributions (see Figure 5.16 b), c) and d)). RANS has a very similar distribution but with lower β values at the outer recirculation zone (Figure 5.16 a)). In comparison of total stretch κ contours, LES produces higher values than RANS and SAS, and SAS produces the lowest values amongst all approaches. Note that, SAS-s1 and SAS-s2 produced very similar stretch and heat loss distributions as in LES-s1 and LES-s2, respectively.

LES-s2 produces higher values of total stretch than LES-s1 due to the additional term in the orientation factors to calculate stretch in LES-s2 (see Table 3.2). This causes higher quenching at the outer shear layer for the flames with hydrogen content (see Figure 5.12 d)). For the pure

methane flame, this results in longer flame prediction compared to LES-s1 and flame stabilization at the outer recirculation zone (ORZ). Flame stabilization at the ORZ is also seen in RANS but not seen in SAS and LES-s1 (see the $\overline{\dot{\omega}}$ contours in Figure 5.16).

For the pure methane flame, calculated high stretch by LES-s2 at the intersection of the outer shear layer with the side wall (see the κ contour in Figure 5.16 d)), decreases the reaction rate and the flame expands towards ORZ by the driving effect of recirculating velocity (see the $\overline{\dot{\omega}}$ contour in Figure 5.16 d)). Similarly, higher heat loss (lower β at the ORZ) in RANS results in the stabilization of the flame at the ORZ (see the $\overline{\dot{\omega}}$ contour in Figure 5.16 a)). In LES-s1 and SAS, moderate stretch and heat loss values at the ORZ do not decrease the reaction rate as strongly as in the LES-s2 and RANS, so the flame cannot be driven by the recirculating flow (see the $\overline{\dot{\omega}}$ contour in Figure 5.16 b) and c)). This ORZ flame stabilization is presented with a magnified view in Figure 5.17 for LES-s1 and LES-s2 setups.
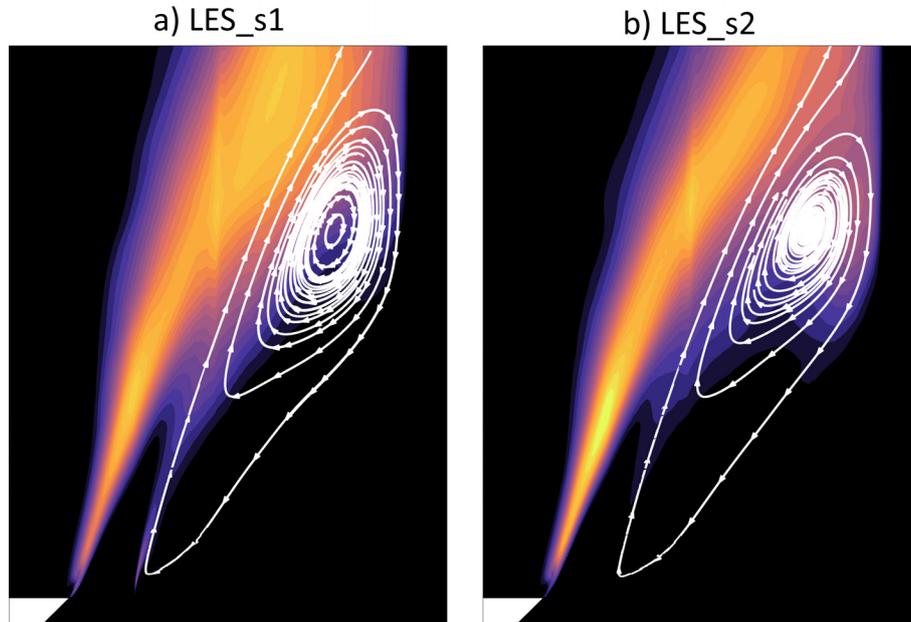
Figure 5.17: Magnified view of ORZ from Figure 5.12 with streamlines for 0% H_2 case for a) LES-s1 setup, b) LES-s2 setup.

ORZ flame stabilization affects the side wall temperature distribution. $T_{wall}(z)$ plots in Figure 5.16 show that temperature is distributed more uniformly in the RANS and LES-s2 where the ORZ flame stabilization occurs, while it makes a peak and then decreases in SAS and LES-s1.

5.4.3. Sensitivities to heat loss

The sensitivities of the mean flame shapes to different heat loss levels are investigated by increasing the side wall HTC from 100 to 150 W/m^{2}K for the RANS, LES-s1 and LES-s2 cases. In Figures 5.18 and 5.19, mean flame shapes and the axial HRR distributions for the cases with 0% and 56.6% H_2 are plotted for the two heat loss levels.
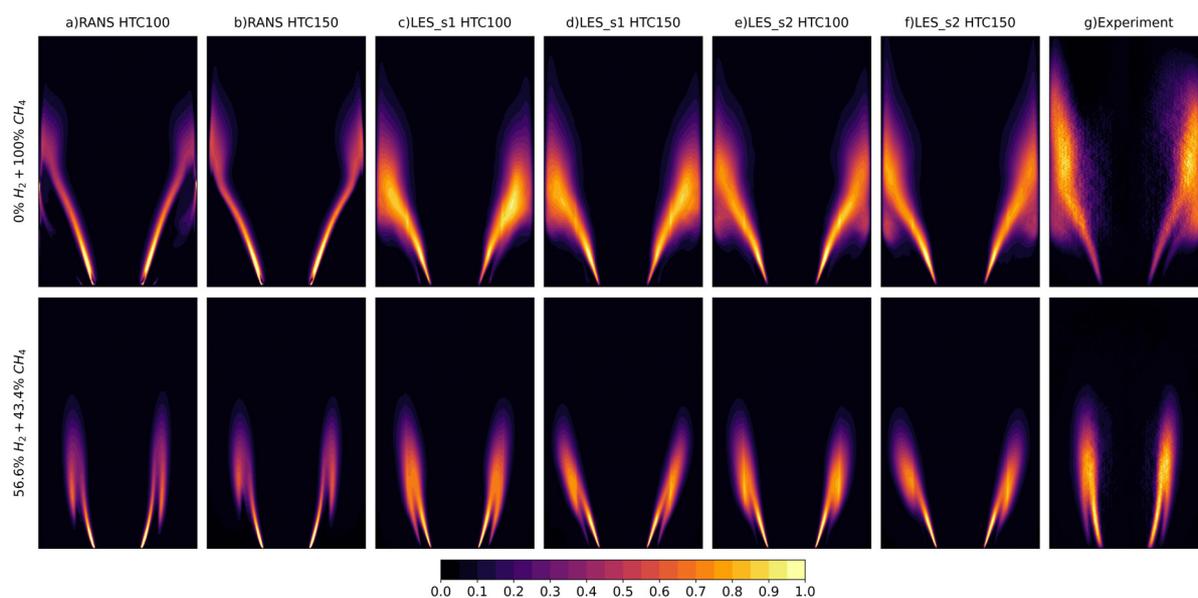
Figure 5.18: Effect of heat loss on flame stabilization a), c) and e) are predicted with RANS, LES-s1 and LES-s2 setups, respectively with side wall HTC = 100 W/m^{2}K, b), d) and f) are predicted with RANS, LES-s1 and LES-s2 setups, respectively with side wall HTC = 150 W/m^{2}K.
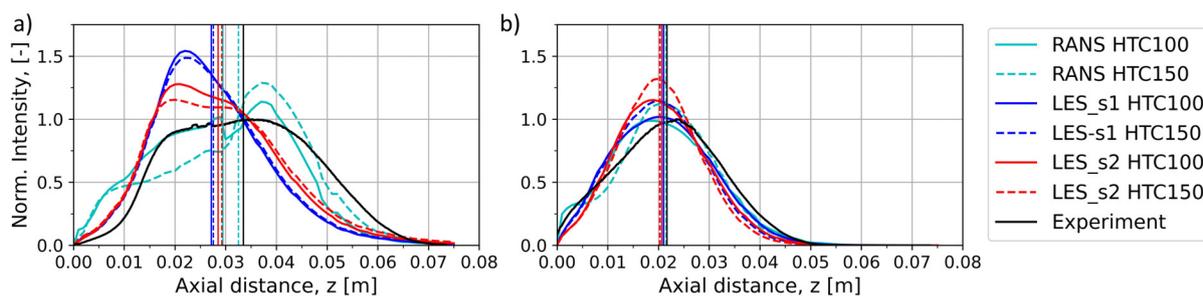
Figure 5.19: Effect of heat loss on axial HRR distribution, a) 0% H$_2$ + 100% CH$_4$, b) 56.6% H$_2$ + 43.4% CH$_4$. Vertical lines show the flame centroid heights $h_{cent.}$.

Comparing Figure 5.18 a) against b), increasing heat loss completely quenches the flame stabilization at the ORZ for the pure methane flame in RANS. For the case with 56.6% H$_2$ the flame shape and length remain the same, but the quenching at the outer shear layer becomes more pronounced. In LES-s1 and LES-s2, increasing heat loss has almost no effect on the flame shape and length for the pure methane flame (see the first row in Figure 5.18 c) vs d), and Figure 5.18 e) vs f)) but for the case with 56.6% H$_2$, it causes wider flame stabilization (the angle between shear layers increases), and the quenching at the outer shear layer becomes more pronounced (see the second row in Figure 5.18 c) vs d), and Figure 5.18 e) vs f)).

As observed from Figure 5.19, major variations due to heat loss increment are seen on the pure methane flame in RANS (see Figure 5.19 a) RANS HTC100 vs RANS HTC150). For the pure methane RANS flame, the complete flame quenching at the ORZ (see the first row in Figure 5.18 a) vs b)) results in a severe decrement of the axial HRR distribution first, up to $z = 0.03$ m, and a severe increment beyond this point in the axial distribution plots (see

Figure 5.19 a)). This also causes a significant shift of $h_{cent.}$, extending the flame length. For the other cases in axial HRR distributions, small variations are seen with a slight shift in the flame centroid heights $h_{cent.}$.

5.4.4. Conclusions

The proposed ExtH$_2$LV model was validated for mean flame shape predictions of atmospheric bluff-body stabilized turbulent premixed CH$_4$/H$_2$/air flame experiments ranging from pure methane to pure hydrogen under lean mixture conditions in RANS, SAS and LES contexts. The conclusions are listed as follows:

- The model captures the correct flame stabilizations and the V to M-flame transition with all the turbulence modelling approaches.

- The model does not require an adjustment in the model coefficient for the translation between turbulent modelling approaches, differently from TFC-based modelling approaches (see Section 5.3. and also [39, 42, 43]).

- Good agreements with experiments, and consistent predictions between RANS, SAS and LES implementations are accomplished. In SAS implementations, for the cases with 56.6% and 67% H$_2$ contents, the model predicts wider flame opening angles than experiments, and for the pure hydrogen case, the flame angle is predicted correctly but the flame length is overpredicted.

- Stretch modelling differences in RANS, SAS and LES contexts were outlined and their effects on flame stabilization were discussed. In LES context two, and in SAS context three different resolved stretch modelling approaches were utilized and their effects on flame stabilization were discussed. The main impact is observed in the pure methane case where strong flame wall interactions are present. In this case, the different levels of calculated stretch result in different predictions of the flame shape and length. For the other cases, the effect is seen only at the quenching level at the outer shear layer, however, this does not influence the flame length predictions.

- Flame stabilization sensitivities to heat loss were investigated under two different heat loss levels in RANS and LES contexts. It is observed that the higher heat loss causes higher quenching at the outer shear layer and results in wider flame stabilization.

FLAME DYNAMICS PREDICTIONS

In this chapter, the dynamic performance of the proposed modelling closure (ExtH$_2$LV) is tested by extracting the flame transfer functions (FTFs) from SAS and LES simulations and comparing them against the experimental measurements.

To compute the FTF, the flame must be forced either by using a harmonic or a broadband excitation technique. The former requires performing a simulation for each discrete forcing frequency and covering the whole frequency range of interest requires a large number of simulations. Instead, the latter approach, which is used in this study, allows to perform only one broadband excited simulation. The FTF can then be extracted by means of CFD system identification (SI) techniques first proposed by Polifke et al. [85], then used successfully in many other studies [8, 23, 24, 58, 86–88] in the literature. For the simulations presented in this paper, the *TFDtools* [89] libraries are used for the creation of broadband excitation signals and extraction of FTFs.

In the following, first, the CFD-SI methodology is outlined, then the computed FTFs with the proposed modelling approach are compared with the experiments.

6.1. CFD-SI TECHNIQUE

The theoretical background of the CFD-SI technique outlined here can be found in detail in [85, 90]. First, the CFD simulation is forced by a broadband excitation signal at the inlet whose spectrum covers the whole range of frequencies of interest up to a specified cut-off limit. During simulation, the axial velocity at the reference plane and the volume-integrated heat release rate over the computational domain are sampled at each time step (see Figure 6.1). These sampled signals are then decomposed into mean and fluctuating parts following Reynolds decomposition to obtain the fluctuating parts:

$$
\begin{aligned}
\hat{u}^{'}_{ref,i} &= \hat{u}_{ref,i} - \bar{\hat{u}}_{ref,i} \\
Q^{'}_i &= Q_i - \overline{Q}_i
\end{aligned}
\tag{6.1}
$$

For simplicity, the fluctuating parts $\hat{u}^{'}_{ref,i}$ and $Q^{'}_i$ are abbreviated as u_i and Q_i for the rest of the explanation. Having the sampled signals u_i and Q_i, the auto-correlation Γ matrix and cross-correlation **c** vector are defined as follows:

$$
\Gamma_{ij} = \frac{1}{N-L+1} \sum_{l=L}^{N} u_{l-i}u_{l-j} \quad \text{for} \quad i,j = 0,1,2,...,L
\tag{6.2}
$$

$$
c_i = \frac{1}{N-L+1} \sum_{l=L}^{N} u_{l-i}Q_l \quad \text{for} \quad i = 0,1,2,...,L
\tag{6.3}
$$
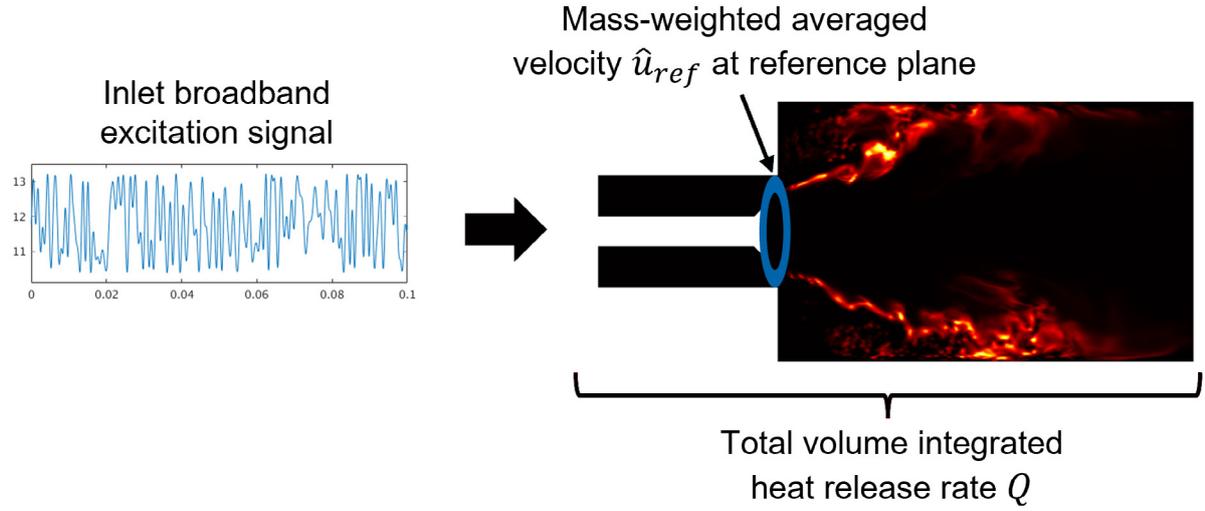
Figure 6.1: Schematic representation of an acoustically forced flame with a broadband signal in CFD simulations.

where N is the number of time steps in the broadband excitation signal. L is an integer, provided that $L \ll N$, and should be chosen that the response time $L\Delta t$ is not shorter than the longest-time-delay τ_{LTD} of the system. A general practice is to choose the L provided that $L\Delta t = \tau_{LTD}$ [86].

The following equation is known as the Wiener-Hopf equation:

$$\Gamma \mathbf{h} = \mathbf{c} \tag{6.4}$$

and the unit impulse response (UIR) coefficients h_k are obtained by taking the inverse of this equation, which is known as the Wiener-Hopf inversion (WHI).

$$\Gamma^{-1}\mathbf{c} = \mathbf{h} \tag{6.5}$$

Here, the $\mathbf{h}$ represents the UIR of the flame in the time domain and its z-transform gives the flame transfer function (FTF) in the frequency domain:

$$FTF(\omega) = \sum_{l=0}^{N} h_l e^{-i\omega\Delta t l} \tag{6.6}$$

Similarly, the inverse z-transform is given as follows:

$$h_k = \frac{\Delta t}{2\pi} \int_{-\pi/\Delta t}^{\pi/\Delta t} FTF(\omega) e^{i\omega\Delta t k} \, d\omega \tag{6.7}$$

where in Eqs. 6.6 and 6.7, the $\omega = 2\pi f$ is defined as the angular frequency.

Proper identification quality depends on the amplitude and length of the excitation signal, especially when system noise is present. Since the method's applicability is limited to linearly time-invariant systems [90], the amplitude of the excitation signal should be low enough not to

excite any non-linear flame response. On the other hand, good identification quality requires a signal-to-noise ratio of at least $A_s/A_n = 4$ with a length of at least 5 times the longest time-delay ($N \geq 5L$ in Eqs. 6.2 and 6.3) in the system [86].

In the current study, Daubechies wavelet [91] excitation signals are generated in *TFDtools* [89] with an excitation amplitude of 12% of the u_{inlet}, which corresponds to a ratio of A_s/A_n = 8, and a time length equal to 4 flow-through times (roughly corresponding to 10 times the longest-time-delay) for the 0% H_2 case, which has the largest time-delay because of its longest flame length. The three different broadband signals, created for the five cases listed in Table 4.1, are shown in Figure 6.2.
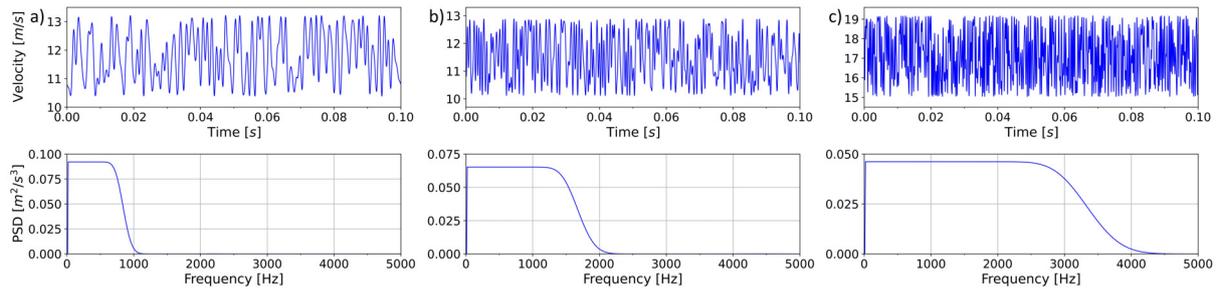
Figure 6.2: Broadband signals generated for SI, a) for the cases with 0% and 25.2% H_2, b) for the cases with 56.6% and 67% H_2, and c) for the case with 100% H_2 content.

As observed from Figure 6.2, the PSD of the signals has a constant amplitude up to the cut-off frequencies. Note that, as the hydrogen content in the fuel increases, the flame shortens, and the cut-off frequency increases. The flow-through-time τ_{FTT}, the cut-off frequency f_c, and the longest time delay τ_{LTD} can be calculated approximately as follows:

$$\tau_{FTT} = \frac{l_{pipe}}{\overline{\hat{u}}_{pipe}} + \frac{l_{cc}}{\overline{\hat{u}}_{cc}} \tag{6.8}$$

$$f_c = \frac{\overline{\hat{u}}_{ref}}{h_{cent.}} \tag{6.9}$$

$$\tau_{LTD} = \frac{h_{cent.}}{\overline{\hat{u}}_{z=h_{cent.}}} \tag{6.10}$$

where l_{pipe} and l_{cc} are the lengths of the pipe and combustion chamber sections of the computational domain, $\overline{\hat{u}}_{pipe}$ and $\overline{\hat{u}}_{cc}$ are the mass-weighted averaged velocity at these sections, respectively. $\overline{\hat{u}}_{ref}$ and $\overline{\hat{u}}_{z=h_{cent}}$ are the mass-weighted averaged velocities at reference ($z = 0$) and at $z = h_{cent.}$ axial locations, and $h_{cent.}$ is the mean flame centroid height calculated following Eq. 5.2.

6.2. FLAME TRANSFER FUNCTIONS (FTF)

The flame transfer functions are extracted from SAS and LES implementations of the proposed combustion modelling approach (ExtH$_2$LV). To investigate the impact of the stretch modelling,

FTFs are extracted from SAS and LES implementations with two different orientation factors $n_i \tilde{n}_j$ calculation methods. In total, FTFs are extracted from five different setups, two SAS, and three LES. Except for the extra LES setup, the solid walls are included in the computational domain and the conjugate heat transfer is solved. For the extra LES case, the temperature distribution is imposed at combustion chamber walls without modelling solid domains. These SAS and LES setups are explained as follows:

- LES-s1-T (see Figure 5.9 b) for mean flame shapes): The LES implementation with the resolved stretch according to the s1 model (see Table 3.2) in the C2 mesh configuration (see Figure 4.3), where the temperature distribution is imposed over the walls of the combustion chamber.

- LES-s1 (see Figure 5.12 e) for mean flame shapes): The LES implementation with the resolved stretch according to the s1 model (see Table 3.2) in the C3 mesh configuration (see Figure 4.3), where the HTC $= 8.6$ W/m^{2}K and HTC $= 100$ W/m^{2}K are assigned to back and side walls of the combustion chamber, respectively.

- LES-s2 (see Figure 5.12 f) for mean flame shapes): The LES implementation with the resolved stretch according to the s2 model (see Table 3.2) in the C3 mesh configuration (see Figure 4.3), where the HTC $= 8.6$ W/m^{2}K and HTC $= 100$ W/m^{2}K are assigned to back and side walls of the combustion chamber, respectively.

- SAS (see Figure 5.12 b) for mean flame shapes): The SAS implementation with the resolved/mean stretch according to the Eq. 3.8 in the C4 mesh configuration (see Figure 4.3), where the HTC $= 8.6$ W/m^{2}K and HTC $= 100$ W/m^{2}K are assigned to back and side walls of the combustion chamber, respectively.

- SAS-s2 (see Figure 5.12 d) for mean flame shapes): The SAS implementation with the resolved/mean stretch according to the s2 model (see Table 3.2) in the C4 mesh configuration (see Figure 4.3), where the HTC $= 8.6$ W/m^{2}K and HTC $= 100$ W/m^{2}K are assigned to back and side walls of the combustion chamber, respectively.

In Figure 6.3, the FTFs extracted from the SAS and LES computations are plotted together with the measured FTFs for the different contents of hydrogen. Comparing experimental FTFs in Figure 6.3, the cases with 56.6%, 67% and 100% H$_2$ exhibit modulations in the FTF gain (see the experimental FTF gains in Figure 6.3 c), d) and e)), while the cases with 0% and 25.2% H$_2$ do not (see the experimental FTF gains in Figure 6.3 a) and b)).

These modulations were investigated in [10] and it was revealed that their presence is due to the vortex shedding from the cylindrical supporting rods shown in Figure 4.4. These vortices perturb the flame and cause modulations in the total heat release, and consequently in the FTF gain due to convective-acoustic interference [10]. Flames whose cut-off frequency ($\omega_c = 2\pi f_c$) is close to or higher than the vortex shedding frequency ($\omega_c \approx \omega_s$ or $\omega_c > \omega_s$ i.e. shorter flames) are prone to show strong modulations in FTF gain, due to convective interference between shed vortices and acoustic velocity fluctuations which can augment or annihilate flame surface area [10, 11]. Figure 6.4 compares the calculated flame cut-off frequencies ω_c and the vortex shedding frequency ω_s. According to the abovementioned $\omega_c \geq \omega_s$ condition, modulations are

expected in the FTF gain plots for the cases which are above the dashed curve in Figure 6.4. The modulations in the FTF gain plots are not observed in the experimental results with 0% and 25.2% H_2 contents, validating the $\omega_c \geq \omega_s$ condition.
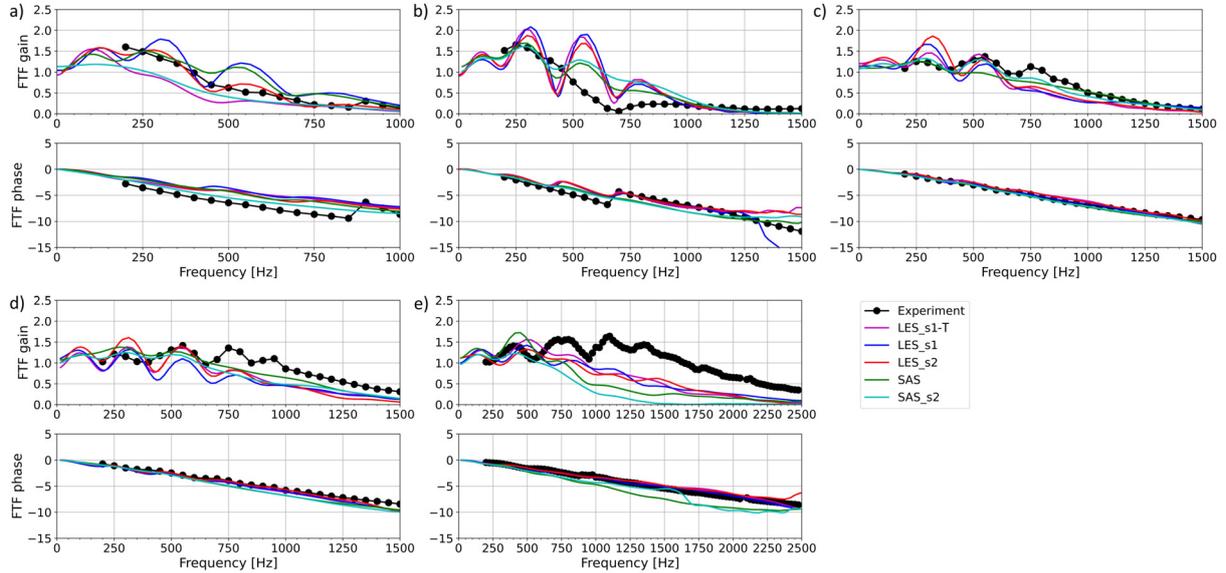
Figure 6.3: Extracted FTFs for a) 0% H_2 + 100% CH_4, b) 25.2% H_2 + 74.8% CH_4, c) 56.6% H_2 + 43.4% CH_4, d) 67% H_2 + 33% CH_4 and e) 100% H_2 + 0% CH_4.

For the CFD results, all the implementations predict the phase in good agreement with the experiments with slight over and under-predictions in some cases. The range of frequency response in the amplitude of the FTF is well captured by the identification, but all CFD cases, except LES-s1-T and SAS-s2, show some modulations in the FTF amplitude.

Based on the $\omega_c \geq \omega_s$ criteria, modulations are not expected to appear in the experiment and CFDs for 0% H_2 content (see Figure 6.4). Possibly the oscillations are appearing in the LES-s1, LES-s2 and SAS implementations as their cut-off frequency ω_c is quite close to the limit $\omega_c = \omega_s$. For example, the modulations are not present in LES-s1-T and SAS-s2 implementations whose cut-off frequencies ω_c are far from the $\omega_c = \omega_s$. The LES-s2 shows lower amplitude modulations than the LES-s1 and SAS as the ω_c in LES-s2 is lower than those in LES-s1 and SAS, reducing the probability of acoustic-convective interference. In parallel, ω_c is much far away from the limit in the experiment, consequently, the experimental FTF does not exhibit modulations. In general, the lower ω_c with respect to ω_s, the less probability of the appearance of such modulations in the FTF amplitude.

Comparing results in Figure 6.3 b) for the case with 25.2% H_2, all the CFD approaches predict modulations in the gain plots which are not present in the experiment. This result shows that apart from the $\omega_c \geq \omega_s$ criterion, the proposed modelling approach tends to show modulations, as the cut-off frequencies ω_c in SAS and SAS-s2, are quite close to the ones in the experiment. A possible explanation for this phenomenon would be that despite a good match achieved in mean flame shape predictions, due to its formulation, the proposed modelling closure (ExtH$_2$LV model) might be over-predicting the heat release rate fluctuations. This statement is investigated in Section 6.2.4. by comparing FTF predictions against ExtH$_2$TFC model.
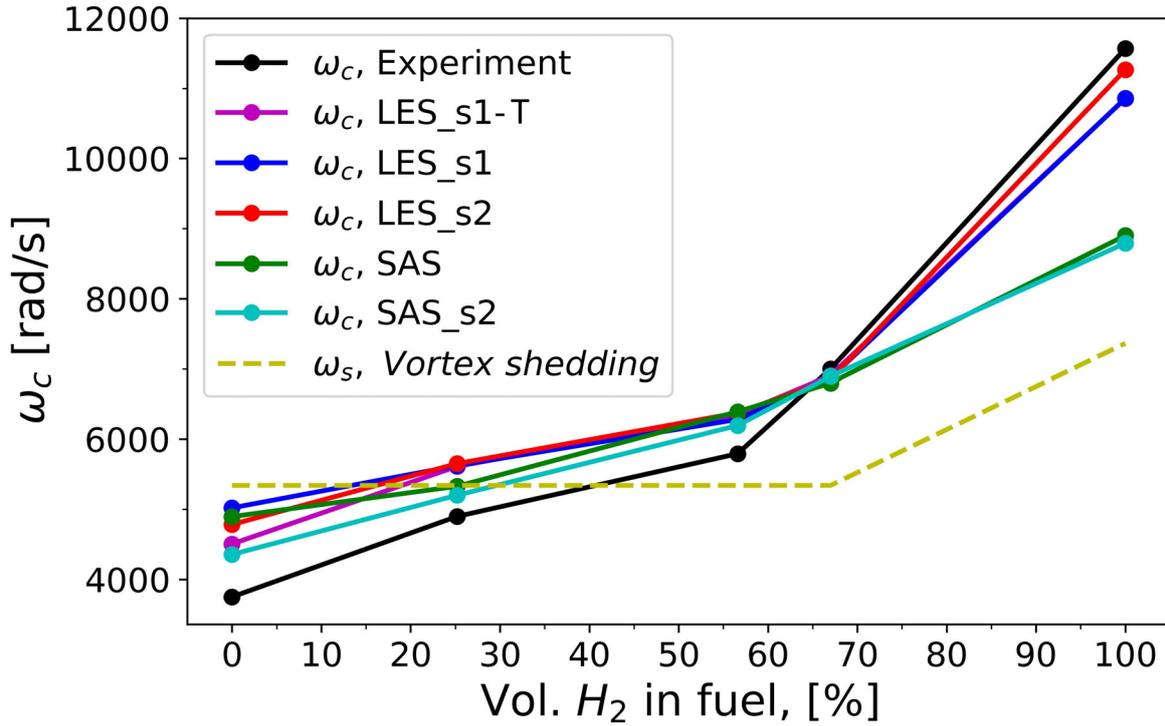
Figure 6.4: Flame response angular cut-off frequencies and angular vortex shedding frequency against increasing H$_2$ content.

For the cases with 56.6% and 67% H$_2$ (Figure 6.3 c) and d)) the gain is predicted in good agreement with experiments. The gain is slightly over-predicted by LES approaches at low frequencies up to 400-500 Hz, and slightly under-predicted at high frequencies beyond this point. SAS approaches exhibited even better agreements with experiments than LES implementations in gain plots at low and high frequencies. The FTF phases are predicted in good agreement with experiments by all the approaches.

In Figure 6.3 e), all the approaches exhibit the same behaviour for the gain plot as they capture the initial peaks of modulations, but for the higher frequencies, they all under-predict the gain. On the other hand, for the phase plot, LES implementations show good agreement with the experiment. A slight under-prediction of the phase is seen with SAS approaches due to its longer flame stabilization for this pure hydrogen case (see the last row in Figure 5.12) which increases the delay of the response (a longer flame produces a higher phase in the FTF).

6.2.1. Unit impulse responses (UIR)

To investigate the differences between the measured and the calculated FTFs, the flame dynamics is analysed in the time domain comparing the UIRs. The UIR from the CFD simulations is obtained as part of the SI process (**h** in Eq. 6.5), while the experimental UIRs are obtained by calculating the inverse z-transform (Eq. 6.7) of the measured FTFs. The UIR is the time

domain representation of the FTF, and it involves the gain and phase information of the FTF in a combined form in the time domain.

Komarek et al. [92] investigated the UIR of a flame against axial and tangential velocity fluctuations (impulses) and revealed that it exhibits different characteristics. The UIR of the flame to axial velocity fluctuations exhibits such a Gaussian-like shape that the UIR makes a positive peak with a significantly high amplitude compared to the following negative peak (see Figure 6.5 a)). In contrast to the axial one, the response to tangential perturbation exhibits different characteristics such that, the positive peak is followed by a negative peak with a comparable amplitude (see Figure 6.5 b)).
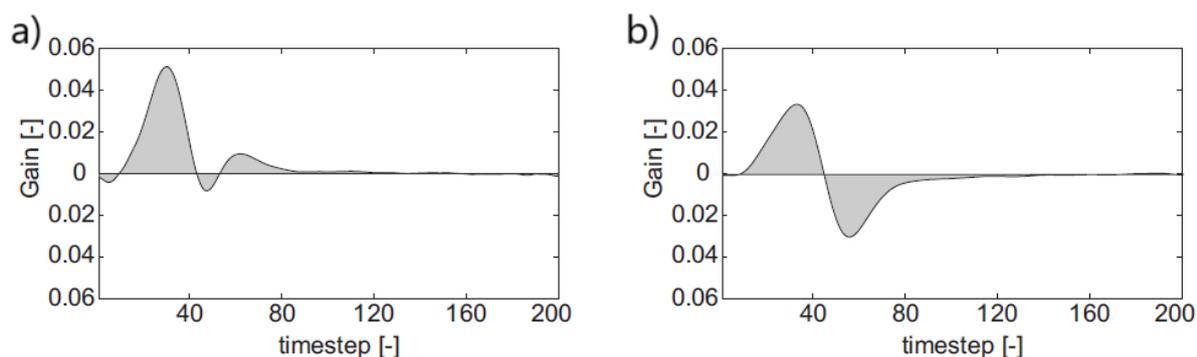
Figure 6.5: UIR of a flame to a) axial excitation, b) tangential excitation. Figure taken from Komarek et. al [92].
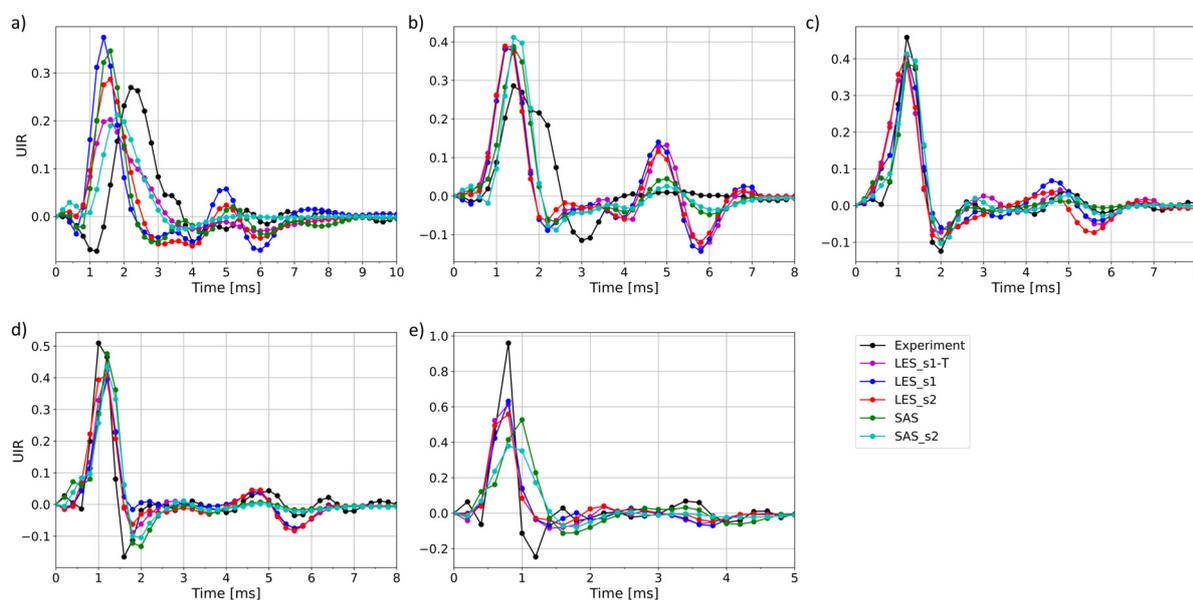
Figure 6.6: UIRs extracted for experiments and CFDs for a) 0% H_2 + 100% CH_4, b) 25.2% H_2 + 74.8% CH_4, c) 56.6% H_2 + 43.4% CH_4, d) 67% H_2 + 33% CH_4, e) 100% H_2 + 0% CH_4.

Bearing in mind the different UIR characteristics against axial and tangential perturbations, the experimental UIRs in Figure 6.6 show that, the flames with 0% and 25.2% H_2 respond

mainly to the axial fluctuations as the high amplitude positive peak (see $t \approx 1.5 - 3.5$ ms in Figure 6.6 a) and $t \approx 1 - 2.5$ ms in b)) is observed initially and no other negative peak (comparable to the positive high peak) follows. On the other hand, for the experiments with 56.6%, 67% and 100% H_2 content, the high amplitude positive peak corresponding to axial fluctuations (see $t \approx 0.8 - 1.5$ ms in Figure 6.6 c) and d), and $t \approx 0.5 - 1$ ms in e)) and the positive-negative subsequent peaks with equivalent amplitude corresponding to tangential velocity fluctuations (see $t \approx 4 - 6$ ms in Figure 6.6 c) and d), and $t \approx 3 - 4.5$ ms in e)) are observed clearly.

For the experimental setup, used in this study, since there is no swirler, the tangential velocity fluctuations are only promoted by the shed vortices from the bluff body supporting rods, shown in Figure 4.4. Considering this, the convective time for a vortex (referring to tangential fluctuation in the scope of this study), travelling from the rods (at $z = -0.045$ m) to the dump plane (at $z = 0$) may be calculated with Eq. 6.11.

$$\tau_{c,tan} \approx \frac{z_{dump} - z_{rods}}{\overline{\hat{u}}_{pipe} = u_{inlet}} \tag{6.11}$$

Approximately, the convective times for tangential fluctuations are calculated as $\tau_{c,tan} = 2.6$ ms for the pure hydrogen case, and as $\tau_{c,tan} = 4$ ms for the other cases. Supporting Komarek's finding, in Figure 6.6, there are positive-negative peak couples, referring to the response to tangential fluctuations (shedding vortices in our setup) as shown in Figure 6.5 b), which start to appear at the calculated convective times. Similarly, the convective time for the axial perturbation may be roughly calculated from Eq. 6.12.

$$\tau_{c,ax} \approx \frac{h_{cent.}}{\overline{\hat{u}}_{ref}} \tag{6.12}$$

Using Eq. 6.12, the convective times for the axial perturbations are calculated for the experimental flames as $\tau_{c,ax} \approx 1.5$ ms for the case with 0% H_2, $\tau_{c,ax} \approx 1.25$ ms for the case with 25.2% H_2, $\tau_{c,ax} \approx 0.8$ ms for the cases with 56.6% and 67% H_2, and $\tau_{c,ax} \approx 0.5$ ms for the pure hydrogen case. It is observed from Figure 6.6 that at these indicated values, the high amplitude positive peak starts appearing. Since the convective time for the response to axial perturbation depends on the flame centroid height $h_{cent.}$, the high amplitude positive peak in the UIR moves to a smaller time as the flame shortens.

In Figure 6.6 a) and b), due to shorter prediction of $h_{cent.}$, UIRs from CFDs shift towards the left (smaller time). Being different than experiments, but in accordance with the modulations seen in the FTFs, the UIRs from CFDs exhibit positive-negative peak couples, starting to appear at $\tau_{c,tan} = 4$ ms. So-called peak couples are not seen in the experiments for the cases with 0% and 25.2% H_2 and in the LES-s1-T and SAS-s2 implementations for the pure methane case. As mentioned in Section 6.2., the flames with higher cut-off frequency (short flames, $\omega_c > \omega_s$) compared to vortex shedding frequency, tend to show modulations in FTF gain due to acoustic-convective interference, which appears in the UIR plots as the response of the flame to tangential perturbations. A comparison of Figure 6.3 and 6.6 shows that the amplitude of the FTF gain modulations and of the positive-negative peak couples in the UIR are in linear relation with each other, supporting the idea that the higher the cut-off frequency, the higher the amplitude.

In Figure 6.3 c), d) and e) good agreements are achieved with the experiments, as in these cases FTF phases (related to time delay) are in very good agreement with experiments. For the cases with 56.6% and 67% H_2 (Figure 6.3 c), d)), the agreement in UIR amplitudes is also quite good, representing the good agreement in FTF gain. On the other hand, for the pure hydrogen case, the under-prediction of FTF gain (see Figure 6.3 e)) is observed as the under-predicted peak amplitude (see Figure 6.6 e)) in the UIR plot. Due to the over-predicted flame lengths in SAS implementations for the pure hydrogen case, the UIR shifts towards the right (larger time) compared to the experiment, inverse to what is observed for the cases with 0% and 25.2% H_2.

6.2.2. Effect of forcing amplitude

To investigate the effect of forcing amplitude on the FTF gain modulations, the LES-s1 implementation in the C3 mesh configuration is forced with the excitation signal having an amplitude of 6% ($A_s/A_n = 4$), and compared to the one having an amplitude of 12% ($A_s/A_n = 8$) for the cases with 0% and 25.2% H_2. In this comparison, the same signal is used and only the forcing amplitude is varied. In the experiments, the cases were forced with a harmonic excitation signal at each discrete frequency having an amplitude of 4% (see Section 4.1.). Using the same amplitude is not possible in CFD-SI with broadband excitation, since the signal-to-noise ratio lower than $A_s/A_n = 4$ causes identification problems [86].

It is observed from Figure 6.7 that the decrease in forcing amplitude decreases the amplitude of modulations seen in the FTF gain plots. It is also seen from the UIR plots that the decrease in forcing amplitude does not affect the response to axial perturbation (the amplitude of the positive initial peak referring to the response to axial perturbation does not change). However, it decreases the amplitude of the response to tangential perturbation (the amplitude of the positive-negative peak couple starts to appear at $t = \tau_{c,tan} \approx 4$ ms).

From this result, it can be revealed that the increase in the forcing amplitude increases the possibility of the presence of acoustic-convective interference, and the amplitude of modulations seen in the FTF gain plots.

6.2.3. Effect of flame length

In this section the effect of flame length prediction on the FTF gain modulations is examined by comparing the two identical LES-s1 implementation setups in the C3 mesh configuration for the case with 25% H_2. The ExtH$_2$LV model prediction was used as the control case, and for the other case, the reaction rate source term $\bar{\dot{\omega}}$ is multiplied by a coefficient of 0.6, resulting in longer flame stabilization. Figure 6.8 compares the mean flame shapes, axial HRR distributions, FTFs, and UIRs for these two cases.

As observed from Figure 6.8 b), the LES-s1-RC (with reduced reaction rate) case predicts the $h_{cent.}$ longer than the experiment while the LES-s1 predicts shorter. Accordingly, the modulation amplitudes in FTF and UIR plots are higher in the LES-s1 (shorter flame) and lower in the LES-s1-RC (longer flame) predictions. Similar to the effect of higher forcing amplitude, the shorter flame prediction promotes the possibility of the presence of acoustic-convective inter-
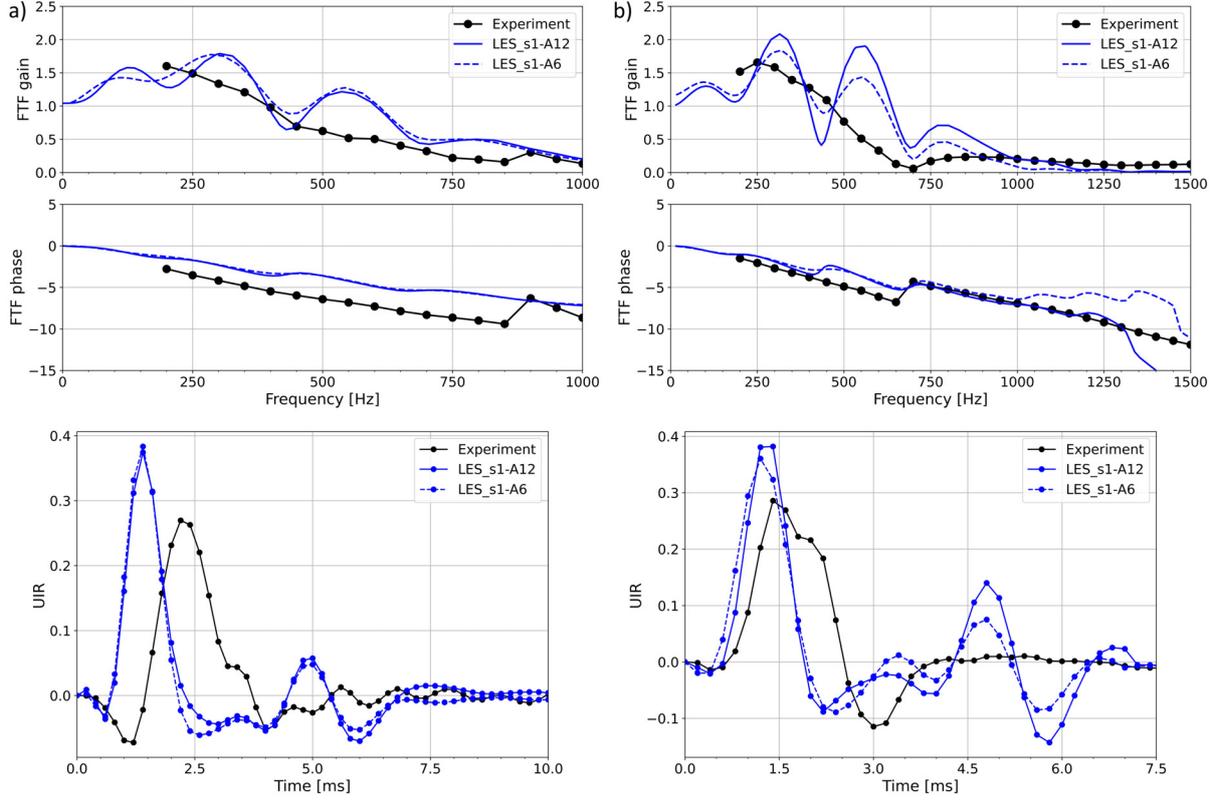
Figure 6.7: ExtH$_2$LV model FTFs and UIRs, extracted with broadband signal of different amplitudes (12% with $A_s/A_n = 8$, and 6% with $A_s/A_n = 4$) for the cases with a) 0% H$_2$ + 100% CH$_4$, b) 25.2% H$_2$ + 74.8% CH$_4$. The comparison is made in the C3 mesh configuration with the LES-s1 implementation.

ference and the modulations seen in the FTF plots.

6.2.4. Effect of turbulent velocity exponent in the closure

In this last section, the possible impact of the proportionality of the turbulent fluctuation velocity u' to the reaction rate source term $\overline{\dot{\omega}}$ is investigated by comparing the extracted FTFs and UIRs from the ExtH$_2$TFC and ExtH$_2$LV models. Note that the ExtH$_2$LV model has the proportionality of $\overline{\dot{\omega}} \propto u'^{1.05}$, while the ExtH$_2$TFC model has $\overline{\dot{\omega}} \propto u'^{0.8}$. The proportionality in the latter is obvious, as the $S_t \propto u'^{0.8}$ is the only term in the closure that is dependent on u' (see Eqs. 3.15 and 5.1). For the former, the $\overline{\dot{\omega}} \propto u'^{1.05}$ relation is obtained by substituting $S_t \propto u'^{0.8}$, $u_{\eta K, SGS} \propto u'^{0.75}$, and $\tilde{k}_{SGS} \propto u'^2$ relations into Eq. 3.16.

For the comparison, the case with 25% H$_2$ is selected, as the flame length and flame centroid height $h_{cent.}$ predictions, and accordingly the cut-off frequencies ω_c by the two models are almost identical (see Figures 5.9 and 5.11). The comparison was made in the C2 mesh configuration with the LES-s1 implementation setup as explained in Section 5.3., and the same broadband excitation signal was used for the acoustic forcing.

Figure 6.9 compares the FTFs and UIRs extracted from these two models for the cases with
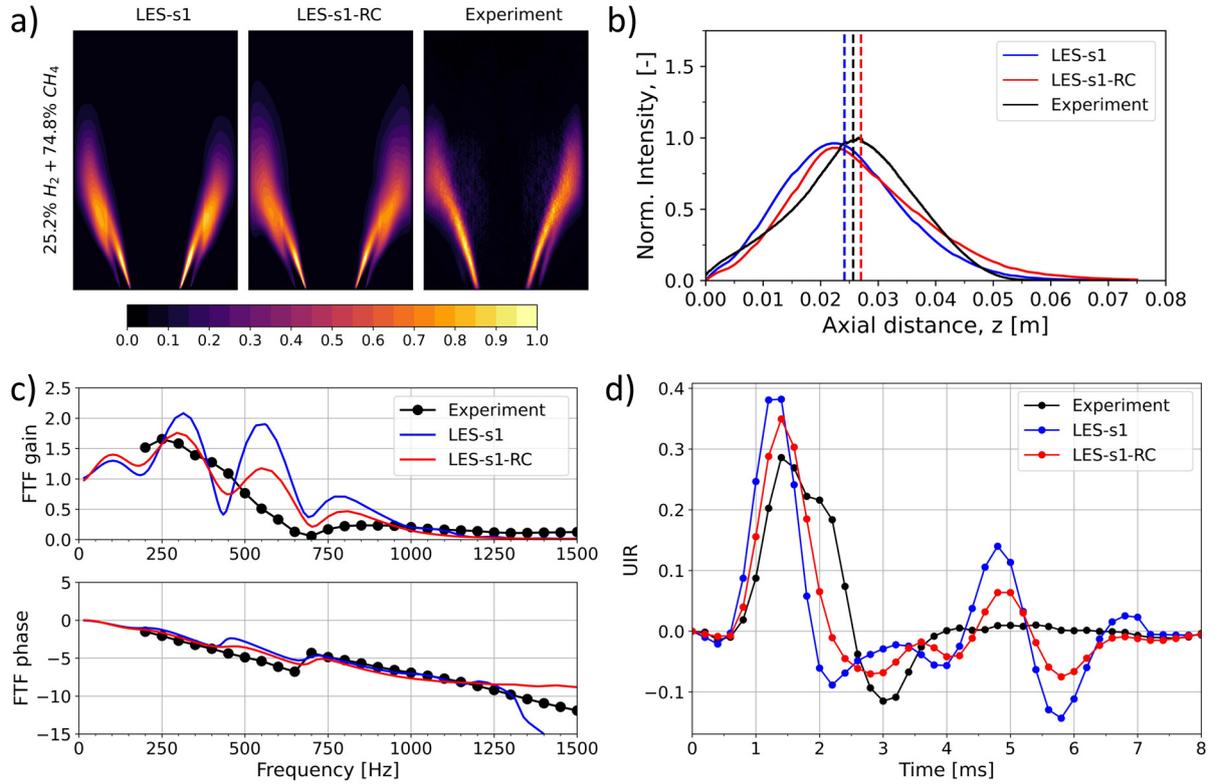
Figure 6.8: ExtH$_2$LV model (LES-s1) vs ExtH$_2$LV model with reduced reaction rate (LES-s1-RC) a) mean flame shapes, b) axial HRR distributions, c) FTFs and d) UIRs for the case with 25.2% H$_2$. The comparison is made in the C3 mesh configuration with the LES-s1 implementation. FTFs and UIRs, extracted with a broadband signal having an amplitude of 12% with $A_s/A_n = 8$.

0% and 25% H$_2$. As observed from Figure 6.9 b), both models predict modulations in the FTF plot, however, the amplitude of these modulations is higher in the ExtH$_2$LV model ($\bar{\bar{\omega}} \propto u'^{1.05}$), where it is lower in the ExtH$_2$TFC model ($\bar{\bar{\omega}} \propto u'^{0.8}$). This result may suggest an idea that the higher exponent of u' in the closure $\bar{\bar{\omega}}$, the higher the fluctuations in the integrated heat release rate (Q_i' in Eq. 6.1), which may increase the probability of the presence of acoustic-convective interference, and hence the amplitude of modulations in the FTF plots.

Apart from that, in Figure 6.9 a), the results were compared for the pure methane case. Although this case is not suitable to make the comparison due to differently predicted flame length and flame centroid heights $h_{cent.}$ by the models (see Figures 5.9 and 5.11), it is plotted to show the importance of the model coefficient in flame dynamics. As observed from Figures 5.9 and 5.11, despite better predicted $h_{cent.}$ by the ExtH$_2$TFC model, the adjusted model coefficient for the LES implementation of this model (see Section 5.3.) based on the best match with the experimental flame length, is not sufficient for representing the correct dynamics. As observed, the FTF gain is predicted too low with the ExtH$_2$TFC model due to insufficient heat release rate and hence the model coefficient.

Note that, different from the ExtH$_2$TFC model, the implementation of the ExtH$_2$LV model in LES, or the model's translation from RANS to SAS or LES does not require an adjustment
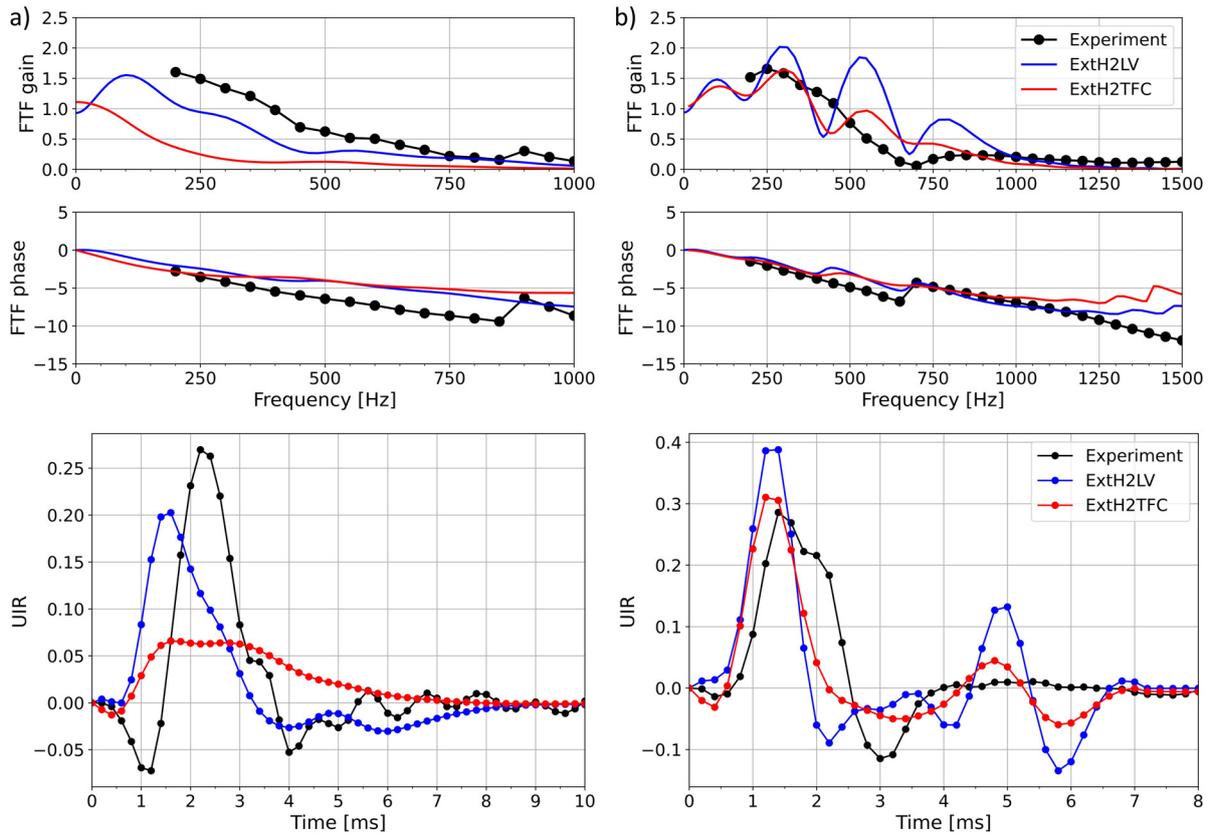
Figure 6.9: ExtH$_2$LV versus ExtH$_2$TFC model FTF and UIR comparison for a) 0% H$_2$ + 100% CH$_4$, b) 25.2% H$_2$ + 74.8% CH$_4$. The comparison is made in the C2 mesh configuration with the LES-s1 implementation. FTFs and UIRs, extracted with a broadband signal having an amplitude of 12% with $A_s/A_n = 8$.

in the model coefficient.

6.2.5. Conclusions

The performance of the proposed modelling approach on flame dynamics is investigated in terms of FTFs and UIRs in SAS and LES contexts. The conclusions are listed as follows:

- Comparison of FTFs with experiments shows that the proposed ExtH$_2$LV modelling approach is capable of reproducing the flame dynamics in both SAS and LES contexts with reasonable agreements with experiments. In the phase plots, quite good agreements with experiments were achieved, however, for the gain plots, some discrepancies were observed depending on the hydrogen content.

- Further investigation of the discrepancies showed that the modulations observed in the CFDs, but not in the experiments, are promoted by the shorter flame predictions, and higher acoustic forcing amplitude requirement in CFDs compared to experiments. How-

ever, in addition to this, the turbulent velocity exponent ($\overline{\overline{\omega}} \propto u'^{1.05}$) in the proposed modelling closure is also found responsible for the amplification of the modulations.

- SAS and LES implementations provide consistent results with each other. For the cases with 56.6% and 67% H_2 content, SAS implementations provided even better agreements than LES with experiments.

- Different stretch modelling approaches, solving conjugate heat transfer or imposing a temperature distribution over the wall surfaces do not affect directly the FTF prediction but they impact implicitly through the length and accordingly the cut-off frequency of the predicted flames.

OUTCOMES AND OUTLOOK

This thesis study presents a combustion modelling approach for CFD simulations of turbulent premixed CH_4/H_2/air flames. The model accounts for stretch, heat loss and hydrogen enrichment effects, responsible for the correct flame stabilization shapes, by means of an algebraic closure proposed for the source term of the progress variable equation. The proposed closure is a function of a novel turbulent flame speed expression derived in this study and is found empirically with the incorporation of the turbulent flame speed into algebraic reaction rate closures by aiming at the best match with the experiments.

First, a turbulent flame speed expression has been derived by combining two expressions from literature as a function of stretch, heat loss and effective Lewis number, and was calibrated against atmospheric lean and stoichiometric CH_4/H_2/air mixtures in spherical expanding turbulent flame experiments available in the literature. In this expression, stretch and heat loss effects are taken into account by means of laminar consumption speeds tabulated in a fresh-to-burnt counter flow flame configuration with a detailed chemistry approach at different levels of strain and heat loss. And the hydrogen enrichment effects are accounted for by updating the model coefficient through the effective Lewis number.

Then the derived turbulent flame speed was incorporated into four different algebraic reaction rate closures available in the literature and the best match with the experimental flame shapes and axial heat release rate distributions was sought in RANS and LES context CFD simulations. The best match was achieved with a reaction rate closure based on the fractal theory. The incorporation of the turbulent flame speed into the fractal-based closure required an assumption that the turbulent flame brush thickness is a function of turbulent flame speed. This assumption was not investigated exclusively in this study and has been left for future studies.

The reaction rate closure has only one model coefficient coming from the turbulent flame speed expression. The validation of the model was done for the mean flame shape and FTF predictions in the *NTNU* atmospheric single sector test rig, for turbulent premixed CH_4/H_2/air flame experiments up to 100% H_2 content. The implementation of the modelling closure in RANS, SAS and LES context CFDs showed that the model does not require calibration in the coefficient for its transformation from RANS to SAS or LES and is capable of reproducing the correct flame shapes observed in the experiments with all the turbulence modelling approaches from pure methane to pure hydrogen. In the FTF comparison, the model provided reasonable agreements with experiments, while further improvements may be achieved with an improvement in modelling the turbulent flame brush thickness term.

7.1. OUTCOMES

The main outcomes from this study can be listed as follows:

- The novel turbulent flame speed expression ($S_t = f(\kappa, \beta, Le^*)$), which accounts for stretch, heat loss, and hydrogen enrichment effects, presents improvements with respect

to the other models in the literature and is able to reproduce the transition from V to M flame shapes against increasing hydrogen content in its incorporation into reaction rate closure models for CFD simulations.

- The effective Lewis number Le^* included in the S_t expression, automatically updates the model coefficient and is responsible for the correct prediction of the flame length, especially at high H_2 contents in the mixture.

- The predicted correct flame stabilization topology is attributed to the quenching effects produced by the combined effect of flame stretch and heat loss.

- The proposed closure, which accounts for stretch, heat loss and hydrogen enrichment effects, has only one coefficient coming from S_t expression, can be implemented in RANS, SAS and LES context CFDs and does not require a parametric CFD study for calibrating the coefficient. It uses the same coefficient for all the turbulence modelling approaches, and this coefficient is calibrated from one-dimensional turbulence flame speed measurements.

- The proposed closure provides consistent results in RANS, SAS and LES context CFDs, reproducing the correct flame stabilizations seen in the experiments with all the turbulence modelling approaches.

- The proposed closure is capable of reproducing the flame dynamics with reasonable agreements with experiments in both SAS and LES context CFDs. Consistent results obtained with SAS and LES show the model's robustness. The model implementation in SAS context CFD could be a low-cost alternative to the LES simulation, as in some cases, the experimental FTFs are better predicted with the SAS implementation.

- The extension of the model to rich mixture conditions and/or high-pressure simulations requires only the recalibration of the S_t expression against turbulent flame speed measurements at the rich mixture and/or high-pressure conditions.

7.2. OUTLOOK

The proposed modelling approach provided promising results for future applications. Some of the ideas that can be investigated in future are listed as follows:

- The proposed model's application to the partially premixed and high-pressure conditions (industrial burner conditions) was not carried out in this study. This is planned in future investigations.

- As mentioned in Section 5.4.1., due to its formulation, the proposed closure can cause a numerical ignition problem in RANS simulations at near-wall boundaries where strong flame wall interactions are present. To remedy this, wall-quenching models need to be implemented. The investigation of wall-quenching models and coupling them to the proposed closure may be the subject of future studies.

- As mentioned in the text above, the proposed model was obtained at the end of an empirical study, and its possible derivation from the fractal theory required an assumption that the turbulent flame brush thickness is a function of turbulent flame speed (see Section 3.3.1.). This assumption was not investigated exclusively in this study and has been planned for future studies.

ACKNOWLEDGEMENTS

REFERENCES

[1] ETN hydrogen gas turbine report: The path towards a zero-carbon gas turbine. Technical report, ETN Global, Brussels, Belgium, January 2020. URL https://etn.global/wp-content/uploads/2020/02/ETN-Hydrogen-Gas-Turbines-report.pdf.

[2] A. Ciani, L. Tay-Wo-Chong, A. Amato, E. Bertolotto, and G. Spataro. Hydrogen blending into Ansaldo Energia AE94.3A gas turbine: High pressure tests, field experience and modelling considerations. Proceedings of the ASME Turbo Expo: Power for Land, Sea, and Air. Volume 3A: Combustion, Fuels, and Emissions, June 2021. doi: https://doi.org/10.1115/GT2021-58650. V03AT04A009.

[3] E. Æsøy, J. G. Aguilar, S. Wiseman, M. R. Bothien, N. A. Worth, and J. R. Dawson. Scaling and prediction of transfer functions in lean premixed H_2/CH_4-flames. *Combustion and Flame*, 215:269–282, 2020. ISSN 0010-2180. doi: https://doi.org/10.1016/j.combustflame.2020.01.045.

[4] R. Mao, J. Wang, W. Zhang, Z. An, W. Lin, M. Zhang, and Z. Huang. Effect of high hydrogen enrichment on the outer-shear-layer flame of confined lean premixed CH_4/H_2/air swirl flames. *International Journal of Hydrogen Energy*, 46(34):17969–17981, 2021. ISSN 0360-3199. doi: https://doi.org/10.1016/j.ijhydene.2021.02.181.

[5] T.F. Guiberti, D. Durox, P. Scouflaire, and T. Schuller. Impact of heat loss and hydrogen enrichment on the shape of confined swirling flames. *Proceedings of the Combustion Institute*, 35(2):1385–1392, 2015. ISSN 1540-7489. doi: https://doi.org/10.1016/j.proci.2014.06.016.

[6] L. Tay-Wo-Chong, T. Komarek, M. Zellhuber, J. Lenz, C. Hirsch, and W. Polifke. Influence of strain and heat loss on flame stabilization in a non-adiabatic combustor. Proceedings of the 4th European Combustion Meeting, 2009.

[7] L. Tay-Wo-Chong, M. Zellhuber, T. Komarek, H. G. Im, and W. Polifke. Combined influence of strain and heat loss on turbulent premixed flame stabilization. *Flow Turbulence Combust*, 97(1):263–294, July 2016. doi: https://doi.org/10.1007/s10494-015-9679-0.

[8] L. Tay-Wo-Chong, A. Scarpato, and W. Polifke. LES Combustion Model With Stretch and Heat Loss Effects for Prediction of Premix Flame Characteristics and Dynamics. Proceedings of the ASME Turbo Expo: Power for Land, Sea, and Air. Volume 4A: Combustion, Fuels and Emissions, June 2017. doi: https://doi.org/10.1115/GT2017-63357. V04AT04A029.

[9] Y. Tang and V. Raman. Large eddy simulation of premixed turbulent combustion using a non-adiabatic, strain-sensitive flamelet approach. *Combustion and Flame*, 234:111655, 2021. ISSN 0010-2180. doi: https://doi.org/10.1016/j.combustflame.2021.111655.

[10] E. Æsøy, J. G. Aguilar, M. R. Bothien, N. A. Worth, and J. R. Dawson. Acoustic-Convective Interference in Transfer Functions of Methane/Hydrogen and Pure Hydrogen

Flames. *Journal of Engineering for Gas Turbines and Power*, 143(12), October 2021. ISSN 0742-4795. doi: https://doi.org/10.1115/1.4051960. 121017.

[11] E. Æsøy, H. T. Nygård, N. A. Worth, and J. R. Dawson. Tailoring the gain and phase of the flame transfer function through targeted convective-acoustic interference. *Combustion and Flame*, 236:111813, 2022. ISSN 0010-2180. doi: https://doi.org/10.1016/j.combustflame. 2021.111813.

[12] Ansaldo Energia AE94.3A Heavy Duty Gas Turbine. URL https://www.ansaldoenergia.com/offering/equipment/turbomachinery/heavy-duty-gas-turbine/ae943a. Accessed: 2022-12-23.

[13] T. Poinsot and D. Veynante. *Theoretical and Numerical Combustion*. Institut de Mécanique des Fluides de Toulouse, 3rd edition, 2012.

[14] N. Peters. *Turbulent Combustion*. Cambridge University Press, 2000. doi: 10.1017/CBO9780511612701.

[15] D. Veynante and L. Vervisch. Turbulent combustion modeling. *Progress in Energy and Combustion Science*, 28(3):193–266, 2002. ISSN 0360-1285. doi: https://doi.org/10.1016/S0360-1285(01)00017-X.

[16] S. M. Candel and T. J. Poinsot. Flame stretch and the balance equation for the flame area. *Combustion Science and Technology*, 70(1-3):1–15, 1990. doi: https://doi.org/10.1080/00102209008951608.

[17] T. Mantel and J.M. Samaniego. Fundamental mechanisms in premixed turbulent flame propagation via vortex–flame interactions part II: numerical simulation. *Combustion and Flame*, 118(4):557–582, 1999. ISSN 0010-2180. doi: https://doi.org/10.1016/S0010-2180(99)00019-X.

[18] D. Bradley, P.H. Gaskell, A. Sedaghat, and X.J. Gu. Generation of PDFS for flame curvature and for flame stretch rate in premixed turbulent combustion. *Combustion and Flame*, 135(4):503–523, 2003. ISSN 0010-2180. doi: https://doi.org/10.1016/S0010-2180(03)00181-0.

[19] T. Lieuwen, V. McDonell, D. Santavicca, and T. Sattelmayer. Burner development and operability issues associated with steady flowing syngas fired combustors. *Combustion Science and Technology*, 180(6):1169–1192, 2008. doi: https://doi.org/10.1080/00102200801963375.

[20] H. Kutkan, A. Amato, G. Campa, G. Ghirardo, L. Tay-Wo-Chong, and E. Æsøy. Modeling of Turbulent Premixed CH_4/H_2/air Flames Including the Influence of Stretch and Heat Losses. *Journal of Engineering for Gas Turbines and Power*, 144(1), October 2021. ISSN 0742-4795. doi: https://doi.org/10.1115/1.4051989. 011020.

[21] J. B. Bell, R. K. Cheng, M. S. Day, and I. G. Shepherd. Numerical simulation of Lewis number effects on lean premixed turbulent flames. *Proceedings of the Combustion Institute*, 31(1):1309–1317, 2007. ISSN 1540-7489. doi: https://doi.org/10.1016/j.proci.2006.07.216.

[22] G.P. Smith, D.M. Golden, M. Frenklach, N.W. Moriarty, B. Eiteneer, M. Goldenberg, C.T. Bowman, R.K. Hanson, S. Song, W.C. Gardiner, V.V. Lissianski, and Z. Qin. GRI-MECH 3.0. URL http://www.me.berkeley.edu/gri_mech/. Accessed: 2022-12-23.

[23] D. Iurashev. *Numerical and analytical study of combustion instabilities in industrial gas turbines*. PhD thesis, Universita degli studi di Genova, 2017.

[24] L. Tay-Wo-Chong. *Numerical Simulation of the Dynamics of Turbulent Swirling Flames*. PhD thesis, Technische Universität München, 2012.

[25] R. Mercier, T.F. Guiberti, A. Chatelier, D. Durox, O. Gicquel, N. Darabiha, T. Schuller, and B. Fiorina. Experimental and numerical investigation of the influence of thermal boundary conditions on premixed swirling flame stabilization. *Combustion and Flame*, 171:42–58, 2016. ISSN 0010-2180. doi: https://doi.org/10.1016/j.combustflame.2016.05.006.

[26] A. Chatelier, T. Guiberti, R. Mercier, N. Bertier, B. Fiorina, and T. Schuller. Experimental and numerical investigation of the response of a swirled flame to flow modulations in a non-adiabatic combustor. *Flow, Turbulence and Combustion*, 102:995–1023, 2019. doi: https://doi.org/10.1007/s10494-018-9995-2.

[27] P.W. Agostinelli, D. Laera, I. Boxx, L. Gicquel, and T. Poinsot. Impact of wall heat transfer in large eddy simulation of flame dynamics in a swirled combustion chamber. *Combustion and Flame*, 234:111728, 2021. ISSN 0010-2180. doi: https://doi.org/10.1016/j.combustflame.2021.111728.

[28] P.W. Agostinelli, D. Laera, I. Chterev, I. Boxx, L. Gicquel, and T. Poinsot. On the impact of H_2-enrichment on flame structure and combustion dynamics of a lean partially-premixed turbulent swirling flame. *Combustion and Flame*, 241:112120, 2022. ISSN 0010-2180. doi: https://doi.org/10.1016/j.combustflame.2022.112120.

[29] A.M. Garcia, S. Le Bras, J. Prager, M. Häringer, and W. Polifke. Large eddy simulation of the dynamics of lean premixed flames using global reaction mechanisms calibrated for CH_4–H_2 fuel blends. *Physics of Fluids*, 34:095105, 2022. doi: https://doi.org/10.1063/5.0098898.

[30] W. Polifke, W. Geng, and K. Döbbeling. Optimization of rate coefficients for simplified reaction mechanisms with genetic algorithms. *Combustion and Flame*, 113(1):119–134, 1998. ISSN 0010-2180. doi: https://doi.org/10.1016/S0010-2180(97)00212-5.

[31] V. Zimont, W. Polifke, M. Bettelini, and W. Weisenstein. An Efficient Computational Model for Premixed Turbulent Combustion at High Reynolds Numbers Based on a Turbulent Flame Speed Closure. *Journal of Engineering for Gas Turbines and Power*, 120(3): 526–532, 07 1998. ISSN 0742-4795. doi: https://doi.org/10.1115/1.2818178.

[32] H.P. Schmid, P. Habisreuther, and W. Leuckel. A model for calculating heat release in premixed turbulent flames. *Combustion and Flame*, 113(1):79–91, 1998. ISSN 0010-2180. doi: https://doi.org/10.1016/S0010-2180(97)00193-4.

[33] P.C. Nassini, D. Pampaloni, R. Meloni, and A. Andreini. Lean blow-out prediction in an industrial gas turbine combustor through a LES-based CFD analysis. *Combustion and Flame*, 229:111391, 2021. ISSN 0010-2180. doi: https://doi.org/10.1016/j.combustflame.2021.02.037.

[34] N. Klarmann, T. Sattelmayer, W. Geng, Benjamin T. Zoller, and F. Magni. Impact of Flame Stretch and Heat Loss on Heat Release Distributions in Gas Turbine Combustors: Model Comparison and Validation. Proceedings of the ASME Turbo Expo: Power for Land, Sea, and Air. Volume 4B: Combustion, Fuels and Emissions, June 2016. doi: https://doi.org/10.1115/GT2016-57625. V04BT04A031.

[35] N. Klarmann, T. Sattelmayer, W. Geng, and F. Magni. Flamelet Generated Manifolds for Partially Premixed, Highly Stretched and Non-Adiabatic Combustion in Gas Turbines. Proceedings of the 54th AIAA Aerospace Sciences Meeting, 2016. doi: https://arc.aiaa.org/doi/abs/10.2514/6.2016-2120.

[36] F. Dinkelacker, B. Manickam, and S.P.R. Muppala. Modelling and simulation of lean premixed turbulent methane/hydrogen/air flames with an effective Lewis number approach. *Combustion and Flame*, 158(9):1742–1749, 2011. ISSN 0010-2180. doi: https://doi.org/10.1016/j.combustflame.2010.12.003.

[37] S.P.R. Muppala, N.K. Aluri, F. Dinkelacker, and A. Leipertz. Development of an algebraic reaction rate closure for the numerical calculation of turbulent premixed methane, ethylene, and propane/air flames for pressures up to 1.0 MPa. *Combustion and Flame*, 140(4): 257–266, 2005. ISSN 0010-2180. doi: https://doi.org/10.1016/j.combustflame.2004.11.005.

[38] P. Siewart. *Flame front characteristics of turbulent lean premixed methane/air flames at high-pressure*. PhD thesis, Swiss Federal Institute of Technology Zurich, 2006.

[39] B. Manickam, J. Franke, S.P.R. Muppala, and F. Dinkelacker. Large-eddy simulation of triangular-stabilized lean premixed turbulent flames: Quality and error assessment. *Flow, Turbulence and Combustion*, 88:563–596, 2012. doi: https://doi.org/10.1007/s10494-011-9385-5.

[40] S.P.R. Muppala, B. Manickam, and F. Dinkelacker. A comparative study of different reaction models for turbulent methane/hydrogen/air combustion. *Journal of Thermal Engineering*, 1:367–380, 2015. doi: 10.18186/jte.60394.

[41] H. Kutkan and J. Guerrero. Turbulent premixed flame modeling using the algebraic flame surface wrinkling model: A comparative study between OpenFOAM and Ansys Fluent. *Fluids*, 6(12), 2021. ISSN 2311-5521. doi: https://doi.org/10.3390/fluids6120462.

[42] V.L. Zimont and V. Battaglia. Joint RANS/LES approach to premixed flames modelling in the context of the TFC combustion model. In W. Rodi and M. Mulas, editors, *Engineering Turbulence Modelling and Experiments 6*, pages 905–914. Elsevier Science B.V., Amsterdam, 2005. ISBN 978-0-08-044544-1. doi: https://doi.org/10.1016/B978-008044544-1/50087-X.

[43] U. Allauddin, S.R.R. Lomada, and M. Pfitzner. Investigation of pressure and the lewis number effects in the context of algebraic flame surface density closure for les of premixed turbulent combustion. *Theoretical and Computational Fluid Dynamics*, 35:17–37, 2021. doi: https://doi.org/10.1007/s00162-020-00543-x.

[44] H. Tennekes and J.L. Lumley. *A First Course in Turbulence*. The MIT Press, 1st edition, 1972.

[45] S.B. Pope. *Turbulent Flows*. Cambridge University Press, 1st edition, 2000.

[46] A.N. Lipatnikov and J. Chomiak. Turbulent flame speed and thickness: phenomenology, evaluation, and application in multi-dimensional simulations. *Progress in Energy and Combustion Science*, 28(1):1–74, 2002. ISSN 0360-1285. doi: https://doi.org/10.1016/S0360-1285(01)00007-7.

[47] F.C. Gouldin. An application of fractals to modeling premixed turbulent flames. *Combustion and Flame*, 68(3):249–266, 1987. ISSN 0010-2180. doi: https://doi.org/10.1016/0010-2180(87)90003-4.

[48] F.C. Gouldin, K.N.C. Bray, and J.-Y. Chen. Chemical closure model for fractal flamelets. *Combustion and Flame*, 77(3):241–259, 1989. ISSN 0010-2180. doi: https://doi.org/10.1016/0010-2180(89)90132-6.

[49] K.N.C. Bray. Studies of the turbulent burning velocity. *Proceedings of the Royal Society London A: Mathematical, Physical and Engineering Sciences*, 431:315–335, 1990. doi: https://doi.org/10.1098/rspa.1990.0133.

[50] Ansys Fluent, Fluent Theory Guide v19.3.

[51] F.R. Menter and Y. Egorov. The scale-adaptive simulation method for unsteady turbulent flow predictions. part 1: Theory and model description. *Flow Turbulence and Combustion*, 85:113–138, 2010. doi: https://doi.org/10.1007/s10494-010-9264-5.

[52] Y. Egorov, F.R. Menter, R. Lechner, and D. Cokljat. The scale-adaptive simulation method for unsteady turbulent flow predictions. part 2: Application to complex flows. *Flow Turbulence and Combustion*, 85:139–165, 2010. doi: https://doi.org/10.1007/s10494-010-9265-4.

[53] W.W. Kim and S. Menon. Application of the localized dynamic subgrid-scale model to turbulent wall-bounded flows. Proceedings of the 35th Aerospace Sciences Meeting and Exhibit, 1997. doi: https://arc.aiaa.org/doi/abs/10.2514/6.1997-210.

[54] V.L. Zimont. Theory of Turbulent Combustion of a Homogeneous Fuel Mixture at High Reynolds Numbers. *Translated from Fizika Goreniya i Vzryva*, 15(3):23–32, 1979.

[55] V.L. Zimont. Gas premixed combustion at high turbulence. turbulent flame closure combustion model. *Experimental Thermal and Fluid Science*, 21(1):179–186, 2000. ISSN 0894-1777. doi: https://doi.org/10.1016/S0894-1777(99)00069-2.

[56] P. Flohr and H. Pitsch. A turbulent flame speed closure model for LES of industrial burner flows. Stanford University Center for Turbulence Research Proceedings of the Summer Program 2000, 2000.

[57] H. Kutkan, A. Amato, G. Campa, L. Tay-Wo-Chong, and E. Æsøy. Assessment of turbulent premixed combustion models for CH_4/H_2/air flames. Proceedings of the 27th International Congress on Sound and Vibration, 2021.

[58] H. Kutkan, A. Amato, G. Campa, L. Tay-Wo-Chong, and E. Æsøy. LES of Turbulent Premixed CH_4/H_2/Air Flames With Stretch and Heat Loss for Flame Characteristics and Dynamics. Proceedings of the ASME Turbo Expo: Power for Land, Sea, and Air. Volume 3B: Combustion, Fuels, and Emissions, June 2022. doi: https://doi.org/10.1115/GT2022-82397. V03BT04A021.

[59] C. Meneveau and T. Poinsot. Stretching and quenching of flamelets in premixed turbulent combustion. *Combustion and Flame*, 86(4):311–332, 1991. ISSN 0010-2180. doi: https://doi.org/10.1016/0010-2180(91)90126-V.

[60] S. Bougrine, S. Richard, O. Colin, and D. Veynante. Fuel composition effects on flame stretch in turbulent premixed combustion: Numerical analysis of flame-vortex interaction and formulation of a new efficiency function. *Flow Turbulence and Combustion*, 93: 259–281, 2014. doi: https://doi.org/10.1007/s10494-014-9546-4.

[61] D. Veynante, J. Piana, J.M. Duclos, and C. Martel. Experimental analysis of flame surface density models for premixed turbulent combustion. *Symposium (International) on Combustion*, 26(1):413–420, 1996. ISSN 0082-0784. doi: https://doi.org/10.1016/S0082-0784(96)80243-8.

[62] E.R Hawkes and R.S Cant. Implications of a flame surface density approach to large eddy simulation of premixed turbulent combustion. *Combustion and Flame*, 126(3):1617–1629, 2001. ISSN 0010-2180. doi: https://doi.org/10.1016/S0010-2180(01)00273-5.

[63] M. Fairweather, M.P. Ormsby, C.G.W. Sheppard, and R. Woolley. Turbulent burning rates of methane and methane–hydrogen mixtures. *Combustion and Flame*, 156(4):780–790, 2009. ISSN 0010-2180. doi: https://doi.org/10.1016/j.combustflame.2009.02.001.

[64] L.J. Jiang, S.S. Shy, W.Y. Li, H.M. Huang, and M.T. Nguyen. High-temperature, high-pressure burning velocities of expanding turbulent premixed flames and their comparison with bunsen-type flames. *Combustion and Flame*, 172:173–182, 2016. ISSN 0010-2180. doi: https://doi.org/10.1016/j.combustflame.2016.07.021.

[65] M.T. Nguyen, D.W. Yu, and S.S. Shy. General correlations of high pressure turbulent burning velocities with the consideration of Lewis number effect. *Proceedings of the Combustion Institute*, 37(2):2391–2398, 2019. ISSN 1540-7489. doi: https://doi.org/10.1016/j.proci.2018.08.049.

[66] X. Cai, J. Wang, Z. Bian, H. Zhao, M. Zhang, and Z. Huang. Self-similar propagation and turbulent burning velocity of CH_4/H_2/air expanding flames: Effect of Lewis number. *Combustion and Flame*, 212:1–12, 2020. ISSN 0010-2180. doi: https://doi.org/10.1016/j.combustflame.2019.10.019.

[67] L. Vervisch and D. Veynante. Interlinks between approaches for modeling turbulent flames. *Proceedings of the Combustion Institute*, 28(1):175–183, 2000. ISSN 1540-7489. doi: https://doi.org/10.1016/S0082-0784(00)80209-X.

[68] R.P. Lindstedt and E.M. Váos. Second moment modeling of premixed turbulent flames stabilized in impinging jet geometries. *Symposium (International) on Combustion*, 27(1):957–962, 1998. ISSN 0082-0784. doi: https://doi.org/10.1016/S0082-0784(98)80494-3.

[69] R.P. Lindstedt and E.M. Váos. Modeling of premixed turbulent flames with second moment methods. *Combustion and Flame*, 116(4):461–485, 1999. ISSN 0010-2180. doi: https://doi.org/10.1016/S0010-2180(98)00058-3.

[70] K. N. C. Bray, M. Champion, and P. A. Libby. The interaction between turbulence and chemistry in premixed turbulent flames. In R. Borghi and S. N. B. Murthy, editors, *Turbulent Reactive Flows*, pages 541–563, New York, NY, 1989. Springer US. ISBN 978-1-4613-9631-4.

[71] I. B. Çelik, Z. N. Çehreli, and I. Yavuz. Index of Resolution Quality for Large Eddy Simulations. *Journal of Fluids Engineering*, 127(5):949–958, 09 2005. ISSN 0098-2202. doi: https://doi.org/10.1115/1.1990201.

[72] O. A. Sergeev, A. G. Shashkov, and A. S. Umanskii. Thermophysical properties of quartz glass. *Journal of engineering physics*, 43(6):1375–1383, 1982. doi: https://doi.org/10.1007/BF00824797.

[73] B.S. Hemingway. Quartz: heat capacities from 340 to 1000 k and revised values for the thermodynamic properties. *American Mineralogist*, 72(3-4):273–279, 1987.

[74] A. S. Agazhanov, D. A. Samoshkin, and Y. M. Kozlovskii. Thermophysical properties of inconel 718 alloy. *Journal of Physics: Conference Series XXXV Siberian Thermophysical Seminar*, 1382:012175, 2019. doi: doi:10.1088/1742-6596/1382/1/012175.

[75] C.O. Popiel. Free convection heat transfer from vertical slender cylinders: A review. *Heat Transfer Engineering*, 29(6):521–536, 2008. doi: https://doi.org/10.1080/01457630801891557.

[76] W. K. Metcalfe, S. M. Burke, S. S. Ahmed, and H. J. Curran. A hierarchical and comparative kinetic modeling study of C1 C2 hydrocarbon and oxygenated fuels. *International Journal of Chemical Kinetics*, 45(10):638–675, 2013. doi: https://doi.org/10.1002/kin.20802.

[77] N. Donohoe, A. Heufer, W. K. Metcalfe, H. J. Curran, M. L. Davis, O. Mathieu, D. Plichta, A. Morones, E. L. Petersen, and F. Güthe. Ignition delay times, laminar flame speeds, and mechanism validation for natural gas/hydrogen blends at elevated pressures. *Combustion and Flame*, 161(6):1432–1443, 2014. ISSN 0010-2180. doi: https://doi.org/10.1016/j.combustflame.2013.12.005.

[78] C. Ji, D. Wang, J. Yang, and S. Wang. A comprehensive study of light hydrocarbon mechanisms performance in predicting methane/hydrogen/air laminar burning velocities. *International Journal of Hydrogen Energy*, 42(27):17260–17274, 2017. ISSN 0360-3199. doi: https://doi.org/10.1016/j.ijhydene.2017.05.203.

[79] E. Mastorakos, A.M.K.P. Taylor, and J.H. Whitelaw. Extinction of turbulent counterflow flames with reactants diluted by hot products. *Combustion and Flame*, 102(1):101–114, 1995. ISSN 0010-2180. doi: https://doi.org/10.1016/0010-2180(94)00252-N.

[80] A. M. Garcia, S. Le Bras, and W. Polifke. Effect of hydrogen addition on the consumption speed of lean premixed laminar methane flames exposed to combined strain and heat loss. *Combustion Theory and Modelling*, page 20, 2022. doi: https://doi.org/10.1080/13647830.2023.2182235.

[81] C. K. Law. *Combustion Physics*. Cambridge University Press, 2006.

[82] C. Chi, G. Janiga, K. Zähringer, and D. Thévenin. Dns study of the optimal heat release rate marker in premixed methane flames. *Proceedings of the Combustion Institute*, 37(2):2363–2371, 2019. ISSN 1540-7489. doi: https://doi.org/10.1016/j.proci.2018.07.095.

[83] T. M. Wabel, P. Zhang, X. Zhao, H. Wang, E. Hawkes, and A. M. Steinberg. Assessment of chemical scalars for heat release rate measurement in highly turbulent premixed combustion including experimental factors. *Combustion and Flame*, 194:485–506, 2018. ISSN 0010-2180. doi: https://doi.org/10.1016/j.combustflame.2018.04.016.

[84] D. Suckart and D. Linse. Modelling turbulent premixed flame–wall interactions including flame quenching and near-wall turbulence based on a level-set flamelet approach. *Combustion and Flame*, 190:50–64, 2018. ISSN 0010-2180. doi: https://doi.org/10.1016/j.combustflame.2017.11.005.

[85] W. Polifke, A. Poncet, C.O. Paschereit, and K. Döbbeling. Reconstruction of acoustic transfer matrices by instationary computational fluid dynamics. *Journal of Sound and*

Vibration, 245(3):483–510, 2001. ISSN 0022-460X. doi: https://doi.org/10.1006/jsvi.2001.3594.

[86] A. Huber and W. Polifke. Dynamics of practical premixed flames, part i: Model structure and identification. *International Journal of Spray and Combustion Dynamics*, 1(2):199–228, 2009. doi: https://doi.org/10.1260/175682709788707431.

[87] D. Iurashev, G. Campa, V. V. Anisimov, and E. Cosatto. Two-step approach for pressure oscillations prediction in gas turbine combustion chambers. *International Journal of Spray and Combustion Dynamics*, 9(4):424–437, 2017. doi: https://doi.org/10.1177/1756827717711016.

[88] D. Iurashev, G. Campa, V. V. Anisimov, and E. Cosatto. Three-step approach for prediction of limit cycle pressure oscillations in combustion chambers of gas turbines. *Combustion Theory and Modelling*, 21(6):1148–1175, 2017. doi: https://doi.org/10.1080/13647830.2017.1349343.

[89] W. Polifke, *TFDtools*. private communication, 2021.

[90] W. Polifke. Modeling and analysis of premixed flame dynamics by means of distributed time delays. *Progress in Energy and Combustion Science*, 79:100845, 2020. ISSN 0360-1285. doi: https://doi.org/10.1016/j.pecs.2020.100845.

[91] S. Föller and W. Polifke. Advances in identification techniques for aero-acoustic scattering coefficients from large eddy simulation. Proceedings of the 18th International Congress on Sound and Vibration, 2011.

[92] T. Komarek and W. Polifke. Impact of Swirl Fluctuations on the Flame Response of a Perfectly Premixed Swirl Burner. *Journal of Engineering for Gas Turbines and Power*, 132(6), March 2010. ISSN 0742-4795. doi: https://doi.org/10.1115/1.4000127.